

# Measurements with a High-Granularity Digital Electromagnetic Calorimeter

**ISBN: 978-90-393-6757-5**

**A catalogue record is available from the Utrecht University Library.**

# Measurements with a High-Granularity Digital Electromagnetic Calorimeter

Metingen met een Hoge-Granulariteits Digitale  
Elektromagnetische Calorimeter

(met een samenvatting in het Nederlands)

## Proefschrift

ter verkrijging van de graad van doctor aan de Universiteit Utrecht op gezag  
van de rector magnificus, prof.dr. G.J. van der Zwaan, ingevolge het besluit  
van het college voor promoties in het openbaar te verdedigen op woensdag 24  
mei 2017 des ochtends te 10.30 uur

door

**Chunhui Zhang**

geboren op 12 juni 1984 te Shaanxi, Volksrepubliek China

**Promotor:** Prof.dr. T. Peitzmann

**Copromotoren:** Dr.ir. G.J.L. Nooren

Dr.ir. M. van Leeuwen

This research was accomplished with financial support from China Scholarship Council (CSC) for the first two years and the Netherlands Organisation for Scientific Research (NWO) via the Fundamenteel Onderzoek der Materie (FOM) for the last two years.

# Contents

<b>Contents</b>	<b>i</b>
<b>1 Introduction</b>	<b>1</b>
1.1 Parton Distribution Functions and Gluon Saturation . . . . .	1
1.2 Forward Photon Production in High-energy Physics . . . . .	3
1.3 The ALICE Experiment . . . . .	6
1.4 Introduction on Calorimetry . . . . .	8
1.5 Properties of Calorimeters . . . . .	9
1.6 Typical Existing Electromagnetic Calorimeters . . . . .	11
1.7 The FoCal Detector as A Possible Upgrade . . . . .	14
<b>2 Design</b>	<b>19</b>
2.1 The Prototype . . . . .	19
2.2 MIMOSA Sensor . . . . .	20
2.3 Stack of Prototype . . . . .	22
2.4 Cooling . . . . .	25
2.5 Initial Coordinate System . . . . .	25
2.6 Trigger Scintillators . . . . .	26
2.7 Data Readout . . . . .	27
2.8 Measurement Setup . . . . .	28
2.9 Tuning of Sensors Thresholds . . . . .	29
2.10 Software . . . . .	30
<b>3 Data Quality</b>	<b>33</b>
3.1 Event Displays . . . . .	33
3.2 Raw Distribution of Hits . . . . .	33
3.3 Channel Synchronization and Balance/Asymmetry . . . . .	35
3.4 Data Cleaning . . . . .	35
3.5 Noise . . . . .	37
3.6 Raw Sensor Response . . . . .	39

<b>4</b>	<b>Test Beam Data Analysis</b>	<b>43</b>
4.1	Event Selection . . . . .	43
4.2	Tracking and Alignment . . . . .	45
4.3	Shower Position Determination . . . . .	46
4.4	Inclination of The Beam . . . . .	49
4.5	Measurement of Hit Densities . . . . .	51
4.6	Instrumental Calibration . . . . .	52
4.6.1	Relative sensitivity calibration within each layer . . . . .	53
4.6.2	Response calibration between the layers . . . . .	54
4.6.3	Calibration constants . . . . .	56
4.6.4	Calibration quality . . . . .	56
4.6.5	Correlation between calibration constants and cluster size . . . . .	57
4.6.6	Hit density extrapolation method for dead area . . . . .	57
<b>5</b>	<b>Simulation</b>	<b>61</b>
5.1	Description of General Simulation . . . . .	61
5.2	Noise . . . . .	65
5.3	Charge Diffusion Model . . . . .	66
5.4	Determining The Model Parameters . . . . .	68
5.5	Simulation Results . . . . .	69
5.5.1	Shower position determination . . . . .	70
5.5.2	Effects of charge diffusion . . . . .	70
5.5.3	Limitation of interpolation for dead areas . . . . .	71
5.5.4	Calculation of the average response . . . . .	72
5.5.5	Fitting the longitudinal profiles . . . . .	73
5.5.6	Effects of calibration . . . . .	74
<b>6</b>	<b>Results</b>	<b>77</b>
6.1	Introduction . . . . .	77
6.1.1	Systematic uncertainties . . . . .	78
6.1.2	Lateral hit density profile . . . . .	79
6.1.3	Fitting the lateral hit density profiles . . . . .	83
6.1.4	Longitudinal profile . . . . .	87
6.1.5	Molière radius . . . . .	89
6.1.6	Detector response and linearity . . . . .	90
6.1.7	Energy resolution . . . . .	91
6.1.8	Two-shower separation . . . . .	92
6.2	Comparison with Simulation . . . . .	93
6.2.1	Longitudinal and lateral profile . . . . .	94
6.2.2	Linearity and energy resolution . . . . .	97

---

<b>7</b>	<b>Conclusions and Outlook</b>	<b>101</b>
7.1	Summary . . . . .	101
7.2	Discussion . . . . .	103
7.3	Outlook . . . . .	105
<b>8</b>	<b>Appendix</b>	<b>107</b>
	<b>Bibliography</b>	<b>113</b>
	<b>Nederlandse Samenvatting</b>	<b>117</b>
	<b>Acknowledgments</b>	<b>121</b>
	<b>Curriculum Vitae</b>	<b>123</b>





# Chapter 1

## Introduction

The internal structure of protons and nuclei is described by the parton distribution functions (PDF). For high-energy collisions of particles at the LHC the knowledge of these PDFs in particular at low-momentum fraction  $x$  is crucial. This is a region, however, where they are not very well determined. In addition, theoretical calculation predicts non-linear behaviour leading to an effect called gluon saturation, which is of interest in itself. Also the ALICE experiment, whose main goal is the study of the Quark-Gluon Plasma, suffers from this uncertainty. Within ALICE, it is being discussed to use forward measurements of photons at the LHC to better constrain the small- $x$  parton distributions. A forward calorimeter (FoCal) is being proposed as an upgrade in ALICE for this purpose.

### 1.1 Parton Distribution Functions and Gluon Saturation

Our current picture of hadrons is based on the *parton model*, which assumes that deep inelastic scattering (DIS) of leptons off hadrons can be explained as the elastic scattering off point-like constituents, the *partons*. The charged constituents visible in DIS are called *quarks*, in addition there are neutral partons, the *gluons*. Quarks possess a property called colour charge. There are three types of colour charge. Each quark carries a colour. The interaction between coloured quarks is called strong interaction, and is described in the theory of quantum chromodynamics (QCD). While quarks are confined inside hadrons at low energy, they behave like free particle in high-energy interactions (e.g. in DIS), a property called *asymptotic freedom*. Knowledge of the density of quarks and gluons (partons in general) in a nucleon or a nucleus is crucial to the understanding of particle production in high-energy collisions.

The Parton Distribution Functions (PDFs) of hadrons, which give the parton densities as a function of the fraction  $x$  of the longitudinal momentum carried by the parton, are essential in order to make predictions for the Standard Model and beyond the Standard Model processes at hadron colliders. The PDFs depend on the four-momentum transfer squared  $Q^2$  exchanged in a given process. The corresponding evolution can be described using the DGLAP evolution equations [1] which can be derived in QCD. But QCD can not calculate the parton distributions themselves. They have to be obtained from experiment, and they suffer from large uncertainties at very small  $x$ . Most of the information about PDFs comes from DIS measurements. DIS results are interpreted in the parton model. The differential cross section for the example of electron-proton scattering, which can be written using two structure functions  $F_1$  and  $F_2$  [2]:

$$F_1(x) = \frac{1}{2} \sum_i Q_i^2 f_i(x), \quad (1.1)$$

$$F_2(x) = x \sum_i Q_i^2 f_i(x), \quad (1.2)$$

where the constituents of the proton will have mostly collinear momentum with the proton and each parton of charge  $Q_i$  has a probability  $f_i(x)$  to carry a fraction  $x$  of the original proton momentum. There is a relation  $F_2(x) = 2xF_1(x)$ , which one can use to show that the partons in DIS (the quarks) have spin 1/2. Bjorken scaling advances that there must exist some range of energies for which the functions  $F_1$  and  $F_2$  are independent of  $Q^2 = -q^2$ , at higher or lower values of  $x$ , the  $Q^2$  dependence of  $F_2$  returns. These scaling violations can be explained by the strong interaction (QCD), which leads to parton splitting, and the quantitative description is given by the DGLAP evolution equations.

DGLAP evolution predicts a further rapid growth of the PDFs towards small values of  $x$ , which would ultimately violate unitarity. However, at sufficiently high densities, gluons start to overlap and this leads to the possibility to have gluon fusion (or recombination) in addition to the splitting processes. This leads to different evolution equations, which are no longer linear (in contrast to the DGLAP equations). The new kind of evolution leads to gluon saturation [3–5]. The new high density state of gluon matter produced is often called the Colour Glass Condensate (CGC). The effect of gluon saturation becomes important for small  $Q^2$  and with decreasing  $x$ . The region of gluon saturation starts when  $Q$  is smaller than the saturation scale  $Q_S$ , which depends on the nuclear mass  $A$  and  $x$ ,

$$Q_S^2 \sim A^{1/3} \cdot x^{-0.3}. \quad (1.3)$$

The enhancement factor  $A^{1/3}$  leads to stronger effects of gluon saturation in

heavy ion collisions. Because one also expects medium modifications in the final state in heavy-ion collisions, proton-nucleus collisions are seen as an ideal system to study saturation. In particular, saturation should be observable in a comparison of particle production in pA to that in pp.

In particle production in a high energy collisions, the  $x$ -values of the incoming partons can be approximately described as:

$$x \approx \frac{2p_T}{\sqrt{s}} e^{-y} \quad (1.4)$$

where  $\sqrt{s}$  is the centre of mass energy,  $y$  and  $p_T$  are the rapidity and the transverse momentum of the outgoing parton. The  $x$  becomes small with increasing beam energy, so LHC is the ideal machine to study saturation. Furthermore, small values of  $x$  are accessed in the production of particles at small values of  $p_T$  and large  $y$ . At high energy, rapidity can be approximated by the pseudorapidity:

$$\eta = -\ln \left( \tan \left( \frac{\theta}{2} \right) \right) \quad (1.5)$$

So measurements at large rapidities imply coverage at small polar angles.

## 1.2 Forward Photon Production in High-energy Physics

Direct photons produced from parton interactions can provide strong constraints on the gluon PDFs. At the leading order, the dominant processes are the quark-gluon Compton scattering (see Fig. 1.1 at the bottoms), and quark-antiquark annihilation. At the next-to-leading order, photons may also be produced in bremsstrahlung or fragmentation of one of the outgoing partons. The direct photons can probe the parton distribution more precisely by constraining the kinematics of the underlying partonic interaction.

Now there are other electromagnetic processes that happen in hadron scattering, which are related to the DIS diagrams and yield similar information. The most important of these processes are shown in Fig. 1.1. The LO process of Drell-Yan pair production (middle left) is closely related to the LO diagram for DIS by crossing symmetry. It can give information on the quark distributions, but unfortunately, the cross section is very small, so it is difficult to measure. Also (as LO DIS) it is not sensitive to gluons directly. Similarly the NLO process for Drell-Yan (middle right) is related by crossing symmetry to the NLO diagram of DIS, and it is also sensitive to gluons. This latter process is sometime also called “virtual Compton scattering”, because it is similar to the Compton scattering (below), but with a virtual photon being emitted instead of a real

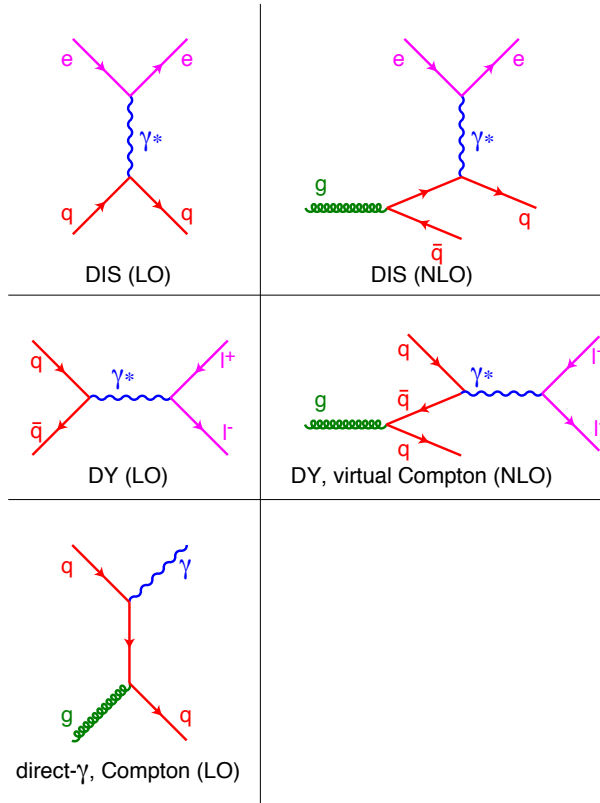


**Figure 1.1:** Examples of Feynman diagrams for electromagnetic processes relevant for probing the parton distribution functions. Upper row: deep-inelastic scattering (DIS) at leading order (LO, left) and next-to-leading order (NLO, right), middle row: Drell-Yan pair production at LO (left) and NLO (right), bottom row left: direct photon production at LO.

photon. Here is where the advantage of direct real photons comes. Photon production is sensitive at LO to the gluon density via the quark-gluon Compton scattering process (lower left), and its cross section is much higher than Drell-Yan. So photon production should be an advantageous way of extracting information on the gluon PDF.

In the leading order case of the quark-gluon Compton or annihilation process, there are 2 partons in the initial state and 1 parton and a direct photon in the final state. While the measurement of inclusive direct photons does already yield important information, the measurement of a direct photon in coincidence with a recoiling jet would constrain the parton kinematics even more. In particular, when one of the incoming partons lies in a region where the PDFs are well-known, the PDF of the other parton can be strongly constrained by a gamma-jet

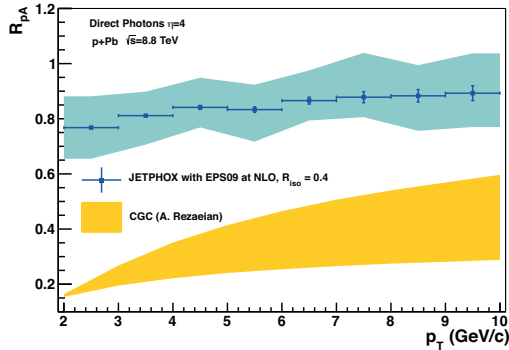


**Figure 1.2:** Nuclear modification factor  $R_{pPb}$  of direct photons from pQCD (shadow with blue points) and from saturation (yellow). Taken from [6].

coincidence measurement.

To probe the gluon distributions in the interesting region of small  $x$  and  $Q^2$ , it will be necessary to perform direct photon measurements at the LHC at low  $p_T$  and at more forward rapidity.

To study the details of gluon saturation experimentally, one would like to measure direct photon production over a wide range of rapidity and transverse momenta, particularly extending the measurements as low in  $p_T$  as possible. In this way, much of the saturation region would become accessible.

The proposed strategy is to compare pp collisions to pA collisions under the same conditions. The saturation leads to a reduction of the gluon density in the nucleus and that in turn to a suppression of photon production in pA compared to pp. One studies it with the nuclear modification factor  $R_{pA}$  of direct photons:

$$R_{pA}(p_T) = \frac{1}{\langle N_{coll} \rangle} \frac{1/p_T \, dN/dp_T(pA)}{1/p_T \, dN/dp_T(pp)} \quad (1.6)$$

where  $\langle N_{coll} \rangle$  is the number of nucleon-nucleon collisions. Fig. 1.2 shows the prediction of the  $R_{pPb}$  from pQCD and from saturation. pQCD with nuclear shadowing shows little suppression (blue points) while a CGC calculations shows a strong effect. This difference is the kind of signal we are after with our photon measurement in the future.

However, the measurement of direct photons is difficult because of the dominant background of decay photons, mainly from neutral pion decays. At forward rapidity, the energy of particles for a given value of  $p_T$  becomes high, so that, the opening angle of decay photons becomes small. Even for a relatively large distance of 7 m of the detector from the interaction point, the minimum separation between two decay photons is small as shown in Fig. 1.3. To discriminate the

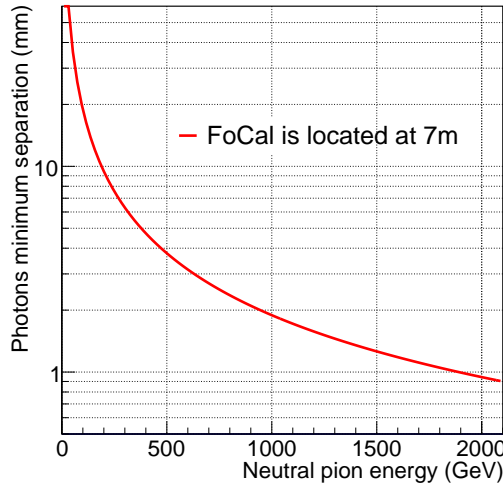


**Figure 1.3:** Minimum separation of the two decay photons as a function of neutral pion energy when FoCal is located at 7 m away from the neutral pion decay point.

direct photons from decay photons, a high-granularity calorimeter is required.

### 1.3 The ALICE Experiment

ALICE (A Large Ion Collider Experiment) is an experiment devoted to the study of the Quark-Gluon Plasma (QGP) which occurs in nuclear collisions at the LHC (Large Hadron Collider). To fully characterise these nuclear collisions, many subdetectors were built and combined into the ALICE detector, as shown in Fig. 1.4.

Below we briefly describe the main subsystems of ALICE [7], more detailed descriptions see their Technical Design Reports (TDRs) [8].

- *Event characterisation*

The impact parameter of the collisions (whether they are central or peripheral) is monitored with the Zero Degree Calorimeters (ZDC) which are located on both sides of ALICE, along the beam line. Charged particles produced at small angles relative to the beam line direction will be measured by the Forward Multiplicity Detector (FMD) which cover a kinematical range of  $1.7 < \eta < 5.1$ . The VZERO (V0) and T0 detectors also measure at small angles and are mainly employed for triggering purposes. V0 is made of two scintillator arrays, and T0 detector consists of two arrays of Cherenkov counters.

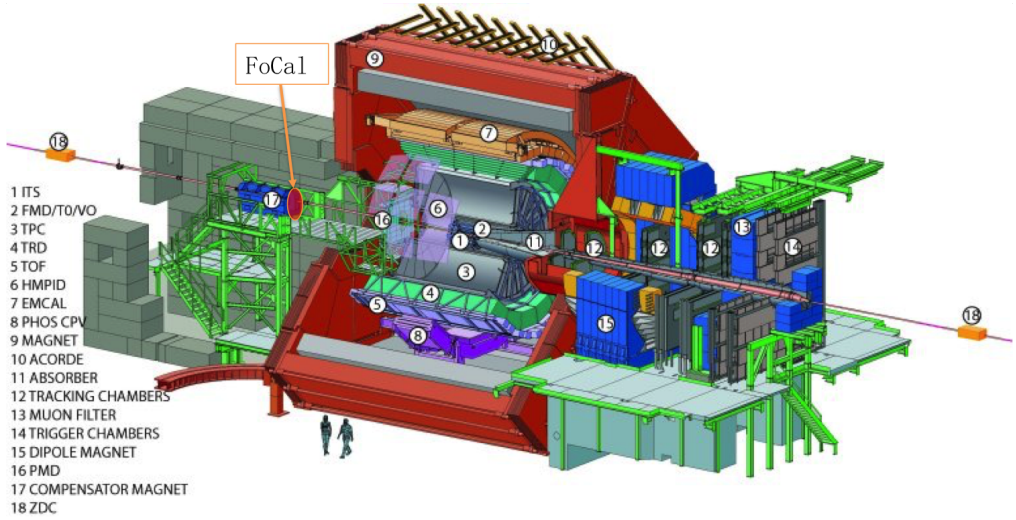


**Figure 1.4:** Layout of the ALICE detector. The proposed FoCal will be placed at 7 m away from the nominal interaction point, outside of the magnet of ALICE.

- *Charged particle tracking*

The charged particles go outwards from the collision point. A series of cylindrical detectors from inside out are used to track the particles, these detectors are Inner Tracking System (ITS), Time Projection Chamber (TPC) and Transition Radiation Detector (TRD). The tracks of charged particles can be reconstructed by the combined measurements from these tracking detectors. The momentum of charged particles can be calculated because of the magnetic field produced by the magnet. The innermost detector ITS consists of six cylindrical layers of silicon detectors, covers  $|\eta| < 0.9$  over the full azimuth. Its high spatial resolution allows to identify weakly decaying particles which do not originate from the collision point.

- *Charged particle identification*

Together with the TPC and the ITS, a number of specialized detector can help to identify charged particles:

TPC and ITS can measure the specific energy loss of a particle.

The TOF detector measures the time of flight of particles from the main vertex.

The HMPID measures Cherenkov radiation from fast charged particles via ring images, whose radius depends on the velocity of particles.

The TRD measures transition radiation, which is emitted by highly relativistic particles at boundaries between different media.

All of these provide some information on the velocity of a particle, which together with the momentum allows to identify them.

- *Forward muon measurement*

At small angles, the muon spectrometer is installed, which measures the momenta of muons in a magnetic spectrometer and identifies them with the use of a thick absorber, which filters out most other charged particles.

- *Photon measurements*

Other special detectors are required to measure high-energy photons. Two electromagnetic calorimeters, PHOS and EMCal, measure photons using different technologies – we will discuss them in some detail below. In addition, the PMD can measure the multiplicity of photons at small angles.

## 1.4 Introduction on Calorimetry

Calorimetry in particle physics is a powerful measurement technique, more introduction on calorimetry see publications such as [9]. A calorimeter is a detector which measures the particle energy from  $\sim$ MeV to TeV. In the measurement process in a calorimeter, an incident particle will produce secondary particles and lose its energy, such that the initial energy of the particle can be obtained by measuring the energy deposited in the calorimeter.

Calorimeters can be classified into electromagnetic and hadronic according to the type of particle one aims to detect. Electromagnetic calorimeters are specifically designed to measure the energy of particles that interact primarily via the electromagnetic interaction, while hadronic calorimeters are designed to measure particles that interact via the strong nuclear force.

They can further be classified into homogeneous calorimeters and sampling calorimeters according to the structure and the materials used. The main advantage of homogeneous calorimeters is their optimal energy resolution since the whole energy of a particle is deposited in the active medium. On the other hand, the materials that can be used as absorbing materials and detectors are very expensive and have a large interaction length. The homogeneous calorimeters are only employed as electromagnetic calorimeters.

A typical sampling calorimeter consists of alternating layers of passive absorbers and active volumes, in which part of the energy is sampled in active volumes. One advantage of this is that each material can be well-suited to its task by choosing the absorbers and active volumes. For example, a very dense



material can be used to produce a shower that evolves quickly in a limited space, even if the material is unsuitable for measuring the energy deposited by the shower. A disadvantage is that some of the energy is deposited in absorber and is not measured, thus the total shower energy must be estimated.

Both the proposed FoCal and the prototype studied here are electromagnetic sampling calorimeters. Below we will thus focus on properties of electromagnetic sampling calorimeters.

An incoming high-energy electron, positron, or photon interacts with the material and creates secondary particles (again photons, electrons and positrons), which are of high enough energy to again undergo similar interactions. They will produce particles of lower and lower energy until all the energy is deposited in the material. This process is called electromagnetic cascade, or an electromagnetic shower. For electrons or positrons, at high energy, the dominant process is bremsstrahlung, while at low energy, it is ionization and excitation of atoms. For photons, at high energy, the dominant process is pair production, and at intermediate energy it is the Compton effect. Below the critical energy  $E_c$ , ionization losses predominate over radiation, and above  $E_c$  radiation is dominant.

When no more new particles are produced in the cascade, the multiplication is stopped. At this point the number of shower particles reaches its maximum, the so-called shower maximum. The shower development in the longitudinal direction can be described in terms of the radiation length  $X_0$ . In the lateral direction, the shower widens with increasing depth mainly because of two types of processes [9]: “(i) Electrons and positrons move away from the shower axis because of multiple scattering. (ii) Photons and electrons produced in isotropic processes (Compton scattering, photoelectric effect) move away from the shower axis”. The first process is dominant before and the second after shower maximum. The Molière radius  $R_M$  is used to describe the lateral shower size, which depends on the detector material. These material parameters are further discussed below.

## 1.5 Properties of Calorimeters

Material properties of a detector are the radiation length  $X_0$ , the critical energy  $E_c$  and the Molière radius  $R_M$ . Another important property of a calorimeter is its energy resolution, which depends in part on the material parameters, but also on the detector structure and the readout components.

- The radiation length  $X_0$  for a material describes the thickness in unit of  $\text{g}/\text{cm}^2$ , where a high energy electron or positron has lost as much energy to be left with a fraction  $1/e$ .  $X_0$  has been calculated and tabulated by

Y.S. Tsai [10]

$$X_0 = \frac{716 \cdot A}{Z(Z+1) \ln(287/\sqrt{Z})} \text{ g cm}^{-2} \quad (1.7)$$

where  $Z$  is the atomic number and  $A$  is the mass number of the nucleus. The value of  $X_0$  depends on the characteristics of the material, for a mixture or compound, it is calculated using the following equation

$$\frac{1}{X_0} = \left( \sum_i \frac{V_i}{X_0^i} \right) \quad (1.8)$$

where  $V_i$  and  $X_0^i$  are the fraction of volume and the radiation length of a single type of nucleus.

- The critical energy is defined as the energy for which the bremsstrahlung and ionization rates are equal, estimated as [11]

$$E_c = \frac{610(710)\text{MeV}}{Z + 1.24(0.92)} \quad (1.9)$$

for materials in the solid or liquid (gas) state.

- The longitudinal shower shape is described well as Gamma distribution [12]

$$\frac{dE}{dt} = E_0 \beta \frac{(\beta t)^{\alpha-1} e^{-\beta t}}{\Gamma(\alpha)} \quad (1.10)$$

where  $E_0$  is the primary particle energy,  $\alpha$  and  $\beta$  are shape parameters, and the scale variables  $t = x/X_0$ . The depth of the shower maximum  $t_{max}$  is usually parameterised as

$$t_{max} = (\alpha - 1)/\beta \approx \ln \frac{E_0}{E_c} + C_j, \quad j = e, \gamma \quad (1.11)$$

where  $C_j = -0.5$  for electron induced cascades and  $C_\gamma = +0.5$  for photo-induced cascade.

The calorimeter thickness containing 95% of the shower energy is approximately given by

$$t_{95\%} = t_{max} + 0.08Z + 9.6 \quad (1.12)$$

- The Molière radius is used to describe the lateral size of an electromagnetic shower. It is defined as the radius of a cylinder in which 90% of the total energy is deposited. About 95% of the energy is contained within  $2R_M$ .

$R_M$  is related to the radiation length and critical energy [13, 14] via:

$$R_M = \frac{21.2\text{MeV}}{E_c} X_0 \quad (1.13)$$

- The energy resolution  $\frac{\sigma_E}{E}$  reflects the accuracy of the energy measurement, it is usually parameterised with  $a, b, c$  as

$$\frac{\sigma_E}{E} = \frac{a}{\sqrt{E/\text{GeV}}} \oplus \frac{b}{E/\text{GeV}} \oplus c \quad (1.14)$$

The three terms respectively are ‘stochastic term’, ‘noise term’ and ‘constant term’. The ‘stochastic term’ represents the intrinsic shower fluctuations, the energy resolution improves with increasing primary particle energy as  $1/\sqrt{E}$ . The contribution from noise decreases with increasing energy, such that the ‘noise term’ only has an influence for low energy. The energy independent term – ‘constant term’ – mainly comes from instrumental effects. So one expects a better energy resolution for high energy.

## 1.6 Typical Existing Electromagnetic Calorimeters

PHOS (PHOton Spectrometer) is a lead-tungstate crystal ( $\text{PbWO}_4$ ) electromagnetic calorimeter to measure photons emerging directly from the collision. It is installed at the bottom of ALICE, and covers  $|\eta| \leq 0.12$  in pseudorapidity, and  $100^\circ$  in azimuthal angle. PHOS contains 17,280 detection channels, each channel is  $2.2 \times 2.2 \times 18 \text{ cm}^3$  of  $\text{PbWO}_4$ , coupled to large-area avalanche photodiodes (APDs) with low-noise preamplifiers. The crystals of  $\text{PbWO}_4$  have values of  $R_M = 20 \text{ mm}$  and  $X_0 = 8.9 \text{ mm}$ , for more information about PHOS see its “Technical Design Report” [15].

The ALICE Electromagnetic Calorimeter (EMCal) is a lead-scintillator sampling calorimeter with the aim of enhancing the capabilities for the measurement of jet quenching towards higher momenta up to  $100 \text{ GeV}/c$ . It is located in the ALICE central detector. The EMCAL occupies part of a cylindrical volume and consists of 12,288 towers. Each individual module has  $2 \times 2$  towers as shown in Fig. 1.5, and consists of 76 alternating layers of  $1.44 \text{ mm}$  Pb and 77 layers of  $1.76 \text{ mm}$  polystyrene based scintillator. So EMCAL covers  $20.1 X_0$  and has  $R_M = 32 \text{ mm}$ . Its “Technical Design Report” gives a comprehensive understanding [16].

The Liquid Argon sampling calorimeter technique in ATLAS was used in electromagnetic and hadronic calorimetry with a  $4\pi$  coverage for high  $p_T$  particles. Its forward calorimeter – FCAL is located near the incident beams, and



*Figure 1.5: The basic module of EMCAL at ALICE. Taken from [16] p.11.*

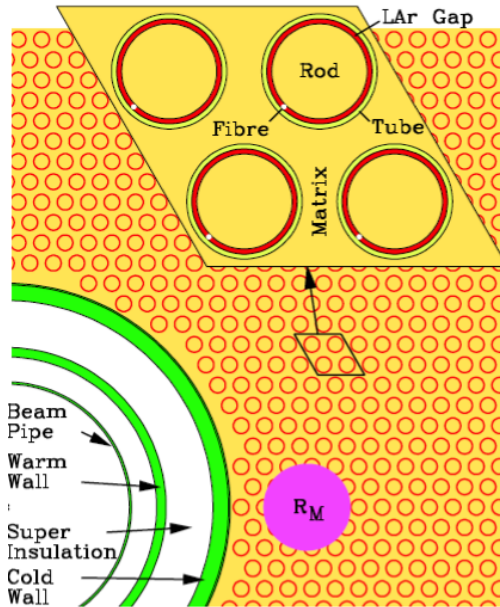


*Figure 1.6: Sketch of matrix and rods at ATLAS. Taken from [17] p.12.*

takes up  $3.0 < \eta < 4.9$ . The FCAL consists of three sections. The first section is made out of copper, while the other two are of tungsten. In each of them the calorimeter consists of a metal matrix with regularly spaced longitudinal channels filled with concentric rods and tubes (see Fig. 1.6). The first section of the FCAL1 covers  $3.0 < \eta < 4.9$  and its granularity is  $2.0 \text{ cm}^2$ . The granularities of the FCAL2 and FCAL3 are  $3.5 \text{ cm}^2$  and  $5.6 \text{ cm}^2$  respectively.

The ECAL at CMS consists of lead tungstate ( $\text{PbWO}_4$ ) which is the same

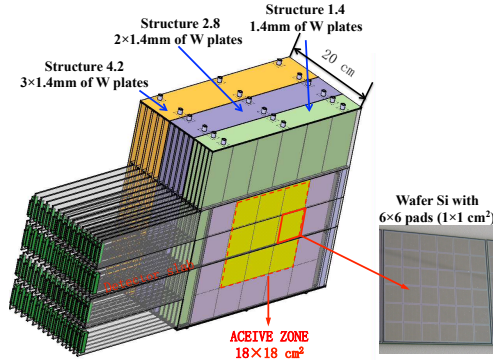


**Figure 1.7:** Schematic view of the Si-W ECAL prototype. Taken from [20] p.242.

material as in PHOS. The detector has a granularity at the front face of  $22 \times 22$   $\text{mm}^2$  (see [18]).

The LHCb electromagnetic calorimeter (ECAL) uses the “shashlik” technology. It is built from individual modules that are made from lead absorber plates interspaced with scintillator tile as active material. There are three types of module that build up the inner, middle and outer section of ECAL. Each module is constructed from alternating layers of 2 mm thick lead, 120  $\mu\text{m}$  thick white reflecting paper and 4 mm thick scintillating tiles (see [19]).

A prototype Si-W ECAL was built by CALICE for an ILC detector, this prototype consists of three stacks. Signals are readout from the silicon wafers with  $1 \times 1$   $\text{cm}^2$  pads. The tungsten thickness is 1.4 mm ( $0.4 X_0$ ) per layer in the first stack, 2.8 mm ( $0.8 X_0$ ) per layer in the second stack and 4.2 mm ( $1.2 X_0$ ) per layer in the rear stack. There is an interlayer gap of 2.2 mm thick in order to accommodate the Si pads and PCB, thus the expected Molière radius of the detector is  $2R_M$  of solid tungsten.

**Table 1.1:** *Properties of existing calorimeters and FoCal.*

	Materials	Granularity (mm <sup>2</sup> )	Molière Radius (mm)
ALICE (PHOS)	PbWO <sub>4</sub>	22 × 22	20
ALICE (EMCal)	Pb+Sc	60 × 60	32
ATLAS (FCal)	Pb+LAr	20 × 20	19
LHCb (ECal)	Pb+Sc	40 × 40	35
CMS (ECal)	PbWO <sub>4</sub>	22 × 22	22
CALICE (Si ECal)	W+Si	10 × 10	~20
Future FoCal	W+Si	1 × 1	<15
FoCal prototype	W+Si	0.03 × 0.03	~10.5

Comparing with the other existing calorimeters, the proposed FoCal has a higher granularity and smaller Molière radius. These features make it suitable to measure the high rapidity forward direct photons in the harsh LHC environment. The comparison is given in Table. 1.1<sup>1</sup>

## 1.7 The FoCal Detector as A Possible Upgrade

To study forward physics, the FoCal proposed as a possible upgrade to the ALICE experiment covering  $3.5 < \eta < 5.3$ , will be installed outside of the magnet at a distance of 7 m. The requirements for two-shower separation are high. As an example, for a neutral pion of  $p_T = 10$  GeV at a rapidity of 4.5 and an energy asymmetry of the decay of  $\alpha = 0.5$ , the separation of the decay photons even at a distance of 7 m is only about 2 mm. Thus a high-granularity detector with sub-millimeter scale is needed to improve the pion rejection efficiency. Such a granularity is not available with conventional technologies. We have chosen pixel sensors (MAPS) with 30  $\mu\text{m}$  pixels – while these certainly fulfil the requirements, they will provide much more extreme granularity, which gives much more information, and is suitable for a prototype to perform detector R&D.

FoCal is composed of an electromagnetic calorimeter and a hadronic calorimeter, called FoCal-E and FoCal-H. The electromagnetic calorimeter will feature high-granularity segments to discriminate direct photons from background, mainly from neutral pion decay. Tungsten has been chosen as absorber, its radiation length is  $X_0 = 3.5$  mm.

FoCal-E is a hybrid sampling calorimeter using Si-W layers in low-granularity layers (LGL) and high granularity layers (HGL). The HGLs are most powerful

<sup>1</sup>CMS and ALICE quote different numbers for the Molière radius of PbWO<sub>4</sub>, but it is not clear from the documentation what that difference is due to.

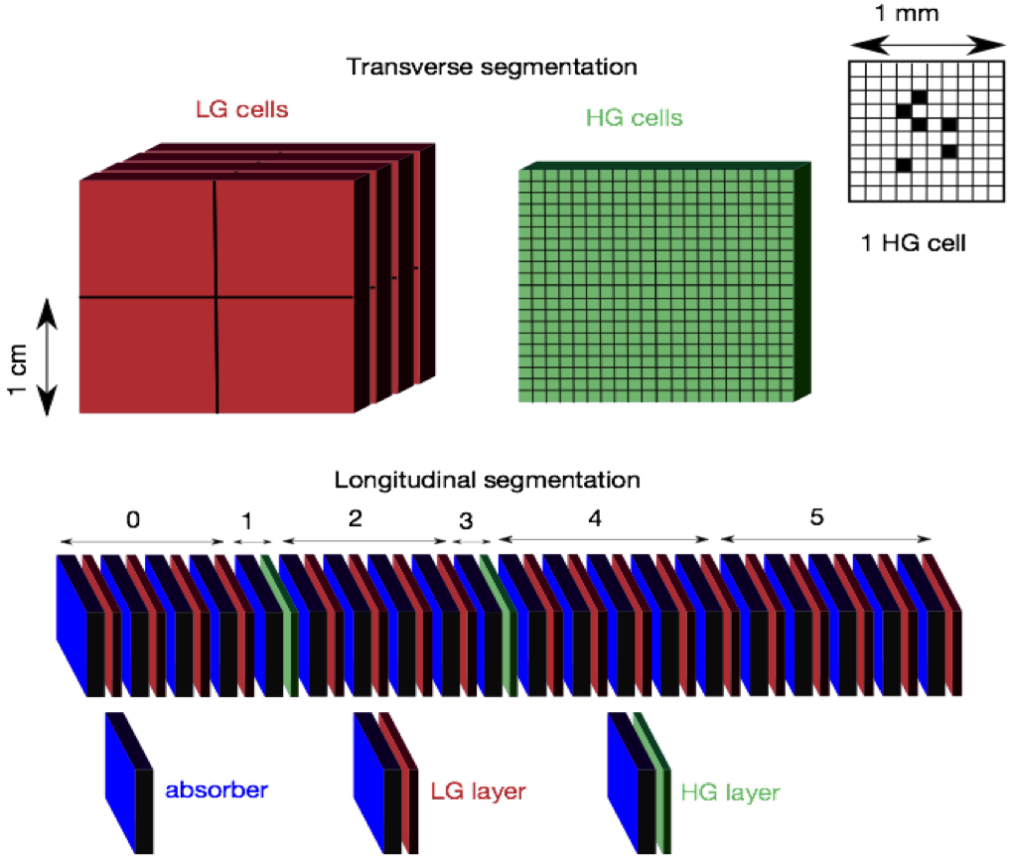


**Figure 1.8:** The concept design for the FoCal detector. Low granularity layers (red) and high granularity layers (green) are inserted between absorbers (blue). The granularities are 1 cm and 0.1 mm. The readout unit of HGLs is independent, and a readout unit contains 4 to 5 LGLs.

for separating close-by photons and provide detailed shower shape analysis capability due to their smaller cells compared to LGLs, while the LGLs provide better energy measurement because of their larger sampling fraction compared to HGLs. A schematic view of the longitudinal structure of FoCal-E is shown in Fig. 1.8. The radiation thickness for each layer and the Molière radius of FoCal-E depend on the thickness of the absorber and the readout, the designed value of  $R_M < 15$  mm.

The MAPS readout is intrinsically slow ( $1/640 \mu\text{s}$  for the prototype, significantly better for the final sensors to be used, but still slow) and cannot provide a trigger signal, which will likely be desirable in p+p collisions, where the interaction rate will be high. In addition, while their envisaged integration time, in the range of 5 – 10  $\mu\text{s}$ , should be short enough to properly separate different

events in Pb+Pb collisions with maximum interaction rate of 50 kHz, pile-up will occur in p+p collisions where interaction rates of 200 kHz or higher are envisaged. These effects will be disentangled by matching clusters in the HGLs and LGLs in position and time.

The LGL will use conventional silicon pad sensors. It is foreseen to sum the analog signals of pads at the same transverse location from different layers within a segment. The sum signals would be routed out of the detector and digitized. The LGL readout will also provide trigger capability.

To facilitate the design of the upgrade and to perform generic R&D necessary for such a novel calorimeter, a compact high-granularity electromagnetic calorimeter prototype has been built. The measurements with this prototype and their analysis is the subject of this thesis. The following general questions are our concerns.

- Does a digital calorimeter work in principle? More specifically:
  - In how far does a digital calorimeter work in a similar way as an analog one, and what are the differences?
  - Is the number of fired pixels a linear function of the primary particle energy?
  - How strong are saturation effects?
- How close do we get to the ideally expected performance?
- What are the new observables of our calorimeter? Which additional information can we access?
- What is the shape of electromagnetic showers at this high level of granularity?
- How well is the behaviour of the calorimeter described by GEANT, and do we see deviations?

To begin with, some properties of detector can be calculated or estimated according to the knowledge of calorimetry. For the FoCal prototype (see the next chapter), the radiation length is calculated as:

$$\begin{aligned}
 \frac{1}{X_0} &= \frac{V_W}{X_W} + \frac{V_{Si}}{X_{Si}} + \frac{V_{PCB}}{X_{PCB}} + \frac{V_{Glue}}{X_{Glue}} + \frac{V_{Air}}{X_{Air}} \\
 &= \frac{0.846}{3.5\text{mm}} + \frac{0.031}{93.6\text{mm}} + \frac{0.041}{167.6\text{mm}} + \frac{0.038}{400\text{mm}} + \frac{0.044}{303900\text{mm}} \\
 &= \frac{1}{4.0\text{mm}}
 \end{aligned} \tag{1.15}$$



**Table 1.2:** *Estimated shower maximum position for SPS beam energies.*

Energy	30 GeV	50 GeV	100 GeV	244 GeV
$t_{max}$	7.7	8.2	9.0	9.8

The critical energy of FoCal is assumed to be the same critical energy as of tungsten (8.1074 MeV). For these assumptions the calculated shower maximum depths for SPS beam energies are listed in Table 1.2. According to Eq. 1.11 and Eq. 1.12, longitudinally containing 95% of the energy up to 250 GeV beam energy needs  $26 X_0$ . According to Eq. 1.13, the Molière radius is 10.5 mm. The very small sampling fraction of the prototype will likely lead to a not so good energy resolution at low energy. It will be interesting to see how good the resolution is at high energy. We will exploit the most important feature of this prototype – its high granularity – by studying finest details of the shower shape with the lateral profiles.

Our studies will be performed on data from beam test measurements, but we will also compare to Monte Carlo simulations.



# Chapter 2

## Design

This chapter will present the design of the high-granularity calorimeter prototype and the test beam setups at DESY and CERN.

### 2.1 The Prototype

The prototype is a Si/W sampling calorimeter using CMOS sensors of the MIMOSA – A type of Monolithic Active Pixel Sensor (MAPS) with a pixel pitch of  $30\ \mu\text{m}$  and binary readout with a total of  $\sim 39$  million pixels. A calorimeter based on MAPS was proposed earlier in the context of the CALICE project for ILC [4], but this is the first implementation of a full MAPS calorimeter prototype. Because high  $Z$  materials lead to a small Molière radius and thus to a small shower size, tungsten was chosen as the absorber. To measure the spatial distribution of showers in detail, high-granularity silicon sensors were chosen as the samplers. The thin sensors were mounted on their own individual thin printed circuit boards (PCB) to minimize the thickness of low  $Z$  materials, i.e. sensors and PCBs. In the current design,  $3.3\ \text{mm}$  tungsten absorber in  $3.9\ \text{mm}$  of the thickness per layer leads to an effective thickness of  $0.97 X_0$  for a single layer. The first sensor layer should preferably measure the particles before the start of showers. Ideally, one would omit the absorber material there. However, as a metal layer is needed to provide both support of the PCB and thermal conductivity, it was chosen to replace the tungsten by aluminum for the front half of the absorber (see Fig. 2.1). The total thickness is  $116\ \text{mm}$  which is the equivalent of  $28 X_0$ . According to Eq. 1.12, up to  $500\ \text{GeV}$ , 95% of the shower energy is contained in the prototype. The calculated Molière radius is  $10.5\ \text{mm}$ , so it is no problem that the prototype is relatively small.

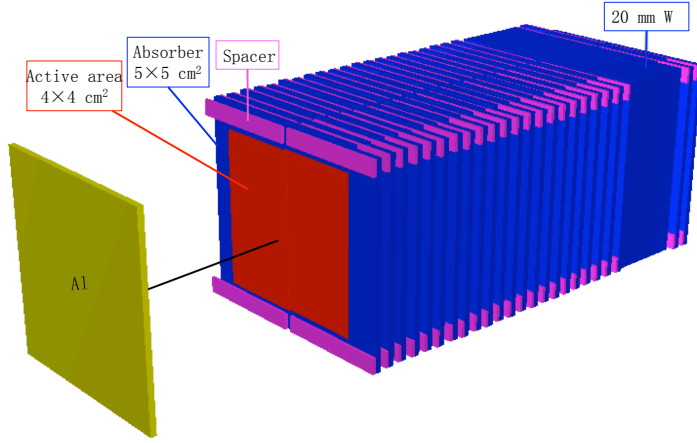


**Figure 2.1:** Schematic view of the FoCal prototype. Aluminum absorber in the first layer is drawn at a distance to uncover the active area, the thick absorber is optional and was not used for low energy measurements.

**Table 2.1:** Three types of sensors employed in prototype.

Sensor type	I	II	III
Thickness of the epitaxial layer ( $\mu\text{m}$ )	14	15	20
Resistivity ( $\Omega/\text{cm}$ )	10	400	400

## 2.2 MIMOSA Sensor

As sensor has been chosen PHASE2/MIMOSA23 from IPHC [31]. This MAPS-type sensor has  $640 \times 640$  pixels covering an active area of  $19.2 \times 19.2 \text{ mm}^2$  in a total sensor size of  $19.52 \text{ mm} \times 20.93 \text{ mm}$ . A schematic view of the MIMOSA sensor is shown in Fig. 2.2 left.

An engineering run at AMS<sup>1</sup> provided 5 wafers with a high resistivity ( $400 \Omega/\text{cm}$ ) epitaxial layer of 15 and  $20 \mu\text{m}$  thickness and 1 standard wafer ( $10 \Omega/\text{cm}$ ,  $14 \mu\text{m}$ ). The former ones were thinned down to  $120 \mu\text{m}$ , the latter to  $180 \mu\text{m}$ . Because of a relatively low yield the detector had to be built with different types of sensors. In our prototype, 19 sensors with  $10 \Omega$  and  $14 \mu\text{m}$  thickness, 46 sensors with  $400 \Omega$  and  $15 \mu\text{m}$  thickness, and 31 sensors with  $400 \Omega$  and  $20 \mu\text{m}$ , are mounted, as indicated in table 8.1. We shortly call the three types of sensors type I, II and III. The different sensors could in principle have different sensitivities which will affect the detector performance.

<sup>1</sup>AMS-C35B4 OPTO by Austria Microsystems.

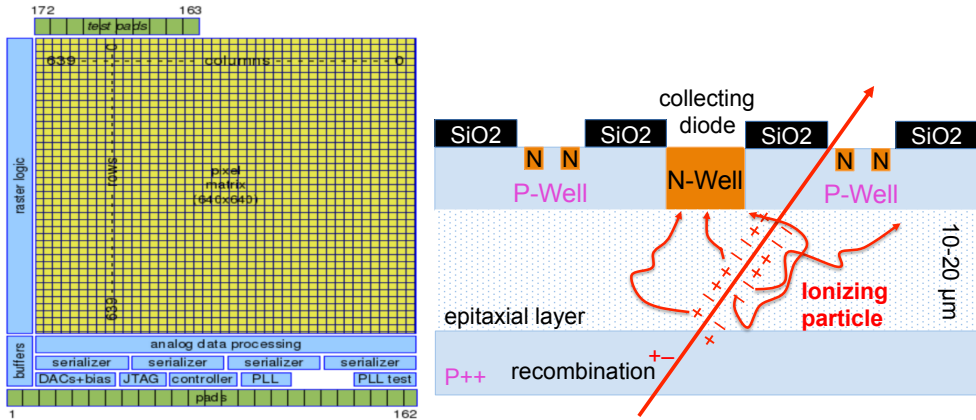


**Figure 2.2:** Left: concept layout of sensor with all the main blocks and the chip architecture [23]. A sensor = 4 serializers, 1 serializer = 160 columns, 1 column = 640 pixels. Right: principle of charge collection when a charged particle crossing a MAP sensor.

Compared to a conventional sensor, the active pixel sensor dissipates much more heat, typically  $0.1 \text{ W}\cdot\text{cm}^{-2}$ . It was realised that the heat can be transported from the sensor chips to the outside by using the rather good heat conductivity of W, namely  $170 \text{ W/m/K}$  (Al:  $237 \text{ W/m/K}$ ). Thus the W-absorbers can also serve as heat conductors connected to cooling elements at their edges. The absence of a separate layer of cooling elements leads to a very compact calorimeter, so helps to achieve the small Molière radius.

The active area of a layer is  $40 \times 40 \text{ mm}^2$ , composed of four sensors, while the absorber measures  $50 \times 50 \text{ mm}^2$ . Taking into account the Molière radius the tower is wide enough to fully contain showers and to study the lateral shower development. The first active layer (*layer 0*) has only  $0.03 X_0$  in front, to act as a charged particle detector.

Fig. 2.2 left shows the layout of the PHASE-2 sensor with the main blocks. All pixels are read out continuously from the 4 ‘serializers’ (‘channel’) which are driven at 160 MHz. The 1 MHz rolling shutter implies an integration time of  $640 \mu\text{s}$ . The resulting low event rate without pile-up makes this unusable for modern particle physics experiments, but is not a problem in the case of our test measurements. Besides the pixel matrix, the MIMOSA23 contains discriminators, and control and output circuitry. Because of this, the a sensor contains some insensitive areas, so we have chosen to let them overlap in one transverse direction to minimise the insensitive areas in the detector. For ease of construction there remains a dead zone of  $0.1 \text{ mm}$  between each pair of chips in the other direction. Fig. 2.2 right shows how a typical MAPS works. At the

bottom is the highly p-doped substrate, over which a p-type epitaxial layer is grown. A charge collecting n-well/p-epi diode and p-well are implanted. The top layer is made of a pixel microcircuit.

When a charged particle penetrates through the sensor active volume – the epitaxial layer – a series of electron-hole pairs is generated along the particle trajectory. Due to only a small depletion near the charge collecting diode, the region is field-free, and the generated electrons will undergo thermal diffusion. Some of them will reach the collecting diode and be collected, and a voltage is generated in the pixel microcircuits. The potential barrier at the border region of p-well and p++ substrate acts as a reflecting surface. The electrons generated in the substrate region hardly can diffuse to the epitaxial layer.

### 2.3 Stack of Prototype

Fig. 2.3 left shows the main part of this prototype. The detector stack is located in the center between the left and right PCBs for readout. This stack consists of 24 layers and an additional 20 mm thick tungsten block inserted between layers 21 and 22. Layer numbers increase from bottom to top, which is also the direction in which the beam travels. Each layer is made of tungsten as absorbers, silicon sensors as samplers, PCBs and glue. The right panel shows a single layer which consists of two half layers. We call this basic unit – half layer – a module.

The structure of a module is shown in Fig. 2.4 on the left, and a corresponding photo is shown in the right panel. Each half layer consists of the following components, whose dimensions are also given below:

- Absorber:  $50 \times 50 \times 1.5 \text{ mm}^3$  of tungsten

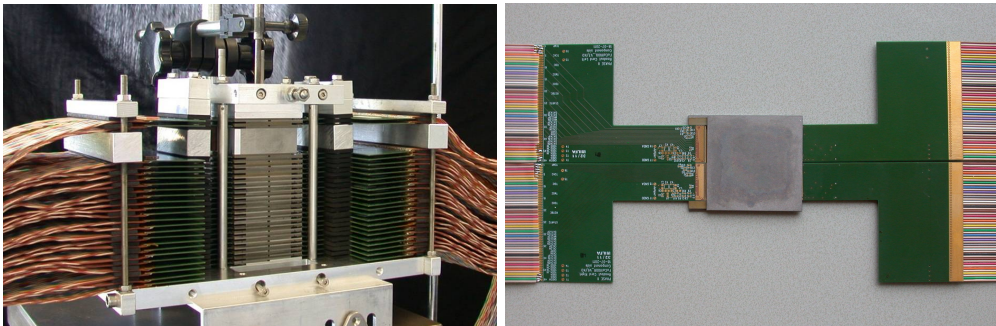


**Figure 2.3:** Left: structure of the FoCal prototype. The stack of W and Si layers is visible in the middle, and the PCBs for readout extend to the left and right. Right: a single layer.

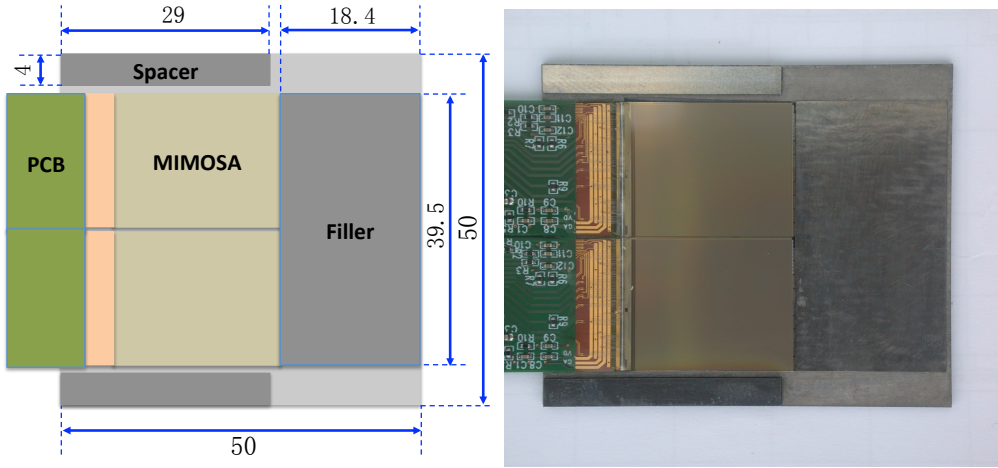


**Figure 2.4:** Left: structure of a basic module. Right: photo of a module. Numbers are given in mm.

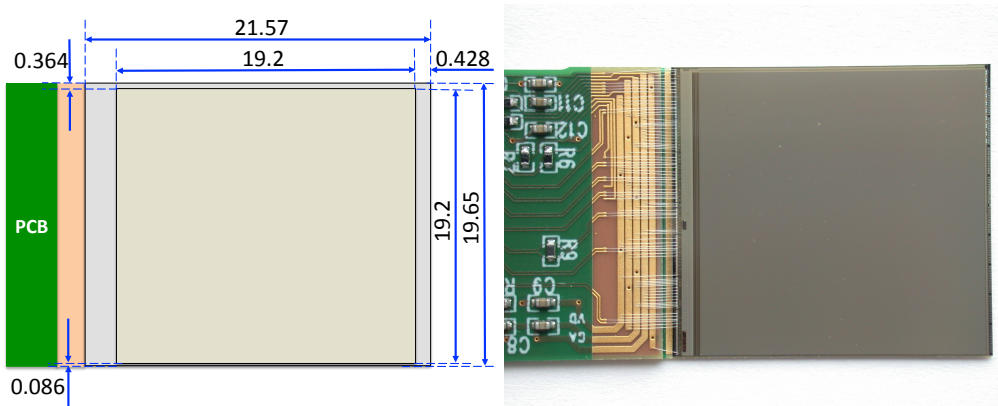


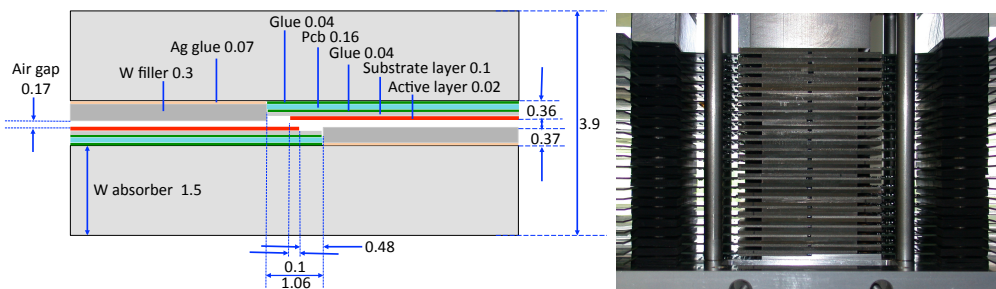
**Figure 2.5:** Left: drawing of a single sensor mounted on a PCB. Right: photo of a single sensor. Numbers are given in mm.

- Filler:  $40 \times 18.5 \times 0.03 \text{ mm}^3$  of tungsten
- PCB: 0.16 mm thick of FR4
- MIMOSA sensor:  $19.52 \times 20.93 \times 0.12 \text{ mm}^3$  of silicon
- Spacer:  $29 \times 4 \times 0.8 \text{ mm}^3$  of steel

Two spacers are glued at the edge of an absorber introducing a glue thickness of  $\sim 0.1$  mm to guarantee a 0.9 mm constant separation between absorbers to prevent the damage of the sensors. Between two spacers, there are two sensors

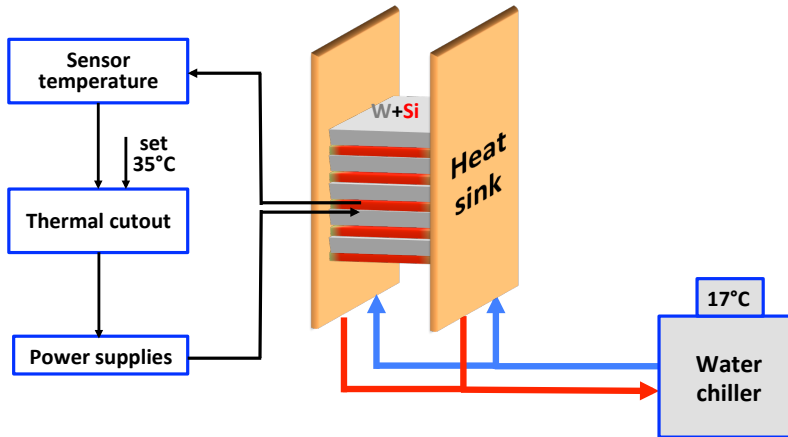
– each of the sensors is mounted on its own PCB as illustrated in Fig. 2.4, so that all the fragile sensors are constrained and protected by the absorbers and spacers. Fig. 2.5 shows a single sensor which is mounted on a PCB. For constructional reasons, the designed PCB is about 0.04 mm larger than the real sensor at the edges. A filler is placed next to the two sensors. Another half layer is turned over and complementally placed to constitute a full single layer with 3.3 mm tungsten, 0.36 mm sampler and 0.17 mm air gap. This geometry results in an effective thickness of one layer of  $0.97 X_0$  and a very small  $R_M$ , calculated to be  $R_M \approx 10.5$  mm. Layer by layer, in total 24 layers and a 20 mm tungsten block were put in a ‘tower’ and pressed tightly in the vertical direction. To align sensors in the horizontal direction, there are two hollow copper parts to restrict the movement. Another function of the copper is cooling the sensors by removing the heat generated in the sensors via the absorbers.

Fig. 2.6 shows a detailed side view of the transition region between the sensors of two half layers. We have tried to make the detector as homogeneous as possible, but there are limitations to this, which are also seen in the analysis. When sensors are placed next to each other within the same plane, there are unavoidable gaps in the sensitive area. To reduce these sensitivity losses at least in one direction, partial overlaps between the sensors are implemented, which can be seen in Fig. 2.6. Also the filler material shows a gap, which leads to a variation of the total material thickness. The figure also indicates the distance in the design positions of the different elements. These positions are important for the final data analysis, but of course, there are unknown variations due to mechanical tolerances.



**Figure 2.6:** Left: drawing of single layer in side view. Right: side view of the real stack.





*Figure 2.7: The cooling and temperature protection system.*

## 2.4 Cooling

An active pixel sensor like the MIMOSA that we use will produce significant heat ( $0.1 \text{ W/cm}^2$ ), while an increased temperature will produce more noise. The cooling system is needed to guarantee stable working conditions of the sensors. We use water cooling to keep the sensor temperature at  $\sim 27^\circ\text{C}$ . Fig. 2.7 shows the water circuit. The heat dissipated from the sensors can be transported to the absorbers due to the good thermal conductivity, then is removed by water from two edges of the absorber. The water chiller keeps the water running and the water temperature at  $17^\circ\text{C}$ . The power supply will be shut down when the temperature of the absorber rises above  $35^\circ\text{C}$  as measured by the thermal sensors.

## 2.5 Initial Coordinate System

The designed FoCal prototype contains gaps in the  $x$ -direction and overlaps in the  $y$ -direction. Some additional displacements of the sensors compared to the design is generated in the assembly process. The coordinate system for the data analysis has the origin in the middle of the first layer. The  $z$  axis points horizontally along the beam direction, while the  $x$  and  $y$  axis are parallel to the detector planes (with  $x$  in the horizontal direction see Fig. 2.8). The differences between ideal and real positions include the gaps and overlaps and the misalignment originating from the assembly. All these will be corrected by the alignment procedure which is described in Sec. 4.2.

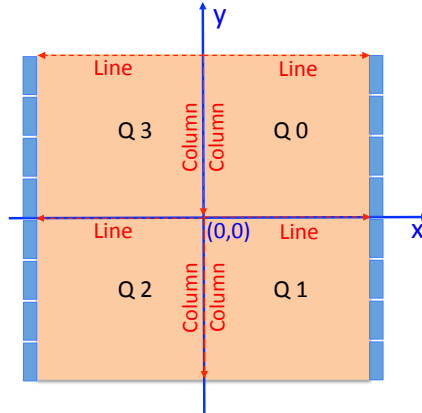


*Figure 2.8:* The initial coordinate system, the line and column number from 0 to 639 in each quadrant is displayed in red, while the coordinate is displayed in blue, the origin of the coordinate is the center of the 4 sensors.

## 2.6 Trigger Scintillators

Five scintillators are mounted in the detector setup for selecting the interesting events. The 5 scintillators are named according to their positions and function. Their sizes are listed below:

- **Presence:**  $110 \times 110 \times 10 \text{ mm}^3$
- **Horizontal:**  $40 \times 10 \times 5 \text{ mm}^3$
- **Vertical:**  $10 \times 20 \times 5 \text{ mm}^3$
- **Front:**  $40 \times 40 \times 10 \text{ mm}^3$
- **Back:**  $40 \times 40 \times 10 \text{ mm}^3$

The installation positions are shown in Fig. 2.9. Signals from the P scintillator, which was placed in front of the prototype, act as a general trigger for an incoming beam particle. Both the F and B scintillators cover  $40 \times 40 \text{ mm}^2$ , which is the same with the sensitive area. The combination of H and V constitutes a central trigger (H&V), which covers  $10 \times 10 \text{ mm}^2$ . The data analysed here use either the coincidence of P&F or only F for a particle close to the active volume, then a coincidence with the central trigger for a particle in the central part of the detector. The B scintillator was meant to detector muons or possible leakage mainly for hadronic showers. It was not used in this analysis.

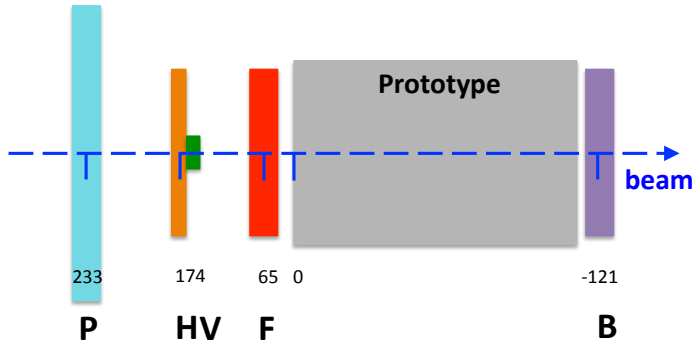


*Figure 2.9: The setup of the trigger scintillators, distance in mm.*

## 2.7 Data Readout

During data taking, there are three data taking modes – pedestal mode, beam mode and cosmic mode. Pedestal mode is used to measure the noise, so is employed when there is no beam. As there is no trigger, frames are read out continuously. Beam mode is meant to measure in an interval of relatively high intensity beam. There is a high probability that a frame will measure a particle, so readout is continuous during that interval (0.5 s). Frames have to be synchronised later with the trigger signals, which are also recorded. Cosmic mode is meant for very low intensity running, where for a trigger (coincidence of F and B for cosmics), one reads out three frames – current frame, previous and next frames.

Each data frame contains 39 million pixels, which are equivalent to 4.875 MB. The frequency of the frame readout is  $1/642 \mu\text{s}$ , thus the raw data rate of the prototype is  $\frac{4.875 \text{ MB}}{642 \mu\text{s}} \approx 7.60 \text{ GB/s}$ . Several FPGAs are used to manage this, as described in [21]. A schematic of the DAQ for one half of the prototype is shown in Fig. 2.10. Incoming trigger bits are time-stamped with the read-out clock and stored separately. A 4 GByte local buffer memory allows storing 0.55 s of pixel and trigger data. Transferred to the DAQ computer takes about 2 minutes due to the software overhead of the TCP/IP protocol. Upon completion, the DAQ system waits for the next spill signal to store another 0.55 s of data. Note that the rolling shutter and chip read-out clocks are running continuously to keep a stable phase relation between all chips. From this continuous data stream, the off-line processing reconstructs frames consisting of pixels read out up to  $642 \mu\text{s}$  after the trigger – this provides all relevant detector signals corresponding to one event.

Each sensor chip performs two steps of multiplexing – the 640 discriminators go to 16 intermediate channels, and finally to 4 output channels read out at

160 MHz. After a full read-out cycle of  $642 \mu\text{s}$ , a test pattern containing a unique ID is added to the output of every channel. The signals of 24 sensors (i.e. 96 channels) are combined by one Spartan6 XC6SLX150 FPGA, and the output of two such Spartan FPGAs is read by one Virtex6 XC6VLX240T FPGA. Two Virtex FPGAs running in a master-slave relationship are needed to read out all sensors and ship them to the DAQ computer. As a pre-processing step before analysis, the collected RAW data then have to be de-multiplexed to recover the true frame data structure. In this step, also checks on data integrity and synchronisation are performed.

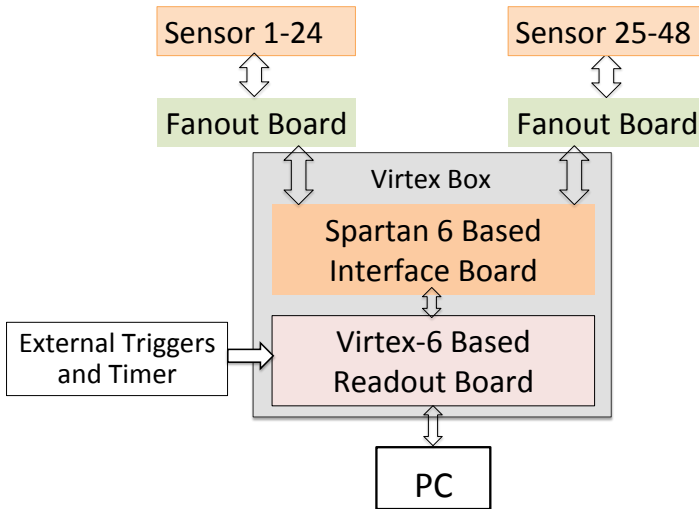


*Figure 2.10: Block diagram of readout for one half sensors of the detector.*

## 2.8 Measurement Setup

The prototype stack was mounted on a metal rail together with two scintillators to be used for triggering as shown in Fig. 2.9. The 96 PCBs of all sensors are connected to the DAQ system via flat cables attached to the sides. The scintillator PMTs are connected to the discriminators to provide trigger signals. The logical signals of the trigger are also sent to the DAQ. This setup was mounted vertically for the measurement of muons originating from cosmic rays. For these measurements only the F and B scintillators are used in coincidence to find a cosmic which passes through the prototype.

Test beam measurements have been performed at DESY and at the CERN PS and SPS, the setup was similar to the one for cosmic measurements, however

the orientation of the detector is horizontal. In addition to the F and B scintillators, three more scintillators are used (see Sec. 2.6). All trigger signals are derived as coincidences of the P (F at SPS) scintillator with at least one other scintillator.

During the test beam at DESY in 2014, the beam is quasi-continuous because of the short periodicity of beam, and a clock generated by a timer every 3 minutes provided the signal ('Spill') to start the acquisition. In addition, the information of the 5 triggers was also recorded.

At PS and SPS, there was a signal called 'Spill' from beam monitor which represented an incoming beam. The prototype took data only during spill 'on', and the other signals from the scintillators were also recorded. In the PS, there were 2 Cherenkov detectors in the beam line, and their coincidence was recorded as well for the discrimination of particle type.

The data samples taken are summarised in table 2.2.

**Table 2.2:** *Beam test overview, the properties of the different data samples collected in test beams.*

Time	Site	Particle type	Energy (GeV)
Feb 2014	DESY T22	$e^+$	2, 3, 4, 5.4
Sep 2014	CERN PS T9	$e^-, \pi^\pm, p$	2, 3, 4, 5, 6, 8, 10
Nov 2014	CERN SPS T8	$e^+, \pi^\pm$	30, 50, 100
Nov 2014	CERN SPS T8	$e^-, \pi^\pm$	244
2013-2016	Utrecht lab	cosmic	-

## 2.9 Tuning of Sensors Thresholds

There are no two identical sensors even when made by the same process. Moreover, there are three types of sensors used in this prototype, so individual tuning of the sensors is necessary. For MIMOSA 23, there are two internal bias voltages of the sensor. There is no direct access to those voltages, but they relate to DAC registers inside the sensor and the values can be varied in a range from 0 to 255.  $V_{\text{ref}2}$  is responsible for equalizing the sensor response along it as a function of column number, while  $V_{\text{ref}1}$  determines the overall sensor sensitivity with respect to the charge.

In most cases, we need a few iterations for this adjustment. In the test beam in 2012, we used reference voltages which did not provide optimal settings. Since 2014, the average noise rate per pixel was tuned to  $10^{-5}$  using pedestal data, and the settings have been verified with cosmic measurements. In layer 0, the noise level of sensors was tuned to  $10^{-5}$  for all DESY data and the 244 GeV

data of SPS, for other energies, a higher noise level of  $10^{-4}$  was used to obtain a high detection efficiency of the first layer.

A possible method to quantify the ‘non-uniformity’ of the sensor is to separate the sensor into two parts and compare the number of firing pixels on both sides. We quantify the sensor response uniformity for pedestal or cosmic via the asymmetry:

$$\chi = \frac{L_p - R_p}{L_p + R_p} \quad (2.1)$$

where  $L_p$  and  $R_p$  are the number of average fired pixels in the left part and right part respectively. The asymmetry can assume values in the range ( $-1 \leq \chi \leq 1$ ).

The asymmetry can in principle be obtained for different types of responses. Fig. 2.11 (a) shows the sensor response uniformity using the information from the pedestal file (noise), which was our main criterion for the tuning process. Similarly, the asymmetry can be extracted for the cluster size from the cosmic data, as shown in Fig. 2.11 (b). The results of the two methods are compared to each other in Fig. 2.11 (c). Apparently the two methods have very different sensitivity. The sensor response uniformity is reasonably good all over the prototype with the parameter settings used here. There are still a few sensors with a non-uniform response due to some damage on the sensors.

## 2.10 Software

The raw data transported from each fully filled memory of 4 GByte contains 814 frames. All the pixel data and trigger logical data should be aligned in time and be separated into 814 frames. This procedure is called ‘data processing’, and the combined data is called ‘processed data’. Pedestal data is taken and stored separately. The pedestal data is not only used in tuning (see above section), but also can be further analysed for the elimination of highly sensitive pixels (called *hot pixels*), pedestal estimation and so on. In the next procedure, pedestal data are analysed to find and mark hot pixels, which will be disabled in the processed data. The synchronization of each output channel is used to check whether its channel has worked in a given frame. When a frame of the processed data is recorded, the information of fired pixels, the trigger status and the frame ID are stored.

The software used [22] does not only perform the processing of raw data, but also can do some basic data analysis, e.g. from the trigger stream, one can discriminate whether pileup occurs in the prototype. It also contains a simple tracking algorithm.

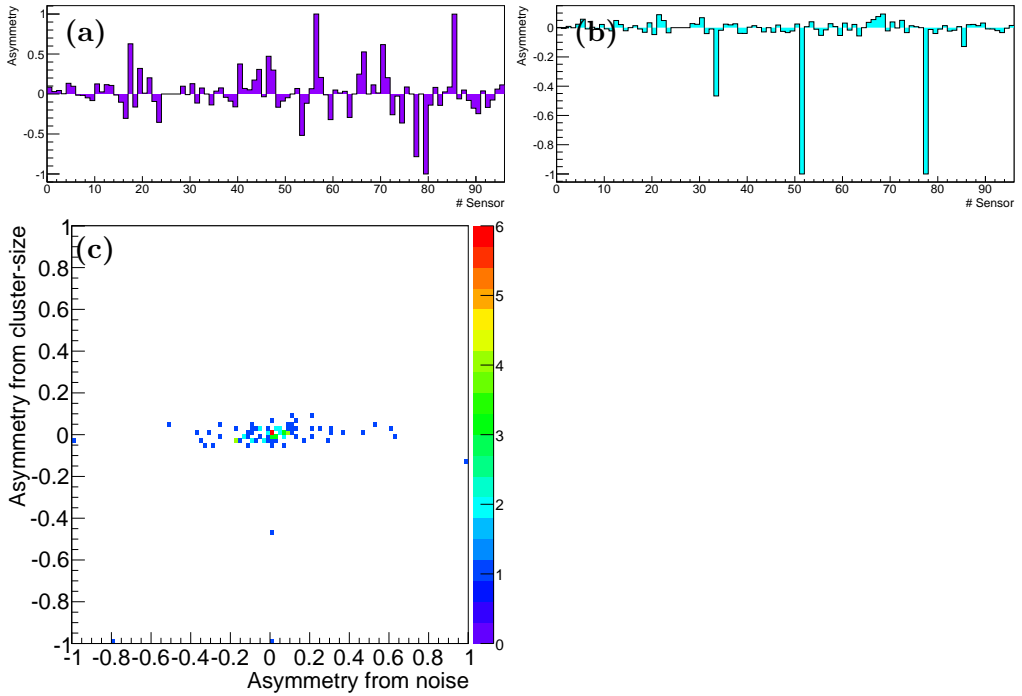


**Figure 2.11:** The uniformity of the sensor response is shown conditions for the whole detector. (a): The response uniformity using the noise information obtained from the pedestal runs. (b): The response uniformity using the cluster size information. (c): Correlation between the uniformity calculated from the sensor noise (a) and the cluster size uniformity (b).





# Chapter 3

## Data Quality

Three types of sensors were employed in the FoCal prototype, we present the raw data to illustrate properties and limitations of this prototype. The properties of the sensors will be shown using the raw distribution of hits, channel synchronization, distribution of track cluster size for cosmics and pions. The distribution of the total number of hits and longitudinal profiles will be presented for electromagnetic showers in the prototype.

### 3.1 Event Displays

Examples of typical events - an electromagnetic shower, a hadronic shower and a track are shown in Fig. 3.1. A clear shower core is found in the shower (a), most of the hits are located within a cylinder radius of  $\sim 10$  mm ( $1 R_M$ ). The shower in the longitudinal direction starts growing from the very early layer (b). These characteristics indicate that this shower is an electromagnetic shower. While the hadronic shower presents a track behaviour before developing into a shower as shown in the side view (d), moreover, the hits of the pion shower are more widely distributed and the number of hits is less than for the electromagnetic shower induced by an electron with same energy as seen in top view (c). For a track, a sequence of clusters are found along the trajectory. A hit line can be seen in side view and a spot in top view (e, f). These differences between them will be used as the basis of particle discrimination.

### 3.2 Raw Distribution of Hits

Some of the properties of the prototype can best be judged from a visual inspection of the distribution of hits. Fig. 3.2 shows the uncalibrated distributions of all the hits in all the individual layers for 244 GeV events when the central

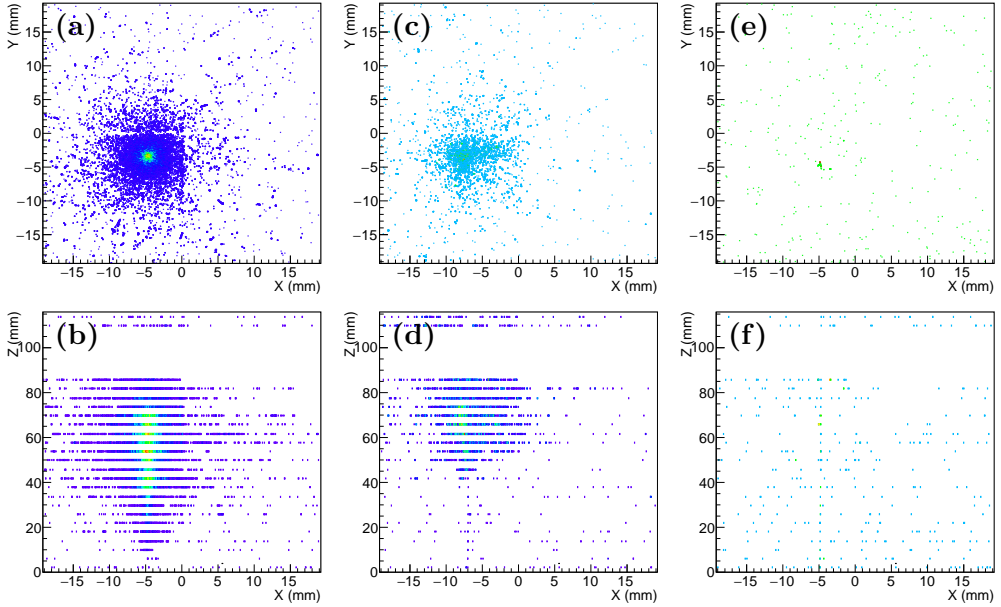


**Figure 3.1:** Typical event displays for 244 GeV raw data in top and side view when the coordinate has been redefined using alignment procedures (see Sec. 4.2). (a, b) show an electromagnetic shower, (c, d) show a hadronic shower, and (e, f) show a track. A white block before last two layers is corresponding to an absorber of 20 mm thick in each side view.

trigger is selected. Because in general, a shower does not develop in the first layer, each beam particle mostly produces one cluster which will be treated as the beam particle position. The region with relative higher hit density indicates the central trigger position which covers a  $10 \times 10 \text{ mm}^2$  ( $x: [-4, 6]$ ,  $y: [-7, 3]$ ) area. The gap region in the  $y$  direction and the overlap region in the  $x$  direction can be found visually, these gap and overlap regions exist in all layers. In addition, we notice that the width and relative position of gap and overlap regions are different from layer to layer. This indicates that the detector assembly introduces small deviations from the design geometry. An interesting line of hits appears in sensor 1, which may be related to a shower particle propagating parallel to the sensor surface. The clusters located in sensors 2 and 3 are larger than the clusters located in sensors 0 and 1, which indicates that the sensor sensitivities are not uniform. Under the same noise level setting, the type II sensor is more sensitive than type III sensor. A calibration procedure will be applied to equalise the effective gains from all the sensors. This procedure is described in Sec. 4.6. In layer 1, there are no hits in 3 channels which leads to rectangular regions without hits, which we call dead areas. 5 lines of hits in sensor 46 and

47 of layer 1, and a triangle in sensor 46 are remarkable, these pixel hits are probably not signal hits induced by beam particles, but rather from large noise. We call those hot pixels. In one channel of sensor 49 in layer 2, a significantly lower density of hits indicates that this channel is working only part of the time - it is called an unstable channel. A similar case is observed in layer 5. There is a rectangle of hits which fires occasionally. In some layers, e.g. in layer 9, the distribution of hit densities is visibly different from one sensor to another sensor. For these different sensitivities, a calibration is needed. The geometric effects (gap and overlap regions) also should be taken into account in the further data analysis. Some of the additional quality assessment and data cleaning are described in the following.

### 3.3 Channel Synchronization and Balance/Asymmetry

The dead or unstable channels as mentioned in the previous section, can be recognized via information related to synchronization. The channel synchronization is performed when the data from the scrambled format are decoded into a format that can be analysed. To reconstruct a single frame in a sensor, the internal FPGA clock is used. If the channel information cannot be used for the frame reconstruction the channel is declared ‘not synchronized’. Fig. 3.3 shows the average channel synchronization counts of one spill (814 frames), for all beam runs at SPS. The vertical white lines are corresponding to pedestal runs, and horizontal white lines to dead channels. From this figure, we find that 30 channels are completely dead, 17 channels unstable and some bad spills take place in some runs (like runs 77, 198), during the test beam at SPS.

### 3.4 Data Cleaning

As discussed above, we can identify bad spills, dead channels and unstable channels. The first data cleaning represents removing bad run and bad spills, which can be found from synchronization plots. To avoid the effects from these unstable channels, we switch off these channels completely and they will appear as dead areas in the analysis. The bad pixels, which appear in signal frames only, but not in pedestal data, will be excluded manually. Finally, we will identify and exclude the hot pixels from pedestal data.

To find the appropriate balance to keep more data and more channels, requires implementing the clean-up in the optimal order. For dead or unstable channels which only exist in a few runs, we remove these runs (e.g run 77)

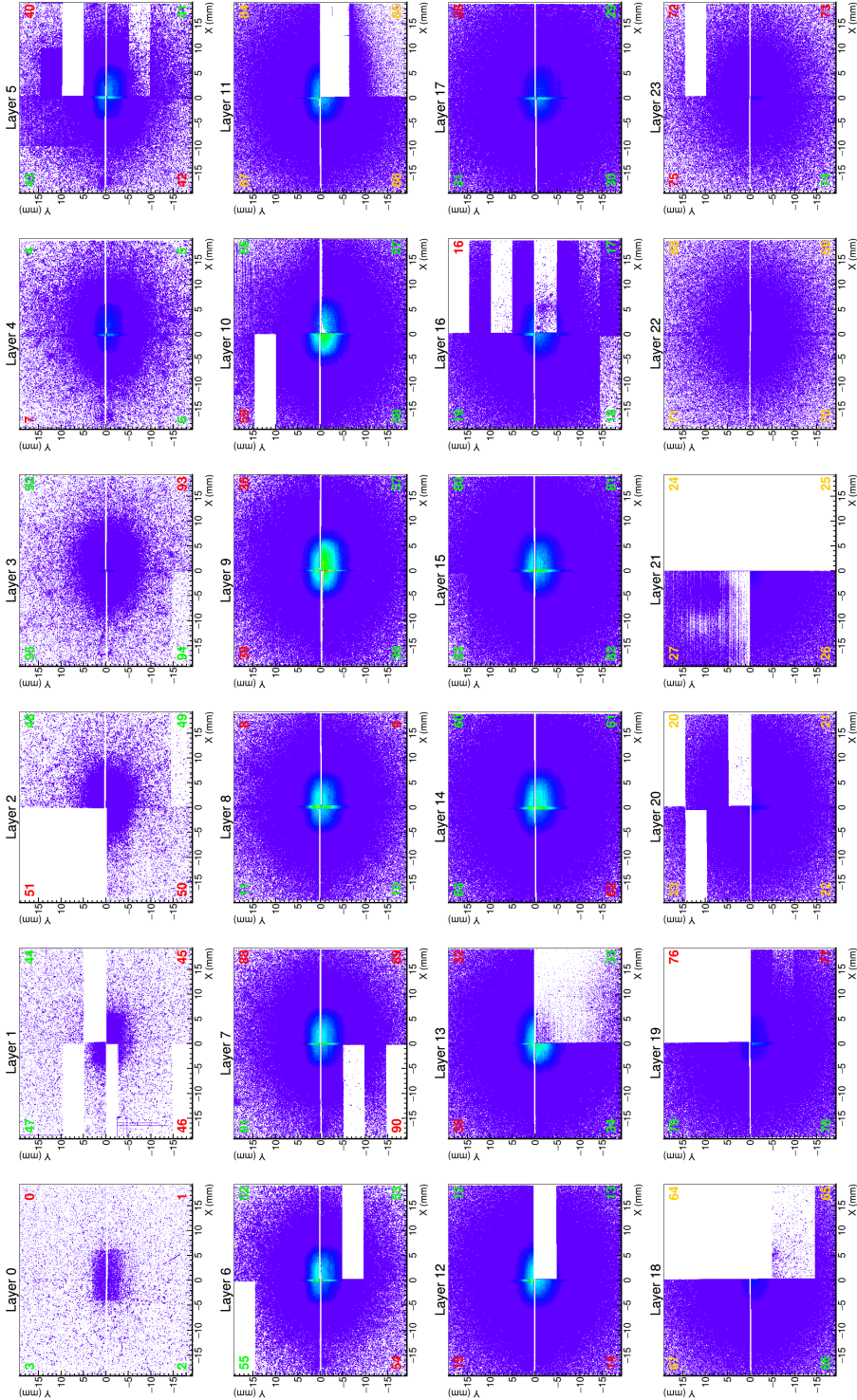


**Figure 3.2:** Uncalibrated distribution of hits in 2D at all 24 layers for raw data of 244 GeV when the central (H&V) trigger is selected with the same  $z$ -scale, bin size = 30  $\mu\text{m}$ , sensor number is marked in every corner, sensor type in color, type I: Orange = 14  $\mu\text{m}$  10  $\Omega/\text{cm}$ , type II: green = 15  $\mu\text{m}$  400  $\Omega/\text{cm}$ , type III: red = 20  $\mu\text{m}$  400  $\Omega/\text{cm}$ .

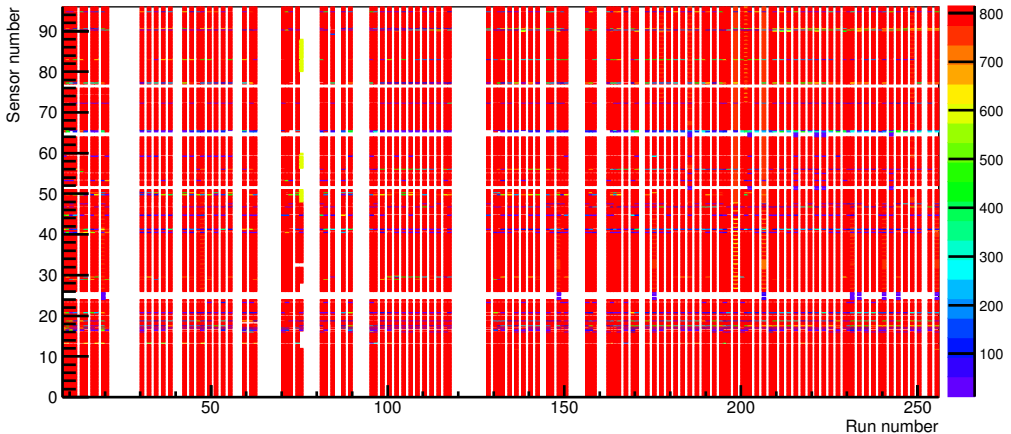


**Figure 3.3:** Channels synchronization counts as a function of sensor number and run number. The red areas (maximum synchronization count) indicate that the synchronization is in order, the white areas show a complete lack of synchronization, and the other colours mean that the channel synchronization is unstable.

instead of excluding channels. Due to the slow transfer from the Virtex box, for some spills the data transfer is incomplete. These incompletely transferred data in a spill will be removed completely. After this, faulty channels, which are visible in plots such as Fig. 3.3 will be masked. Identification of hot pixels is realised by setting a threshold of 0.01 for the average noise probability.

All plots presented in the following sections are from cleaned-up data, unless explicitly specified otherwise. Comparing with the Fig. 3.2, the distribution of the cleaned-up data (see Fig. 8.1) indicates that the data is cleaned successfully.

### 3.5 Noise

After the clean-up, e.g. removing noisy pixels, the tuned MIMOSA sensor has a remaining low noise rate of  $10^{-5}$  per pixel. For a typical good sensor, whose noise map shows a uniform distribution, we treat it as shot noise which can be regarded as random and the number of noise hits per frame can be described by a Poisson distribution. After the data cleaning procedures, some pixels are removed, especially for the sensors which have considerable removed pixels, the noise rate (average noise over live pixels) is changed. The property of sensor response for noise is studied. To obtain a uniformed noise rate of  $10^{-5}$  for live pixels, the tuning of sensors should be changed.

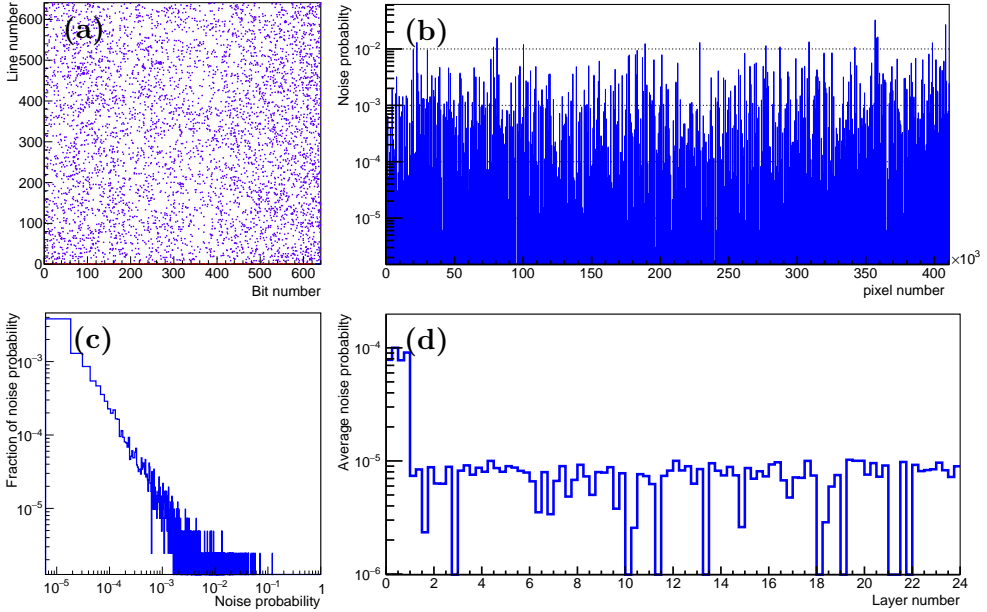


**Figure 3.4:** Distribution of noise probability over  $7 \times 10^5$  pedestal frames in sensor 7 as a function of spatial position (a) or pixel number (b). The spectrum of noise probabilities in sensor 7 (c). The average noise of all sensors (d), the four bins in an interval  $[i-1, i]$  correspond to the four sensors in layer  $i$ . The noise rate is  $10^{-4}$  for sensors in layer 0.

Pedestal data was taken without beam. The noise probability of each pixel was calculated over all pedestal runs. Fig. 3.4 shows the distribution of noise probabilities in sensor 7 in 1D and 2D, the corresponding spectrum is shown as well. The noise level of  $10^{-5}$  for live pixels has been obtained by tuning the thresholds appropriately as explained below. The average noise for all sensors is shown in Fig. 3.4 (d). The amount of random noise is stable in time.

The following procedures have been established to obtain a uniformed noise rate of  $10^{-5}$  for live pixels:

- Clean-up – Remove bad runs and spills, then exclude dead or unstable channels.
- Tune the DAC settings ( $V_{\text{ref1}}$  and  $V_{\text{ref2}}$ ) to obtain a similar noise spectrum of each sensor for the working pixels. This needs two substeps.
  - Tune  $V_{\text{ref1}}$  to obtain an average noise level of  $\sim 10^{-6}$  for most of the live pixels (90%). This can be realised by summing the noise probability from low to high until the average noise is larger than  $10^{-6}$ .
  - Tune  $V_{\text{ref2}}$  to obtain a more balanced sensor.

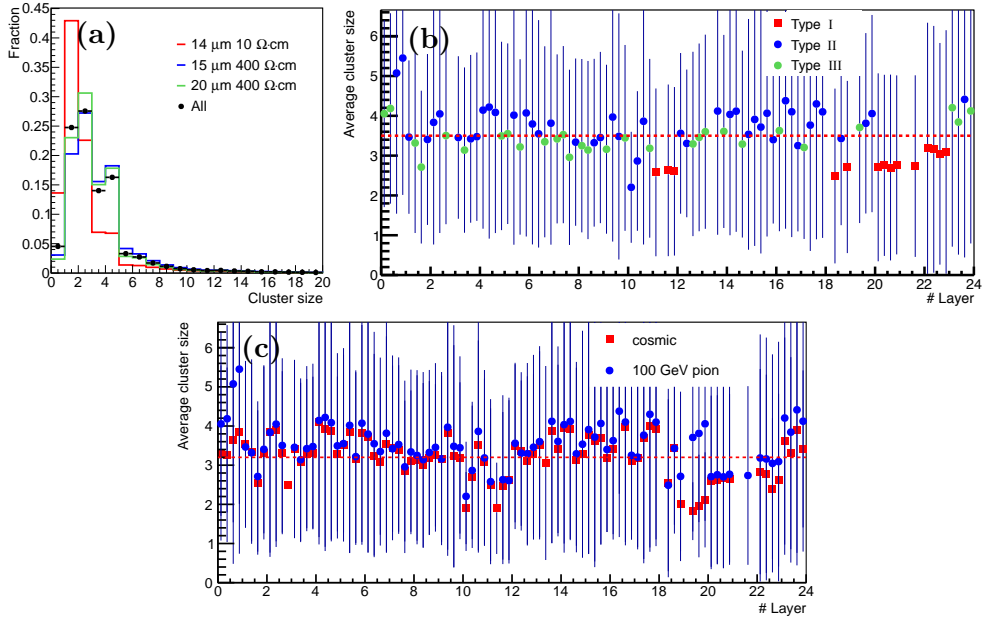


**Figure 3.5:** Distribution of cluster size. (a): Distribution of the cluster size in three types of sensors for 100 GeV pions. (b): Average cluster size of the individual sensors with error of the mean for 100 GeV pions, each layer has 4 sensors. (c): Comparison of average clusters size between cosmic and 100 GeV pions.

- Calculate and set a constant threshold for each sensor. Two substeps are also needed.
  - Mask candidate pixels with noise rate above 0.01%.
  - Accumulate low noise up to a maximum threshold, such that the average noise rate is  $10^{-5}$  per live pixel.

### 3.6 Raw Sensor Response

In this section, the initial detector properties are studied by tracks and showers. We have reported some raw results about the prototype in [27–29]. Cluster size is an important measurement to indicate the sensor response, and to check the implementation of the charge diffusion. We show the distribution of cluster size for cosmic and 100 GeV pions, and the distribution of the total number of

hits for beams. For the raw data analysis, besides data is cleaned-up, data with pile-up is rejected.

A track event is identified by two criteria:

- the number of total hits is smaller than 1000;
- these hits can be fit by a straight line with the requirement that more than half of the layers (12 layers) has hits around the straight line within 1 mm.

For a more detailed description see pages 74-76 in [22]. The clusters around the fit line are considered as induced by a track. To reduce the influence from secondary particles, we assume that the closest cluster is the cluster induced by the particle, and we use only that one cluster per layer.

The sensor response to minimum ionizing particles (MIP) was studied using cosmics and compared using 100 GeV pions. Fig. 3.5 (a) shows the distribution of average cluster size of all three types of sensor for pions, the average cluster sizes are 2.8, 3.7, 3.4 and 3.5 for type I, II, III and all respectively. The size of the cluster depends on energy deposition, charge collection mechanism, threshold, particle position and angle of the particle with the sensor.

The predefined absolute threshold ( $V_{\text{ref1}}$ ) has been tuned to obtain an average noise probability per pixel of  $10^{-5}$ . Compared to type II, type I sensors have a similar thickness of the epitaxial layer and lower resistance, type III sensors have thicker epitaxial layer and same resistance. Pions impact the prototype perpendicularly, so the mean energy deposition in type I and II should be similar and should be less than in type III. As the average cluster size of type I sensors is smaller than type II and III sensors, we can conclude that the resistance plays a key role to determine the cluster size. The varying size of clusters in one sensor can be explained by the particle location and energy loss. For instance, a larger cluster (3-4) is produced when a particle loses more energy and is located in the middle of 4 neighbouring pixels, an even larger cluster ( $\geq 5$ ) may be produced by a secondary particle with a larger angle.

The average cluster sizes of individual sensors are shown in Fig. 3.5 (b). Average cluster sizes among type I sensors have relatively smaller fluctuation than type III sensors, which in turn have smaller fluctuations than type II sensors. In Fig. 3.5 (c), the average cluster size of all sensors for 100 GeV pions are higher than for cosmics. The average cluster size is  $\sim 3.2$  for cosmic and  $\sim 3.5$  for 100 GeV pions. The difference is likely due to increasing radiative effects with higher particle energy.

Fig. 3.6 shows the distribution of the total number of hits for the different beam energies when the central trigger is selected to reduce the effect of lateral leakage. Here the noise is not subtracted.



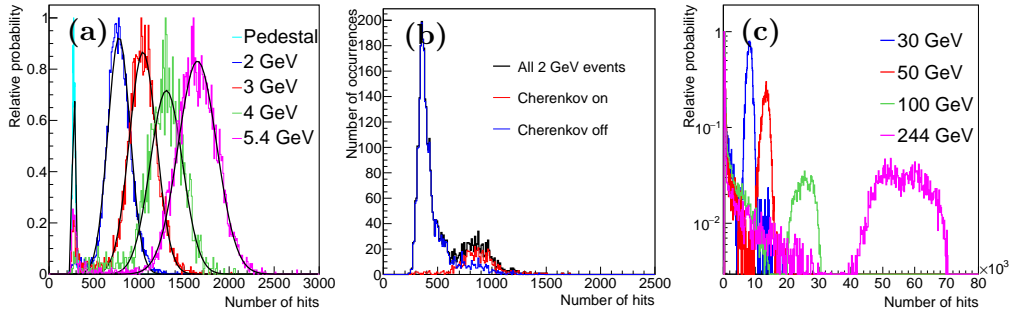


**Figure 3.6:** Distributions of the number of hits when the central trigger is selected for DESY (a), PS (b) and SPS (c) data.

For all the test beam samples, the distributions of the total number hits are broad. At DESY, the beam consists of pure positrons. The large width of the distributions is caused by the different sensitivities of the sensors and the different number of working sensors in each quadrant. The effect of the number of working sensors is so strong that even two peaks are visible for the SPS data. For PS data, due to the mixed beam, 70% of the signals are produced by pions which give the first peak at a smaller number of hits for 2 GeV, the second peak is caused by electrons. Here, particle identification can be performed by applying the cherenkov detector, as can be seen from the differently colored histograms in Fig. 3.6 (b). Unfortunately, there is only a very small fraction of electrons for the other energies at PS, only 2 GeV electron beam at the PS is used as a bridge between DESY and PS data. For SPS data, pions also contribute significantly to the beam. The signals triggered by the pion tracks are easily separated from electron events with their large number of hits. Pions can also lead to hadronic showers, which produce a tail in the hit spectrum on the right side of the track peak, ultimately reaching up to the electron peak, albeit with a very small probability. Since no cherenkov detector was used at SPS, other means of particle identification have to be used: the total number of hits and the lateral width of candidate showers.

For all the electromagnetic shower data, a clear increase of the number of hits can be seen with increasing beam energies, as expected.

Raw longitudinal profiles for DESY and SPS are shown in Fig. 3.7. The instrumental effects observed in the hit maps (Fig. 3.2) are playing an important role in degrading the FoCal detector performance. As a consequence, effects are also seen in the longitudinal profiles, e.g. the number of hits is relatively small in layer 5 (DESY) or layer 10 (SPS).

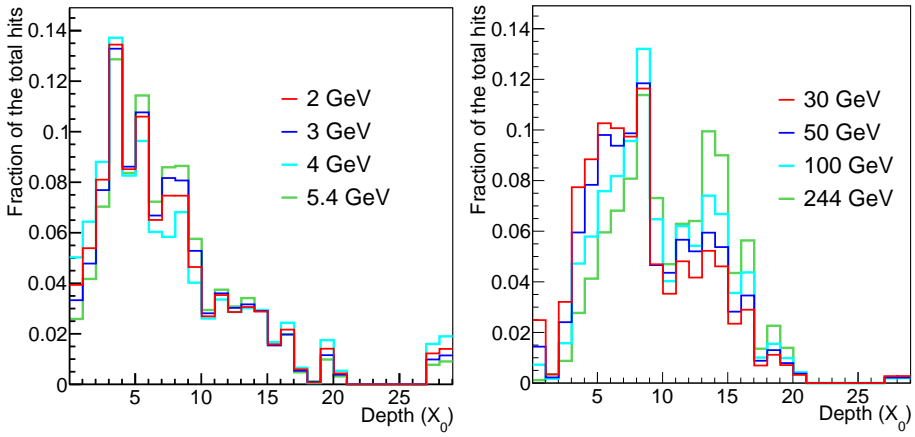


**Figure 3.7:** Longitudinal profiles for DESY (left) and SPS (right) data.

# Chapter 4

## Test Beam Data Analysis

The detector properties were tested using beams with a wide range of energy at DESY, CERN PS and SPS. The corresponding R&D studies for detector performance are carried out. In this chapter, the analysis methodology will be presented.

### 4.1 Event Selection

Since the beam at PS and SPS is not a pure electron beam (see the Table. 2.2 in Sec. 2.8), we need to identify beam particles to study the detector performance. One event can be a single electromagnetic shower, a track, a hadronic shower, noise, or mixture of these processes. We select the events that we are interested in with specific triggers and by setting cuts on the number of hits, dispersion, and position. The following procedures are applied to select one electromagnetic shower per event.

- *Cut off the events with pileup based on trigger information.*

The rate of pileup depends on the intensity. For instance, the pileup is up to 30% when beam intensity is  $\sim 250/s$  (244 GeV). This step excludes most of events with more than one particle, but not all, due to trigger inefficiency.

- *Apply a selection on the total number of hits  $N_{hit}$ .*

We know the beam energy. For a certain beam energy, the number of hits for an electromagnetic shower is much larger than for tracks and noise and would be smaller than for events with two electromagnetic showers. Events with a small number of hits and events with too many hits are excluded. The selection depends on the beam energy. The value of the

cuts was determined by inspecting the raw distribution in Fig. 3.6, and the exact values of these cuts are given in Table. 4.1.

- *Apply a selection on the standard deviation of the hit positions.*

The number of hits for a hadronic shower can be similar to an electromagnetic shower. Here, a simple cut on the standard deviation (RMS) of the hit positions is used for each SPS data set. This step is used to separate electromagnetic showers and hadronic showers. We calculate the standard deviation of the hits in the two layers with high signal-to-noise ratio and no bad sensors, before the shower maximum: layers 3 and 4.

Fig. 4.1 shows the distribution of the total number of hits and the standard deviation of the hit positions in layers 3 and 4. One expects that there are more hits and smaller dispersion for electromagnetic showers than for hadronic showers. We apply cuts on the total number of hits and the RMS to separate shower types.

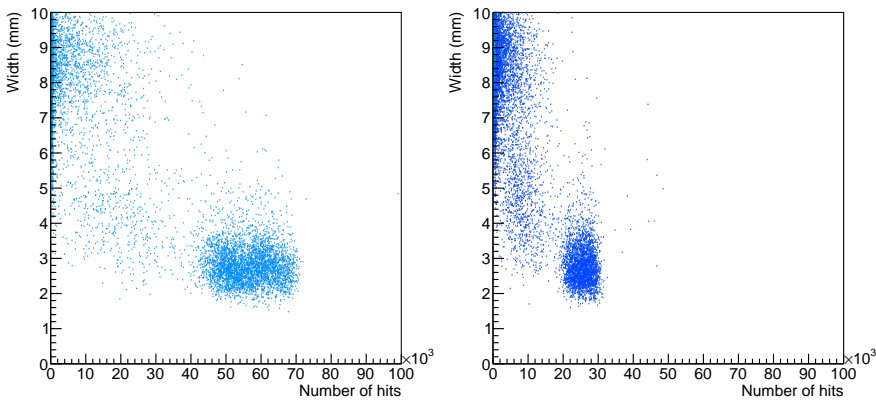


**Figure 4.1:** The distribution of the standard deviation of hit positions in layers 3 and 4 and the total number of hits for raw data 244 GeV (left) and 100 GeV (right) when  $-10\text{mm} < x, y < 10\text{mm}$  is selected.

- *Count the number of hits  $N'_{hit}$  in layers 3 and 4 and apply a selection.*

For the events which involve two particles, the calculated shower position will be between the two showers, and the fraction of the number of hits that is contained in the area around the calculated shower position to the total number of hits will be smaller than the same ratio for events with only one particle. This cut rejects double shower events.

- *Select events within 10 mm in the  $x$  and  $y$  direction from the detector center.*

Such that showers are well contained within the detector. The approximate shower position is determined following the procedures described in Sec. 4.3. This selection is based on the shower position, instead of using the central trigger, to increase the event sample.

To refine the discrimination, the selections are carried out after calibration for sensor sensitivity.

The selection procedure outlined above is used to select electromagnetic showers. For alignment and hadronic shower studies, tracks and hadronic showers are also used. Tracks are selected by taking only events with  $N_{hit} < 1000$ , where the candidate hits can be fitted by a straight line.

For hadronic showers, the number of hits most likely is between a track and an electromagnetic shower. A few hadronic showers with a larger number of hits are identified by the dispersion of hit positions. Table. 4.1 summarises the selection criteria for different event types.

**Table 4.1:** *Cuts applied for selection of events.*

Beams	No pile-up	Total $N_{hit}$	RMS(mm)	$N'_{hit}$	$-10\text{mm} < x, y < 10\text{mm}$
30 GeV	✓	5800-11000	<4.8	>50	✓
50 GeV	✓	9500-16000	<4.5	>50	✓
100 GeV	✓	18000-32000	<4.0	>120	✓
244 GeV	✓	40000-72000	<3.6	>120	✓
Track	✓	<1000	-	-	
Hadronic shower	✓	1000-70000	-	-	✓
DESY data	✓	-	-	> 30	✓

## 4.2 Tracking and Alignment

The coordinate system is defined in Sec. 2.5. The position and orientation of the sensors are specified in the reference system by their position in  $x$  and  $y$  and a rotation angle around the  $z$  axis. The position in the  $z$ -direction is calculated from the measured layer thickness and the tilts in the  $yz$  and  $xz$  planes are ignored.

The sensors alignment is crucial and is the first step for an accurate shower core position estimation. All the sensors are aligned using muon tracks from cosmic rays, which are better than pion tracks from beam because the cosmic

muons have a range of incident angles, and inclined tracks cross more than one quadrant, thus providing relative alignment between the quadrants. The misalignment of a sensor can be described with three degrees of freedom,  $\Delta X$ ,  $\Delta Y$ ,  $\theta$ , the movements in the  $x$  and  $y$  directions and a rotation angle  $\theta$  around the  $z$  axis respectively. The transformation is a rotation by an angle  $\theta$  in the sensor plane, followed by a translation  $(\Delta X, \Delta Y)$ . So the sensor-coordinates in term of the global reference system are:

$$X_{new} = X_{old} \cos \theta + Y_{old} \sin \theta + \Delta X, \quad (4.1)$$

$$Y_{new} = Y_{old} \cos \theta - X_{old} \sin \theta + \Delta Y \quad (4.2)$$

### 4.3 Shower Position Determination

The shower position in layer 0 should be the most accurate since a high energy electron going through the first layer will generate a single cluster, but the shower does not start. A single track cluster is however susceptible to noise. To avoid picking up clusters which are not related to the shower, we will calculate the ‘approximate shower position’ first, which is determined in early layers, and then find the cluster closest to this approximate shower position in layer 0. The approximate shower position determines the search range and the sensitivity to noise. So we want an approximate shower position that is as precise as possible. The procedure that is used to determine the approximate shower position can be described in the following three steps, the ‘final shower position’ in the last step. The resolution of the final shower position is better than the approximate shower position, but a disadvantage is that there are no available hits in the gap between the sensors at  $y \approx 0$  to determine shower position.

1. *Find the centre of gravity of the  $N$  hits in layers 3 and 4.*

$$(x, y)_{3,4} = \frac{1}{N} \sum_i^N (x_i, y_i) \quad (4.3)$$

2. *Reduce the search range in layers 3 and 4 and repeat the calculation of the centre of gravity.*

Because the hits include signal and noise, and the signal-to-noise ratio becomes lower far from the shower axis, the calculation is repeated using only hits in a limited radial distance around the estimated position  $(x, y)_{3,4}$  for selected layers. The search area can be gradually narrowed with a

simple iteration formula:

$$r = (l + 2 - (n - 1)) \text{ mm} \quad (4.4)$$

Where  $l$  is layer number 3 and 4, and  $n$  is the iteration number. In each iteration, the search is performed around the center of gravity obtained from the previous iteration. From studies of the lateral distribution (see Sec. 6.1.2), we know that 90% of the hits are contained in layer 3 within  $r = 5$  mm, and in layer 4 within radius  $r = 6$  mm. So the search area starts from  $r = 5$  mm for layer 3, and  $r = 6$  mm for layer 4. We obtain the centre  $(x, y)_l$  of the selected hits for each selected layer. The iteration stops when the minimum search area of  $r = 1$  mm is reached for both selected layers 3 and 4.

### 3. Combine information of layers 3 and 4.

The approximate shower position becomes:

$$(x, y)_{3,4} = \frac{1}{2} \left( \frac{1}{N_1} \sum_i^{N_1} (x_i, y_i) + \frac{1}{N_2} \sum_j^{N_2} (x_j, y_j) \right) \quad (4.5)$$

where  $N_1, N_2$  are the number of hits in layers 3 and 4 respectively within  $r = 1$  mm.

### 4. Calculate the final shower position.

The final shower position is calculated by searching for clusters in layer 0 within 1 mm from the approximate shower position determined from layer 3 and 4. Fig. 4.2 left shows the distribution of the distance of hits in layer 0 to the estimated shower position with Eq. 4.5. Fig. 4.2 right shows the distribution of cluster size of all clusters and selected clusters. The centre of gravity of the cluster closest to the approximate shower position in layers 3 and 4 is used as the final shower position. Events with no hits or with 12 or more hits in the range  $r < 1$  mm are rejected to further remove events where the shower position is not well defined.

Because the sensor sensitivities are not identical, the procedure of calculating the centre of gravity of hits is repeated after calibration. Eq. 4.3 then becomes:

$$(x, y)_{3,4} = \frac{1}{\sum_i^N c_i} \sum_i^N (c_i \times x_i, c_i \times y_i) \quad (4.6)$$

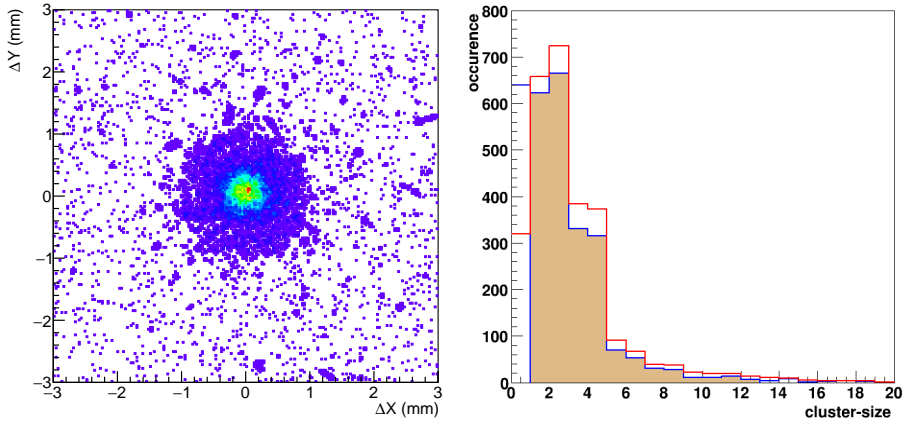


**Figure 4.2:** *Left: distribution of the distances of hits in layer 0 to the approximate shower position. Right: distribution of the cluster size in the search area (blue) and for all clusters (red). The filled area represents the range of selected events.*

where  $c_i$  is the calibration factor of the sensor in which hit  $i$  is located, see Sec. 4.6. The resolution of the approximate shower position determined in layers 3 and 4 is energy dependent, because the number of hits increases with energy. The final shower position is determined by a cluster position in layer 0, for which the position resolution is energy independent.

The central trigger is determined by a coincidence of signals of the H and V scintillators signals (Sec. 2.6) which cover  $10 \times 10 \text{ mm}^2$  and which are mounted in front of the detector. Fig. 4.3 shows the shower position for events with a central trigger. A projected intensity profile is taken across the sharp edge. The profile is fitted (red) with a cumulative Gaussian function:

$$F(x) = \frac{1}{2} \left[ 1 + \operatorname{erf}\left(\frac{x - \mu}{\sqrt{2}\sigma}\right) \right] \quad (4.7)$$

The parameter  $\sigma$  describes the sharpness of the edge of the distribution. In the ideal case, this gives an estimate of the position resolution for showers. However this  $\sigma$  also contains effects related to the accuracy of the definition of the edge of the scintillator. The obtained value should be regarded as an upper limit for the resolution. For 100 GeV showers, the smallest  $\sigma = 0.07 \text{ mm}$  is found for the top side (positive  $y$ ). This value shows that the final position is very accurate, and the resolution of shower position found with other methods can be obtained by comparing to it [30].



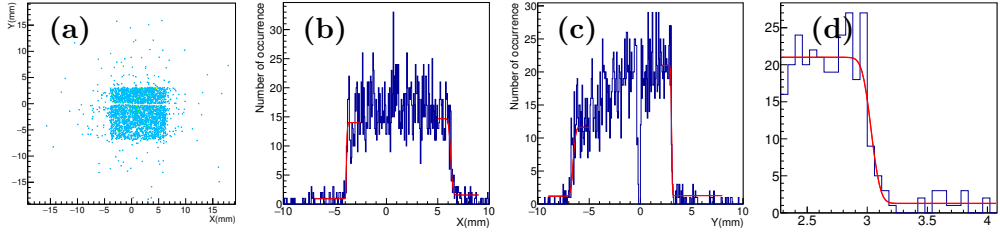


**Figure 4.3:** Shower position distributions with the central scintillator trigger. (a): Distribution of the shower positions in 2D when the central trigger is selected. (b, c): Projection of the shower positions onto the  $x$  and  $y$  coordinate with a fit of an Error function Eq. 4.7. (d): The distribution for the sharpest edge shown on a different scale.

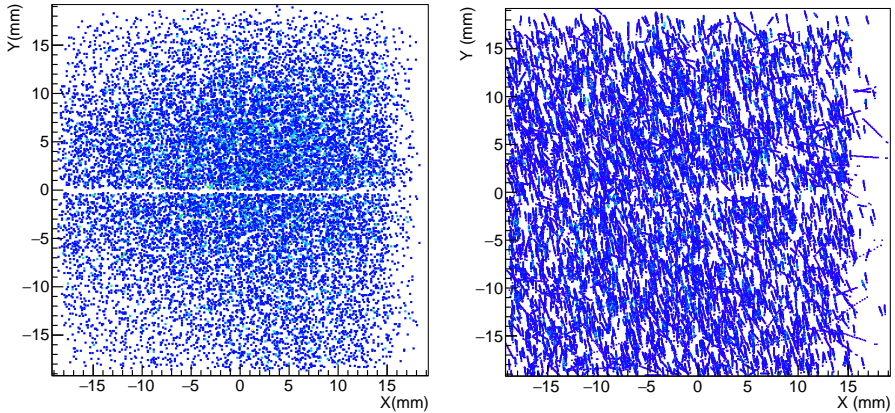


**Figure 4.4:** Shower position for 100 GeV positrons (left) and projection of 100 GeV pion tracks (right).

## 4.4 Inclination of The Beam

The inclination of the beam with respect to the setup has been measured using tracks from the beam. The beam at PS and SPS beams are mixed beams, which are produced by interactions of a primary beam with a target. The beam line optics provide a narrow momentum selection, with a spread of 1.3%. The distribution of shower position for 100 GeV positrons and the distribution of projections for pion tracks are shown in Fig. 4.4. Since both types of particles have a similar distribution, we can conclude that the spatial distribution of pions and positrons in the beam is similar (the two beam distributions were different in the 2012 beam test). Therefore, we can assume that the inclination of both beams are equal as well, so that the inclination measured with pion

tracks can be used to calculate the change of the shower positions from layer to layer. The projection of all pion tracks on the transverse plane is shown in Fig. 4.4 right. It indicates a preferred direction of the tracks, corresponding to a common angle of inclination of the beam. The inclination can be calculated from the displacement of the pion tracks between the first and the last layer. Fig. 4.5 left shows the distribution of this displacement. The values cluster in a narrow spot at  $\Delta x = 0.2$  mm and  $\Delta y = 0.97$  mm, which indicates that the particles in the beam are on parallel trajectories, with a finite inclination in the  $x$  and  $y$  direction corresponding to an inclination angle of  $0.4^\circ$  relative to  $z$  direction. We can use this to calculate hit coordinates corrected for this inclination according to:

$$x = x_0 + l \times 0.007 \text{ mm} \quad (4.8)$$

$$y = y_0 - l \times 0.035 \text{ mm} \quad (4.9)$$

for layers 0-21. Between layers 21 and 22, there is a tungsten block of 20 mm thick, corresponding to 5 layers, therefore we use  $l+5$  instead of  $l$  for layers 22 and 23. Fig. 4.5 right shows a comparison of hit densities in layer 17 as a function of distance from the shower axis before and after correction for the inclination. Without the correction, there is a minimum in the hit density for very small distance  $r$ , which is removed by the correction. The width of the spot (in Fig. 4.5 left) is a convolution of beam divergence, tracking accuracy and alignment errors. These terms are thought so small that can be ignored in our analysis.

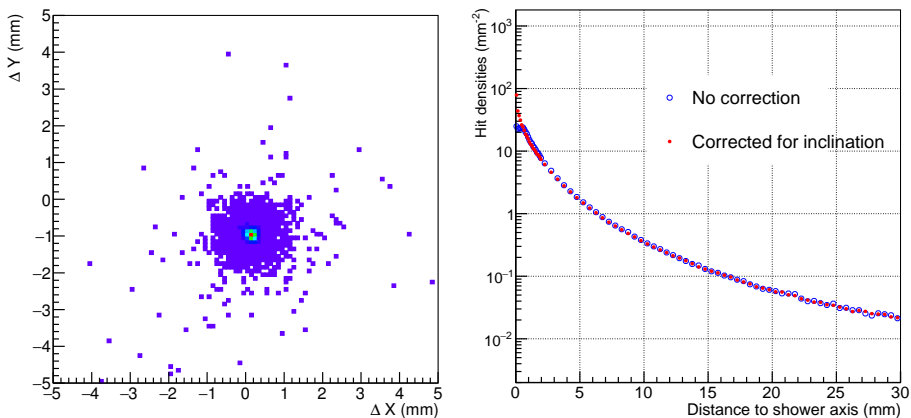


**Figure 4.5:** Left: displacement between the first and the last layer of projected tracks for 100 GeV pions. Right: distribution of hit densities for layer 17 before and after inclination correction.

## 4.5 Measurement of Hit Densities

The lateral distribution of hit densities as a function of the distance  $r$

$$r \equiv \sqrt{(x - x_s)^2 + (y - y_s)^2} \quad (4.10)$$

from the shower axis  $(x_s, y_s)$  is obtained by counting the number of hits. Each layer is divided into narrow rings around the shower axis, and the hit density in a sensor  $(l, q)$  is calculated as:

$$\nu_{l,q}^0(r) = \frac{\Delta N_{\text{hit}}^{l,q}(r) - \Sigma p_i}{\Delta N_{\text{pixel}}^{l,q}(r) \cdot (30\mu\text{m})^2} \quad (4.11)$$

where  $\Delta N_{\text{hit}}^{l,q}(r)$  is the number of hits in a ring for a given sensor,  $\Delta N_{\text{pixel}}^{l,q}$  is the number of counted live pixels within this ring and  $\Sigma p_i$  is the total measured noise contribution, which is obtained by summing the noise probability  $p_i$  over the live pixels. Because both the number of hits and the area used are from live areas, the effects of dead areas and the areas where sensors overlap in the ring are corrected for. The dead areas of the detector include dead sensors, dead channels, masked pixels, the gaps between sensors and even the areas where no sensor covers. To investigate the lateral shower development in detail, especially for the shower core region, the step size is 0.1 mm for  $r < 2$  mm and 0.5 mm for  $r > 2$  mm.

In principle, the distribution of hit densities for one layer can even be obtained from only a small live area. For one ring, the larger the number of live pixels in a ring and the lower the noise, the more accurate the measurement is. For each layer, we determine the distribution of hit densities from individual sensors. From differences in the distribution of hit densities of hit densities, information of the different sensors is obtained. The cumulative distribution is

$$M_{l,q}(R, \langle \nu_{l,q} \rangle) \equiv \int_0^R 2\pi r \langle \nu_{l,q}(r) \rangle dr \quad (4.12)$$

where the brackets  $\langle \rangle$  indicate an average over the analysed events and  $l, q$  are the layer number and quadrant number. These two numbers identify a sensor, so  $\langle \nu_{l,q} \rangle$  is the mean hit density in this sensor and  $\langle \nu_{l,q}(r) \rangle$  is the mean hit density in a given sensor at distance  $r$  to the shower axis. When the sensor sensitivities are identical, the mean hit density distributions are the same for all

of the sensors  $(l, q)$  in the same layer.

$$M_l(R, \langle \nu_l \rangle) = \frac{1}{4} \sum_{q=0}^3 M_{l,q}(R, \langle \nu_{l,q} \rangle) \quad (4.13)$$

The dead sensors will be ignored in this procedure.

## 4.6 Instrumental Calibration

In the FoCal prototype, the sensitivity varies from sensor to sensor, due to the different threshold settings, the use of three types of sensors with different thickness of the epitaxial layers and different specific resistivity (see Sec. 2.2), and the natural variability of the production process. Moreover, 16.7% (at SPS) of the pixels are masked, which include dead pixels, unstable pixels, hot pixels and pixels with higher noise probabilities. These instrumental effects will affect the detector performance. To achieve the best possible accuracy, a calibration for the sensor sensitivity and a correction for the dead areas have been developed and are presented below.

A previous attempt to calibrate the detector using pion tracks, did not achieve the expected resolution [22]. One reason for the unsatisfactory results may be the difference of the number of hits induced by a MIP and a shower particle. A MIP goes through the detector perpendicularly or with a very small angle, but shower particles have a distribution of angles with respect to the sensor surface, these differences can be found in simulation Sec. 5.1. Even when the energy depositions are the same, the number of hits induced can be different.

The calibration in the present work is based on the measurement of the distribution of hit densities in both longitudinal and lateral direction using all selected electromagnetic shower events at a given energy. The correction for dead areas is based on the hit densities after calibration, and is implemented event by event.

The calibration is carried out in the following steps.

- Equalise the response in each layer, using calibration constants

$$c_{l,q}^0 \equiv \frac{M_l(R, \langle \nu_l \rangle)}{M_{l,q}(R, \langle \nu_{l,q} \rangle)} \quad (4.14)$$

where  $M_{l,q}(R, \langle \nu_{l,q} \rangle)$  are the hit multiplicities defined in Eq. 4.12.

- Inter-layer calibration by fitting the longitudinal profile using equalised hit multiplicities  $M_l^{fit} = c_l M_l$ .  $M_l^{fit}$  is the expected number of hits from

the fit to the longitudinal profile based on the hit densities  $M_l(R, \langle \nu_l \rangle)$ . This fit is then used to calculate the final calibration constants

$$c_{l,q} \equiv \frac{M_l^{fit}}{M_{l,q}(R, \langle \nu_{l,q} \rangle)} = \frac{M_l^{fit}}{\int_0^R 2\pi r \langle \nu_{l,q}(r) \rangle dr}, \quad q = 0, 1, 2, 3, \quad (4.15)$$

- The calibrated hit density for each shower is then

$$\rho_l(r) = \frac{\sum_{q=0}^3 c_{l,q} (\Delta N_{l,q}(r) - \Sigma p_{l,q}^i(r))}{\Delta N_{\text{pixel}} \cdot (30\mu\text{m})^2} \quad (4.16)$$

where  $\Delta N_{l,q}(r)$  is the number of hits in in the ring with radius in sensor  $(l, q)$  and  $\Delta N_{\text{pixel}}$  is the number of live pixels in layer  $l$ . The expected noise is subtracted using the noise probabilities  $\Sigma p_{l,q}^i(r)$  which is the sum of noise probabilities in the current ring and sensor  $(l, q)$ .

- The calibrated number of hits in layer  $l$  is

$$L_l(R) \equiv \int_0^R 2\pi r \rho_l(r) dr \quad (4.17)$$

#### 4.6.1 Relative sensitivity calibration within each layer

The equalisation of the sensor response in each layer using the average hit densities to obtain the calibration factors in Eq. 4.14 is based on the following assumptions:

- (i) Each electromagnetic shower develops symmetrically around the shower axis in the detector for small inclination angle. On average, the hit densities in the same layer, at the same radial distance, are the same.
- (ii) The beam impacts the detector perpendicularly to all the layers after the correction in Sec. 4.4.
- (iii) Any sensor asymmetry is neglected, i.e. in a single sensor, the sensitivities of all pixels are assumed to be the same.

The uncorrected distribution of hit densities for each sensor has been obtained for beams of various energies. The upper panel in Fig. 4.6 left shows an example of these profiles for layer 4 in selected electromagnetic shower events with beam energy 50 GeV. The average hit density for a layer  $l$  at distance  $r$  to the shower position is  $\nu_l(r) = \frac{1}{4} \sum_0^3 \langle \nu_{l,q}(r) \rangle$ . So the ratio of the hit density for individual sensor to the average is

$$V_{l,q}(r) = \frac{4 \langle \nu_{l,q}(r) \rangle}{\sum_0^3 \langle \nu_{l,q}(r) \rangle} \quad (4.18)$$

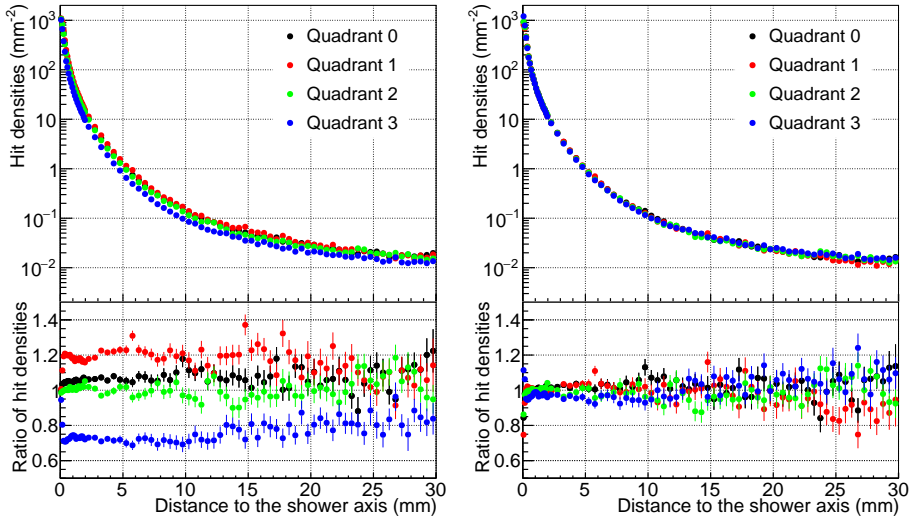


**Figure 4.6:** Lateral profiles and the ratio of hit densities (lower panels) for each sensor in layer 4 for 50 GeV positrons before (left) and after (right) sensor sensitivity calibration within the layer.

which is shown in the lower panel in Fig. 4.6 left.

In the first step, the sensitivities of 4 sensors in the same layer are made uniform by multiplying the 4 hit density distributions using a single factor for individual sensors. Because of the noise, sensor asymmetry and statistics, the distribution of ratio values fluctuates. We calculate the 4 factors for one layer from Eq. 4.14 with  $R = 18\text{mm}$ , to exclude regions where the noise dominates. Fig. 4.6 right shows 4 lateral distributions of hit densities in layer 4 after this step which now lie very close together. The lower panel shows the ratio of the hit density profiles in each individual sensors to the average.

#### 4.6.2 Response calibration between the layers

The calibration constants will equalise the mean hit densities in the same layer at the same  $r$ . As a second step, the number of hits in all layers will be matched to a Gamma distribution. The calibration factors of the sensors should be constant and can be calculated using any beam energy. The 50 GeV positron beam data is selected for this purpose.

The longitudinal profile is obtained by accumulating the mean hit densities  $\langle \nu_l(r) \rangle$  per layer. As mentioned, a Gamma distribution Eq. 1.10 can describe this profile reasonably well:

$$\frac{dN}{dt} = N_0 \beta \frac{(\beta t)^{\alpha-1} e^{-\beta t}}{\Gamma(\alpha)} \quad (4.19)$$

The parameters  $N_0$ ,  $\alpha$  and  $\beta$  depend on energy. In this step, the 3 free parameters are found by fitting the mean longitudinal profile of 24 layers of hits with the Gamma function. A calibration constant for each layer is obtained by comparing the measured number of hits to the value of the fit function:  $M_l^{fit} = c_l M_l$ . The final calibration factors are  $c_{l,q} \equiv c_{l,q}^0 \times c_l$ . The two steps above can be combined in a single calculation as in Eq. 4.15

The second step relies on a successful calibration for the sensors within the layers as a prerequisite. Alternatively, one can pick one good sensor per layer, obtain the number of hits per layer from an integral of the density in the single sensor and use that information in a similar fit procedure to the longitudinal profile (see Fig. 4.7 left). The selection of good sensors depends on the sensor type and cluster size. As Fig. 3.5 shows, the type III sensors have the most similar response for 100 GeV pions. The second option is type II if there is no type III sensor in the layer.

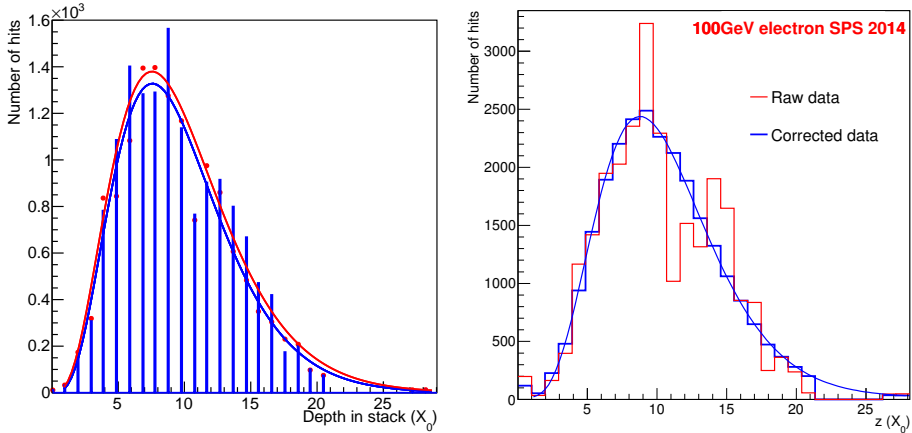


**Figure 4.7:** Longitudinal profiles. Left: in the blue histogram, the number of hits in each layer is the integral of hits  $M_l(R, \nu_l)$  from average hit densities, the red dots present the number of hits  $M_l(R, \nu_{l,q})$  from selected good sensors for 50 GeV positron showers. The corresponding fits with the Gamma function are shown in the same color as the data. Right: comparison of the longitudinal shower profiles for 100 GeV positron showers between: raw (red) and corrected (blue) data.

### 4.6.3 Calibration constants

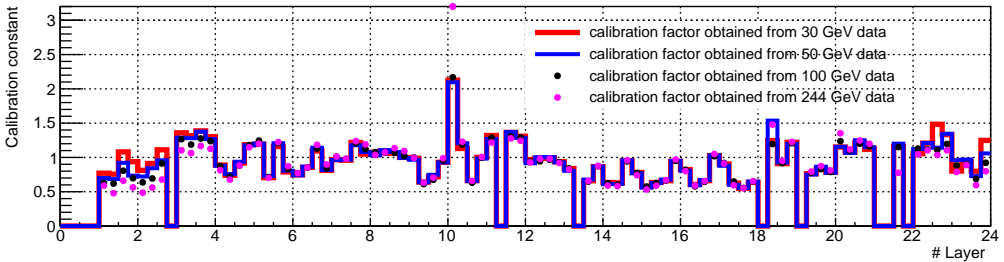


*Figure 4.8: Calibration constants obtained from data at different energies.*

The calibration constants for all functioning sensors are shown in Fig. 4.8. Differences between these constants appear in the layers 1-3 and the last two layers. Because the calibration constants are obtained from hit density analysis, the smoothness of the distributions of hit densities like those examples in Fig. 4.6 indicates that there is no large fluctuation in a large range and thus the densities can be integrated over  $r$  to measure the longitudinal profile. To verify the stability of the calibration procedure, all the longitudinal profiles of SPS energies are shown with fit curves in Fig. 4.9. For all the layers and all the SPS data, the fits provide reasonably good descriptions and the differences of the number of hits in each layer and the value at the corresponding fit point is similar for all energies. However, for layers 1-3, the fit values are consistently low and thus the corresponding calibration constants smaller than 1, same for the last one layer. It indicates that the Gamma function may not fit the longitudinal profile well for the first and last layers. In page 262 of PGD, as reported the Gamma function fails badly for about the first two radiation lengths [32]. Other small problems appear for a few sensors: sensor (10,0) are unstable when taking 244 GeV data. For sensors (18,1) and (20,0) statistics is very low, the settings of sensor (21,2) were changed during test beam.

### 4.6.4 Calibration quality

So far we have got the calibration factors for all sensors. The calibrated hit density in layer  $l$  is calculated by multiplying the number of hits in each sensor  $(l, q)$  by the corresponding calibration constant, see Eq. 4.16

To check the calibration quality, we compare the lateral profiles in selected layers containing different types of sensors for different energies as shown in Fig. 4.10. For an early layer, e.g layer 4, the ratio of corrected hit densities is constant in the range  $2 < r < 8$  mm. At the closest distance to the shower



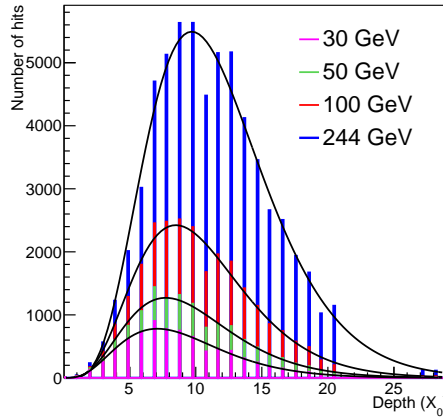


**Figure 4.9:** Longitudinal profiles with Gamma function fit curve. The number of hits is calculated using the calibration constants determined from the 50 GeV positron beam.

axis, the ratio slightly deviates from 1. Larger fluctuations of the ratio appear at a large distance to the shower axis due to the increasing contribution from noise hits. For a mid layer, e.g layer 9, there is a deviation at a very close distance to the shower axis for high energy, however, the ratio quickly reaches 1 for larger distance. For later layers, e.g layers 14 and 18, the ratio shows a good calibration. The deviations close to the shower axis are probably due to the saturation.

#### 4.6.5 Correlation between calibration constants and cluster size

A comparison between calibration factors and cluster size is shown in Fig. 4.11. There is no strong connection between two, especially for type II sensors. A MIP calibration would use cluster size information to calibrate the detector. The large spread in Fig. 4.11 is one of the reasons why the MIP calibration does not provide satisfactory energy resolution and has not been used in this work.

#### 4.6.6 Hit density extrapolation method for dead area

The hit density based signal measurement corrects for dead areas in each layer using rotational symmetry. There is, however, a special situation in case the shower center falls inside a dead area. The full procedure is outlined in this section. The correction procedure for dead areas starts from the calibrated hit densities.

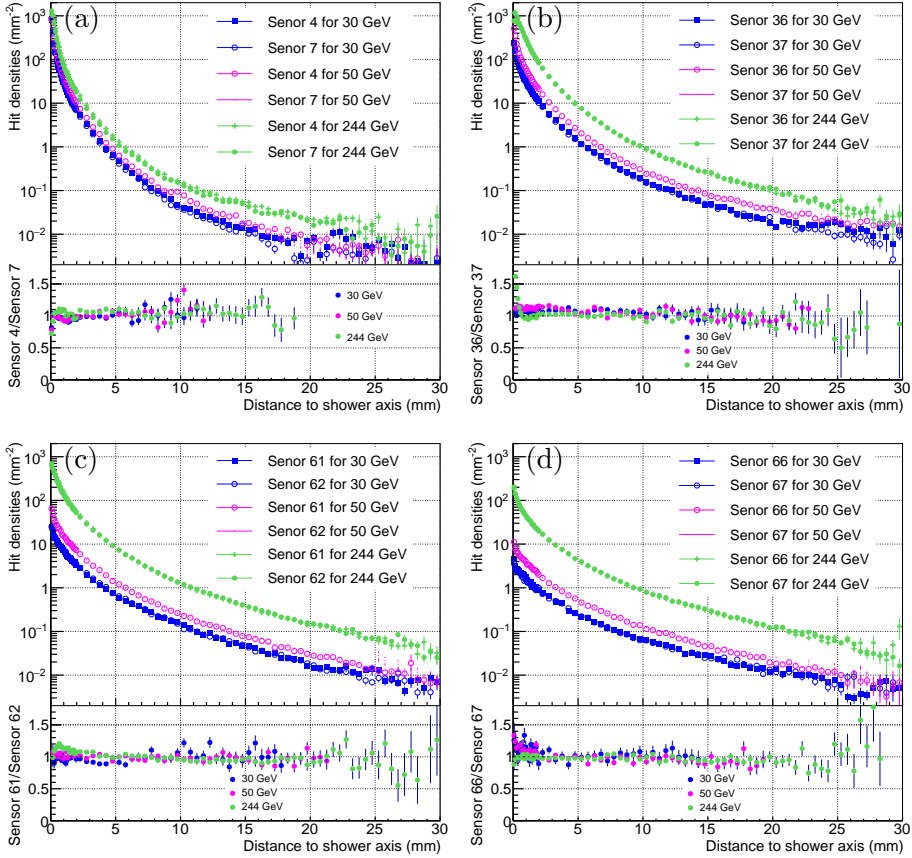


**Figure 4.10:** Comparison of the lateral hit density profile from different sensors in layers 4, 9, 14 and 18 (a, b, c and d respectively). The lower panels show ratios of one sensor over another. The ratio points are only drawn when the hit density is more than twice the noise density. Sensors 4, 37, 61 and 66: 15  $\mu\text{m}$  thick with 400  $\Omega/\text{cm}$ ; sensors 7, 36 and 62: 20  $\mu\text{m}$  thick with 400  $\Omega/\text{cm}$ ; sensors 67: 14  $\mu\text{m}$  thick with 10  $\Omega/\text{cm}$ .

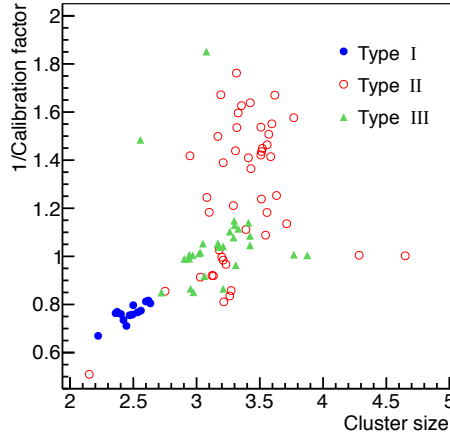


**Figure 4.11:** Calibration factors obtained from 100 positron showers vs the average cluster size for 100 GeV pion tracks.

For each ring, the number of hits in this ring is calculated according to different procedures for the following cases classified by the number of live pixels  $\Delta N_{\text{pixel}}$ :

*case 1* :  $\Delta N_{\text{pixel}} > 0$ . The hit densities in the dead area are assumed to be the same as in the live areas with the same distance to the shower axis. The number of hits in each ring will then be the hit density times the total area of the current ring, as in Eq. 4.11. With this assumption, the corrected number of hits is calculated by multiplying the hit density in the live area by the total ring area. To illustrate the procedure, Fig. 4.12 (a) shows the hit distribution in layer 6. The total number of hits in this ring is the hit density  $\rho_l(r)$  calculated in the live area indicated by the red line times the total area in this ring. Thus the blue dead area is corrected by using hits in the red live area.

*case 2* :  $\Delta N_{\text{pixel}} = 0$ . If a shower is located in a dead area, the rings close to the shower axis contain no counts and no live pixels. In this case,  $\rho_l(r)$  is estimated from the measured densities in the preceding and following layers  $\rho_{l-1}(r)$ ,  $\rho_{l+1}(r)$ . Fig. 4.12 (b) and (c) show two examples of the hit densities as a function of depth at  $r = 2$  mm and  $r = 4$  mm from the shower axis. The hit densities gradually change along the depth. The hit density is estimated by a linear interpolation:

$$\rho_l(r) = \frac{1}{2}[\rho_{l-1}(r) + \rho_{l+1}(r)] \quad (4.20)$$

when there are contiguous layers with dead areas at same range, the above estimation equation is changed as  $\rho_l(r) = \rho_{l-m}(r) + \frac{m}{m+n}[\rho_{l+n}(r) - \rho_{l-m}(r)]$ , where  $n$  and  $m$  are chosen such that layer  $l - m$  and later layer  $l + n$  are the nearest layers with working pixels in current ring.

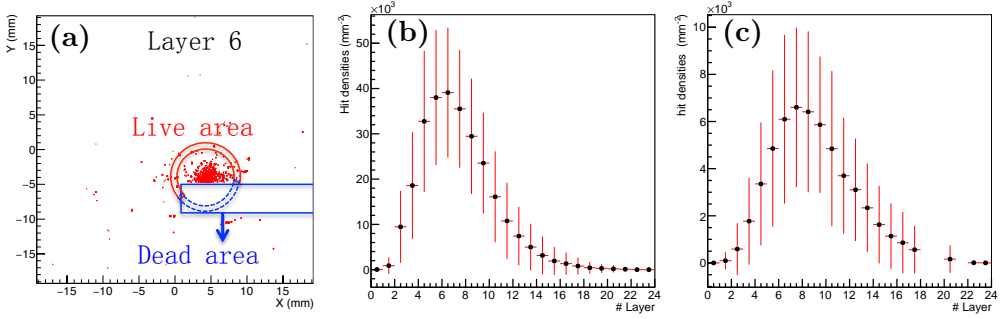


**Figure 4.12:** (a): Illustration of correction in case1. Hit densities in quadrant 0 as a function of depth (#layer) for 50 GeV positrons, at a distance  $r = 0.2$  mm (b),  $r = 2$  mm (c) from the shower center.

The choice of correction procedures for dead area only depends on the number of live pixels in a ring. The total number of hits for each electromagnetic shower is equal to the sum of the number of hits of all layers. The number of hits in each layer is calculated with Eq. 4.17 with a certain range  $R$ . In principle, different values of  $R$  can be used in these calculations.

# Chapter 5

## Simulation

The detector simulation software uses the TVirtualMC interface, which interfaces with the Geant3 [33] and Geant4 [34] software for particle transport and shower simulations. The simulation results presented in the following chapters are based on Geant4, unless explicitly specified otherwise. In order to make a valid comparison of simulation with experiment, a detailed detector description has been implemented, including the tungsten converter, filler plates, the silicon sensors, and the printed circuit boards on which sensors are mounted. For each event, noise is generated by a random generator which produces an average noise level of  $10^{-5}$  for live pixels. A charge diffusion model is used to distribute the deposited charge over neighbouring pixels. In the last section, the behavior of some observables in the simulation is studied, using the analysis algorithms that are applied to data.

### 5.1 Description of General Simulation

In the simulated geometry, the sensors are placed at the locations and orientations as determined by the alignment procedure (see Sec. 4.2). Dead sensors and channels are marked in the simulation, which take up 16.7 % of the total pixels. Simulation results with these pixels excluded are referred to as ‘real detector’, while for ‘ideal detector’ simulations, all pixels are included. Both versions have been studied here to understand the effect of the dead pixels. The external scintillators are also included in the simulated detector. Sensors with different properties, e.g. different thickness of the epitaxial layer and resistivity, are used in the prototype. To first order, this should mainly result in different sensitivity. We perform a calibration to correct the sensors to the same apparent signal height. The remaining possible differences between the different sensor

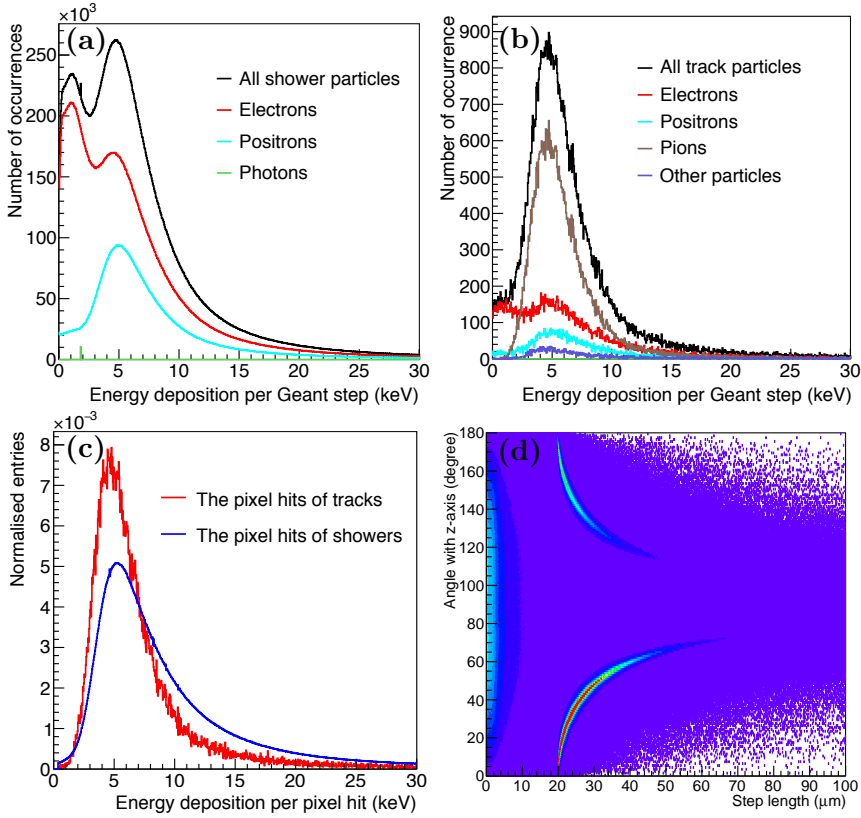


**Figure 5.1:** The spectrum of energy deposition induced by 100 GeV positrons (a) and by 100 GeV pion tracks (b). (c): Comparison of the deposited energy spectrum of the reconstructed pixel hits for showers and pion tracks. (d): Geant step length and angle of shower particles for 100 GeV positron events.

types are expected to be small, so we have implemented only one sensor type with a epitaxial layer thickness of 20  $\mu\text{m}$ .

In the simulations, we assume that there is no spread of the given beam energies. For the studies in this chapter, we will make use of 100 GeV pions or positrons. For later studies, a number of different beam energies have been simulated as indicated. The physics list ‘emStandard’ is employed for positrons and ‘FTFP\_BERT\_HP’ for pions. All the primary particles start at 5 m away from the first layer. The primary particle positions are uniformly distributed in the range of  $-10 \text{ mm} < x, y < 10 \text{ mm}$ . Only one primary particle per event is generated. The beam has a small inclination angle of  $\theta = 0.4^\circ$  with the  $z$  axis for the measurements at the SPS.

The information of Geant steps in the sensitive volumes is recorded, which includes energy deposition, step length, position, time and so on. In Fig. 5.1, panels a and b show the spectrum of energy deposition in Geant steps for positron showers and pion tracks. A pion event can be a track or a hadronic shower. Pion tracks are selected by requiring less than 1000 hits (table 4.1). Each Geant step in sensitive volumes is saved as a Geant hit. A pixel is counted as a ‘pixel hit’ when the energy collected by this pixel is larger than a threshold. This process is called hit reconstruction. A group of pixel hits induced by one event is called a frame. The distribution of deposited energy per reconstructed pixel hit is shown in Fig. 5.1 (c). The comparison of two distributions demonstrates that shower particles do not behave in the same way as tracks. The average energy deposition in each pixel hit from a shower is larger than from a track since shower particles can have a non-perpendicular angle with the sensor surface, but primary pion tracks always go perpendicularly through the detector and there are fewer secondary particles. Fig. 5.1 (d) shows the distribution of shower particle angles as a function of Geant step length. The step length is  $\frac{20}{\cos\theta} \mu\text{m}$  when a particle goes through the epitaxial layer. The curved bands in panel (d) follow this relation. If a shower particle does not go through the epitaxial layer in one step there is no connection between the step length and shower particle angle - one observes a broad distribution. The energy deposition of all the steps in individual pixels is summed and converted into pixel hits by setting a threshold.

Geant does not generate charge diffusion, so when Geant hits are converted directly into pixel hits, the average cluster size is 1 and the total number of hits for showers is much smaller than observed the experimental data. Results from a simulation with the ideal detector and no charge diffusion are shown in Fig. 5.2 (a) – the distribution of the total energy deposited in the active volumes – sensors for 100 GeV positrons. After digitisation – determining which pixels are pixel hits, the distribution of the total number of pixels hits is shown in panel (b) and the total response as a function of shower position is shown in panel (c).

Interestingly, the distribution of the total number of hits, i.e. the response for digital sampling, appears to be narrower than the distribution of the deposited energy, which corresponds to analog sampling. This is confirmed by Gaussian fits to the peaks, which are included in the figure. The relative width is 5.9% for the analog case and 4.6% for the digital case. The distribution of the total number of hits (panel b) is not fully described by a Gaussian distribution, there are tails both to the left and the right side. The tail on the left side of the peak indicates a low response. This can be due to leakage when showers are located far away from the detector center. In addition for our calorimeter, some of the

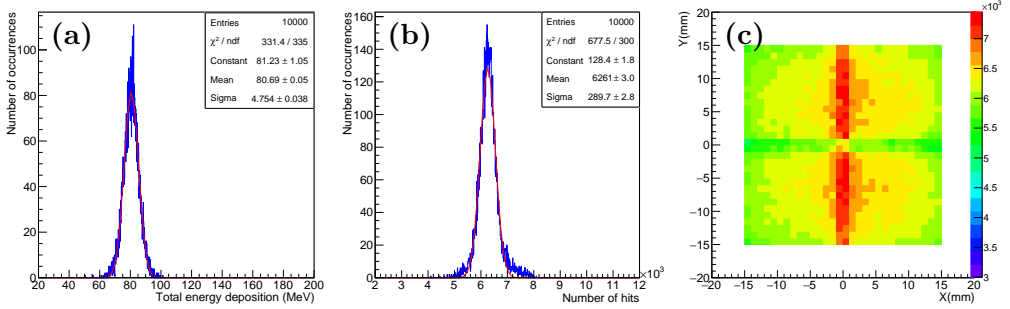


**Figure 5.2:** Simulations for the ideal detector and without charge diffusion. (a): Distribution of the total deposited energy for 100 GeV positrons with Gaussian fit. (b): Distribution of total number of pixel hits with Gaussian fit. (c): The total hit response as a function of shower position.

hits are not counted when showers are located in the gap regions. The right tail is caused by showers which are located in the overlap regions. These can be confirmed from panel (c). To achieve a good performance, we use a correction which is based on the hit density for the effects of the overlap and gap regions as well as partially contained showers, as explained in Sec. 4.6.6.

The total detector response after correction is shown in Fig. 5.3 (a). This improves the relative energy resolution to 2.9% for 100 GeV positrons. Looking into the response layer by layer, we find for early layers, e.g layer 5 (see panel b), a smaller response for showers that are located in the middle of the detector in the  $x$  direction, while for the later layers, such as layer 15, shown in panel (c), the number of hits is larger when showers are located in the same region. That is because of the gaps between the filler plates in the middle of the detector in the  $x$  direction (see the geometry description in Sec. 2.3). The radiation depth per layer in the filler gap region is less than in other regions, so the shower develops later.

The average cluster size (i.e. number of hits per cluster) in experimental data is  $\sim 3.5$  for pion tracks and  $\sim 4$  for shower particles, while it is 1 in both cases in the simulations without charge diffusion. An additional charge diffusion model is added to the Geant 4 simulation to simulate a realistic detector response for both tracks and showers. The charge diffusion model distributes the charge generated in each Geant step [34] over neighbouring pixels. For more details on the charge diffusion model, see Sec. 5.3.



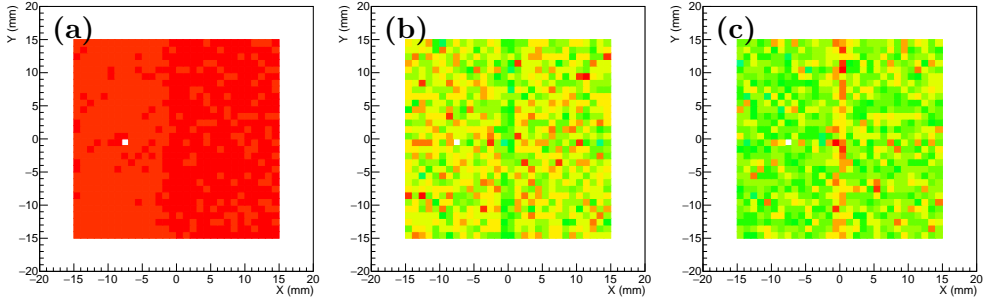


**Figure 5.3:** The number of pixel hits after correction for gap and overlap regions as a function of the shower position after correction for ideal detector for all the layers (a), for layer 5 (b) and layer 15 (c). The white square represents an empty bin, i.e. no beam particle.

## 5.2 Noise

The noise measurements in pedestal runs show that the noise is uniformly distributed in each sensor. We use a Poisson distribution to generate the number of noise hits

$$N_{noise} = \text{Poisson}(\overline{N_{noise}}), \quad (5.1)$$

where  $\overline{N_{noise}}$  is the mean number of noise hits per sensor.  $N_{noise}$  noise hits are randomly distributed over each sensor. This is much faster than simulating the noise of each pixel. The mean number of noise hits of  $N_{sensor}$  sensors will be  $N_{sensor} \times \overline{N_{noise}}$ , it can be described by a Gaussian distribution when  $N_{sensor}$  is large. Fig. 5.4 shows the distribution of the number of noise hits for 76 sensors which is equivalent to all working pixels, excluding the 4 sensors with a higher noise level of  $10^{-4}$  in layer 0. A good agreement between experiment and simulation is found for a Poisson distribution using a mean of  $\overline{N_{noise}} = 3.55$ . For the total detector, this corresponds to a mean value of the noise of 271 hits which is equal to the average response for 1.06 GeV electrons and has a standard deviation of 17.1. The contribution of the ‘noise term’ to the energy resolution is  $6.3\%/E$ , which is equivalent to fluctuations in units of energy of  $\approx 60$  MeV.

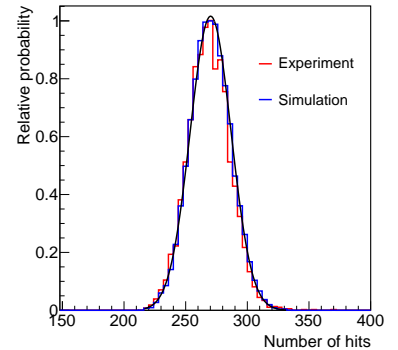


**Figure 5.4:** Distribution of the number of noise hits in simulation in blue and in data in red line with Gaussian fit (black line).

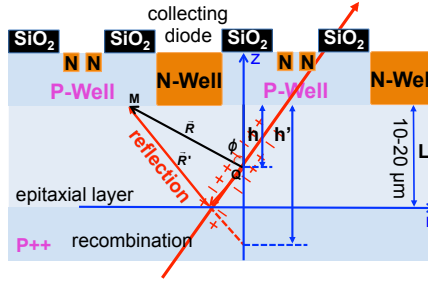


**Figure 5.5:** Illustration of the parameters used in the diffusion model calculation.

### 5.3 Charge Diffusion Model

When a particle crosses the epitaxial layer, electron–hole pairs will be generated along the particle’s trajectory. Since there is no electric field in the p-epitaxial layer, electrons reach the collecting diode through thermal diffusion. Charge recombination can take place during this thermal diffusion process. The charges generated in the highly doped substrate are lost because of the fast recombination of electron-hole pairs.

The charges generated in the epitaxial layer diffuse thermally and isotropically. In the model, recombination is characterised by an attenuation length  $\lambda$ . The charge moving towards the substrate will be reflected by the potential barrier. The charges collected are the sum of the charges that reach the collection diode directly and after reflection. Because of the recombination of carriers, part of ionizing charges can not be collected by the diode. This process is distance dependent.

The charge diffusion model [35] consists of isotropic diffusion and attenuation. When a track penetrates the epitaxial layer, free charge (electron-hole pairs) is generated at the point  $Q$ . The fraction of the produced charges that is collected at point  $M$  is  $(d\Omega/4\pi) \cdot p$ , where  $p$  is the probability. The charge collection probability density at horizontal distance  $r$  from the track and polar angle  $\phi$  in the detector plane, can be expressed in terms of the thickness  $L$  of the epitaxial layer and the depth  $h$  in the epitaxial layer:

$$\rho(\vec{R}) = \rho(r, \phi) = \frac{d\Omega}{4\pi} \cdot \exp\left(-\frac{|R|}{\lambda}\right) = \frac{1}{4\pi L} \frac{hr}{(h^2 + r^2)^{\frac{3}{2}}} \exp\left(-\frac{\sqrt{h^2 + r^2}}{\lambda}\right) dr d\phi \quad (5.2)$$

where the first term  $d\Omega/4\pi = \sin\theta d\theta d\phi/4\pi$  describes isotropic diffusion and the second term  $\exp(-R/\lambda)$  describes attenuation due to recombination with

constant attenuation length  $\lambda$ .

Apart from the charges directly reaching point  $M$ , the collection probability density at point  $M$  includes the contribution after reflection by the P++ substrate as well, where  $h' = 2L - h$ . Fig. 5.6 (b) shows the probabilities as a function of horizontal distance  $r$  at given  $\lambda$  for 3 values of  $h$ . The probability of directly reaching point  $M$  is higher than after reflection due to the longer path length that the reflected charges have to travel and the larger solid angle. The closer a charge is to  $M$ , the higher the probability of being collected.

To calculate the total charge collected by one pixel, we divide each Geant step into  $N$  substeps along the  $z$  direction. Each substep has a length of  $1 \mu\text{m}$  so that the number of substeps depends on the step length. The angle of a Geant step with the sensor surface is automatically taken into account. For each substep, the electronics layer is divided into a group of squares of  $1 \mu\text{m} \times 1 \mu\text{m}$  so that for a charge generated at a given  $h$ , the probability of being collected by one pixel can be quickly obtained by summing the probability for  $30 \times 30$  small squares. We only calculate the probability for the squares where the horizontal distance of the square to substep  $r < 120 \mu\text{m}$ .

It is assumed that each particle uniformly releases energy and generates charge along the particle direction in each step. The number of charges generated in each substep is  $(n_0/N)$ , where  $n_0$  is the total number of charges generated in one step which includes  $N$  substeps. The amount of charge collected by one pixel will be the sum of the collected charge released in each substep  $h$

$$\sum_{h=0}^L (n_0/N) \times \sum_{i=s}^{s+30 \times 30} p_h(r_i) \quad (5.3)$$

where  $p_h(r_i)$  is the probability of being collected by square  $i$  in position  $M$ , with horizontal distance  $r_i$  from the point where the charge is produced for given  $h$ . The calculation of  $p_h(r_i)$  follows. For this we essentially have to discretize Eq. 5.2.

According to Eq. 5.2, the probability of charge collection in each square will be the solid angle covered multiplied by  $\exp(-R/\lambda)$ . The solid angle can be given as  $\Delta\Omega = \int \sin\theta d\theta d\phi = (\cos\theta - \cos(\theta + d\theta))d\phi$ . As we are using a discretized version of the calculation,  $R$  is the distance between  $Q$  and  $M$ , where  $M$  is now located in the center of a small square. Note that this is different from [35] in which the distance  $R$  is the center of pixel to a vertical substep. In current simplified calculation, assuming  $dr = 1 \mu\text{m}$ , so  $\cos\theta = h/\sqrt{r^2 + h^2}$  and  $\cos(\theta + d\theta) = h/\sqrt{(r+1)^2 + h^2}$ . The  $d\phi$  is calculated according to the proportion of area one square takes in its ring at horizontal distance  $r$ ,

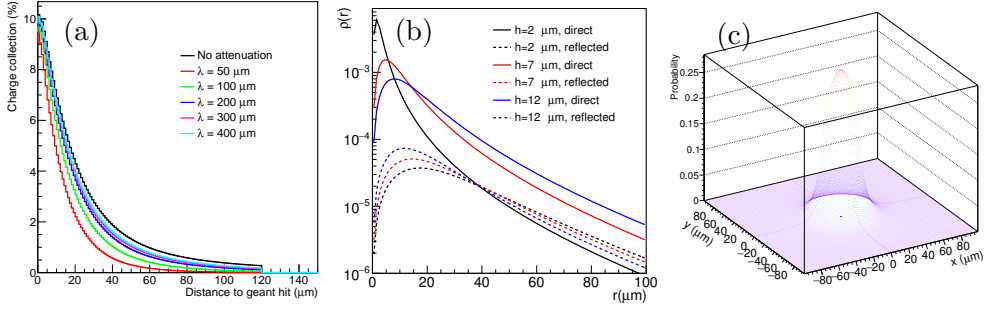


**Figure 5.6:** (a): Collecting probability of a small square as a function of horizontal distance  $r$  to the point where the charge is produced. (b): Collection probability for charges that reach the surface directly and after reflection. (c): Probability map of charge collecting for one pixel.

so  $d\phi = \frac{1}{2\pi r + 1}$ . The collecting probability of one square is

$$\begin{aligned}
 p_h(r_i) &= \Delta\Omega \cdot \exp\left(-\frac{|R|}{\lambda}\right) \\
 &= \left(\frac{h}{\sqrt{r^2 + h^2}} - \frac{h}{\sqrt{(r+1)^2 + h^2}}\right) \cdot \frac{1}{2\pi r + 1} \cdot \exp\left(-\frac{r^2 + h^2}{\lambda}\right)
 \end{aligned} \tag{5.4}$$

For reflected charge, the  $r$  and  $h$  will be  $r'$  and  $h'$  respectively. Fig. 5.6 (a) shows collecting probability of one square as a function of the horizontal distance between the center of the small square and the point  $Q$  for different attenuation length  $\lambda$ . Fig. 5.6 (c) shows an example of the total fraction for one pixel as a function of relative pixel position to the point where the charge is deposited in substep for  $h = 7\mu\text{m}$ .

The number of pixel hits depends on the charged particle direction, the energy deposition, thickness of epi-layer, and the detection threshold in this model.

## 5.4 Determining The Model Parameters

The cluster size in the simulation is determined by three quantities: the thickness of the epitaxial layer, the attenuation length  $\lambda$  in the charge diffusion model and the detection threshold. The thickness of the epitaxial layer  $L$  is known from the fabrication process, leaving only two free parameters. The values of those parameters are determined by comparing the cluster size distribution from simulations with the measured distributions in the experiment. The

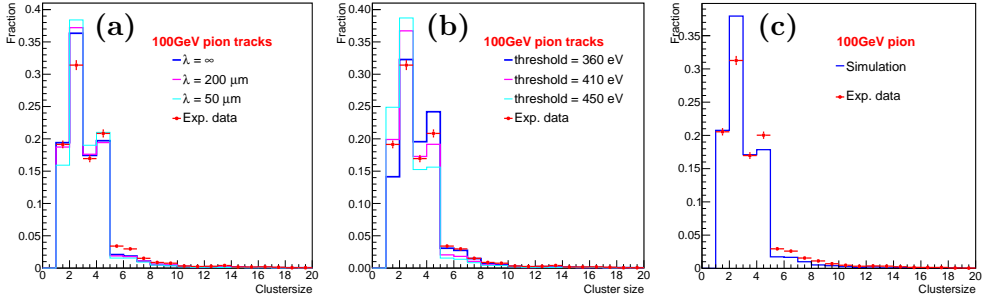


**Figure 5.7:** Study of charge diffusion parameters -  $\lambda$  and threshold - through comparison of the distribution of cluster size for sensor 7 between data and simulation. (a): Varying threshold for each  $\lambda$  to keep the average cluster size equal to 3. (b): Changing thresholds for  $\lambda = 200 \mu\text{m}$ . (c): Threshold is 450 eV and  $\lambda = \infty$  for the final choice of parameters.

threshold is verified and refined by comparing the distribution of the number of hits for electromagnetic showers of various energies.

To make a valid comparison, the experimental cluster size distribution is extracted from sensor 7 whose calibration factor is  $\sim 1$  (see Sec.4.6.3) and the thickness of the epitaxial layer is  $20 \mu\text{m}$ . Fig. 5.7 (a) shows the comparison between data and simulation with different attenuation length  $\lambda$  while the thresholds are tuned to keep the average cluster size the same. The shape of the cluster size distribution is closest to the data for large values of  $\lambda$ . Fig. 5.7 (b) shows the comparison with different thresholds when  $\lambda = 200 \mu\text{m}$ .

Currently,  $\lambda = \infty$  and a threshold of 450 eV are used for a sensor thickness of  $20 \mu\text{m}$ . For these values of the parameters, also the shower response shows a good agreement between experimental data and simulation. Since  $\lambda = \infty$ , this model can be further simplified such that only the isotropic charge diffusion is responsible for the distribution of the generated charge. The attenuation term can be neglected.

## 5.5 Simulation Results

Realistic simulation results are obtained after adding charge diffusion and applying the mean hit density method. Normally, the properties of a detector are obtained event by event. For the longitudinal profile, the hit density based analysis will be presented and compared with a standard analysis which counts hits without using corrections for non-uniformities.

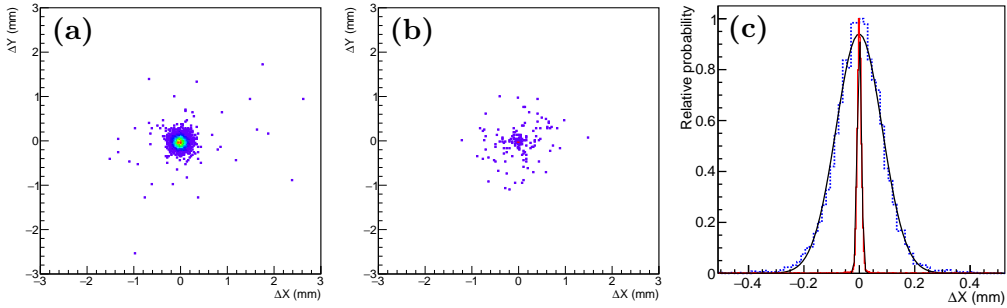


**Figure 5.8:** The approximate and the final shower position resolution. The distribution of the distance between the real position and the approximate (a) and the final position (b) in  $x$  and  $y$ . Their projection onto the  $x$  coordinate in blue (approximate) and red (final) respectively, with Gaussian fits in black (c).

### 5.5.1 Shower position determination

As described in Sec. 4.3, the ‘approximate shower position’ is determined by the hits in layer 3 and 4, and the ‘final shower position’ is determined by the position of the cluster in layer 0, which is closest to the approximate shower position. In simulation, we exactly know the ‘real shower position’, i.e. the position of every incoming particle and we can use this information to determine the resolution of the approximate and final shower position. Fig. 5.8 (a and b) show the distribution of the difference between the real position and the approximate and final shower position. The corresponding projections are shown in panel (c), the widths of them are the shower position resolution. The approximate and the final shower position resolution are  $83 \mu\text{m}$  and  $7 \mu\text{m}$  respectively for 100 GeV positrons. The final shower position is so precise that it will be used as the shower position without further corrections in the analysis.

### 5.5.2 Effects of charge diffusion

Fig. 5.9 (a) shows the distribution of the total number of pixel hits within a cylinder of  $r = 22 \text{ mm}$  ( $\sim 2 R_M$ ), with and without charge diffusion. The results show that the energy resolution is not changed (2.9%) when charge diffusion is applied, but the total number of hits increases by a factor of  $\sim 4$ , called ‘gain factor’. The value of the gain factor induced by the charge diffusion depends on the deposited energy, the angle of a particle relative to the sensor surface and the particle density. Fig. 5.9 (b) shows the longitudinal profiles with and without charge diffusion in the upper panel and their ratio in the lower panel. For early layers, the gain factor is slightly smaller than 4. As a consequence, a shift of

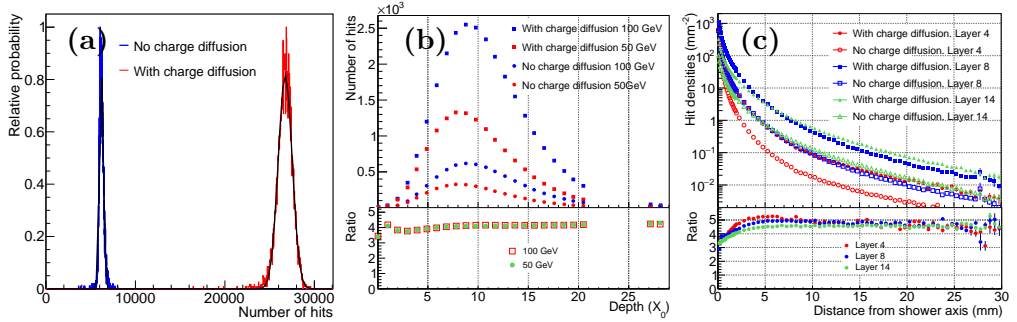


**Figure 5.9:** Study of the effects of charge diffusion with the same threshold for no charge diffusion. (a): Distribution of the total number of hits after correction for 100 GeV positrons, with (red histogram) and without (blue histogram) charge diffusion. The black curves show a Gaussian fit to the histograms. (b): Comparison of longitudinal profiles with and without charge diffusion for 100 GeV and 50 GeV positrons. The ratio of the results with and without charge diffusion is shown in the lower panel. (c): Comparison of the lateral profiles with and without charge diffusion for 100 GeV positron showers at selected layers. The lower panel shows the ratio up to the point where hit density with charge diffusion is smaller than twice the noise density.

$\sim 0.1 X_0$  of the shower maximum position in depth is induced. Similar details are observed in the lateral distributions, as shown in Fig. 5.9 (c). The effective gain factor depends on the local particle density and therefore is smaller at small distances from the shower center and increases at larger distances, then stays constant. The total effective gain factor is determined by an interplay of charge sharing, energy deposition, and the angle of the particles relative to the sensor, which all enter in the charge diffusion model. Very close to the shower core, the gain factor is smaller than the average due to saturation. The maximum at intermediate distances may be due to the other possible effect of charge sharing, namely the possibility to get additional pixels above the threshold.

### 5.5.3 Limitation of interpolation for dead areas

The distributions of the total number of hits for the ideal and real detector are shown in Fig. 5.10 (a). The mean numbers of hits are almost identical for the two cases, but the width of the distribution (indicated by the error bars) for real detector is larger than for the ideal detector. When the shower center falls inside a dead area, the response is calculated by interpolating the hit densities from the neighboring layers. It can be seen from the longitudinal profiles in Fig. 5.10 (b), that the interpolation can lead to a biased estimation of the number of hits

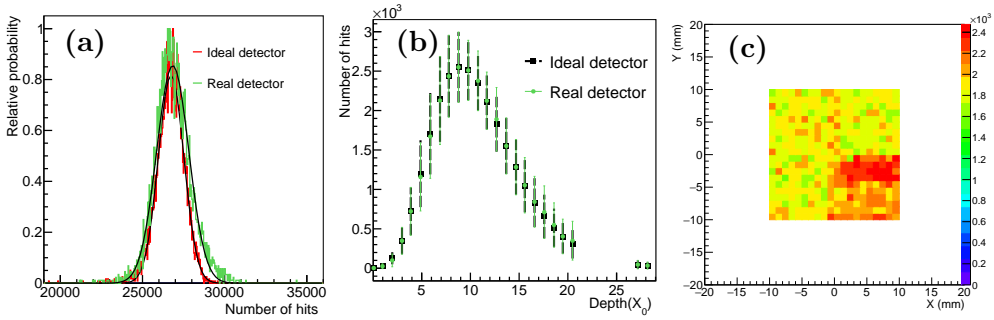


**Figure 5.10:** (a): Distribution of the total number of hits for the ideal (red) and real (green) detector at 100 GeV positrons. (b): The longitudinal profiles for the ideal and real detector in the upper panel, the ratio of the number of hits for the ideal to real detector in the bottom panel. The error bars represent the standard deviation of the number of hits in each layer. (c): Response as a function of shower position after correction for layer 13.

and a broader distribution. Looking into one of the layers, we do not correctly interpolate the dead area even in simulation when showers are located in dead areas (*case 2*). As Fig. 5.10 (c) shows, the number of hits in this dead area of  $x > 0$  and  $y < 0$  estimated by neighbouring layers is larger than the number of hits in other area. This leads to a difference between the ideal detector and the real detector.

#### 5.5.4 Calculation of the average response

Generally, the number of hits of the detector is determined from the calibrated hit density in a given event. The average response is calculated as the mean of the total number of hits for each layer as well as for the full detector. We call this method the ‘standard method’. The real detector has a significant fraction of dead area due to bad sensors. Using the rotational symmetry of the shower to correct for dead areas, one can measure radial profiles using information from only live areas as explained in Sec. 4.5.

From the same information one can also obtain the average lateral hit densities, and the mean number of hits in each layer can be calculated by integration. The average response of the detector is the sum of the mean of all layers. We call this alternative method the ‘mean density method’.

The standard method can be used to study shower-to-shower fluctuations, but it is more strongly affected by the dead areas, while the mean density method minimizes the effects from dead areas but cannot be used to measure fluctuations. The left panel of Fig. 5.11 shows three longitudinal profiles using



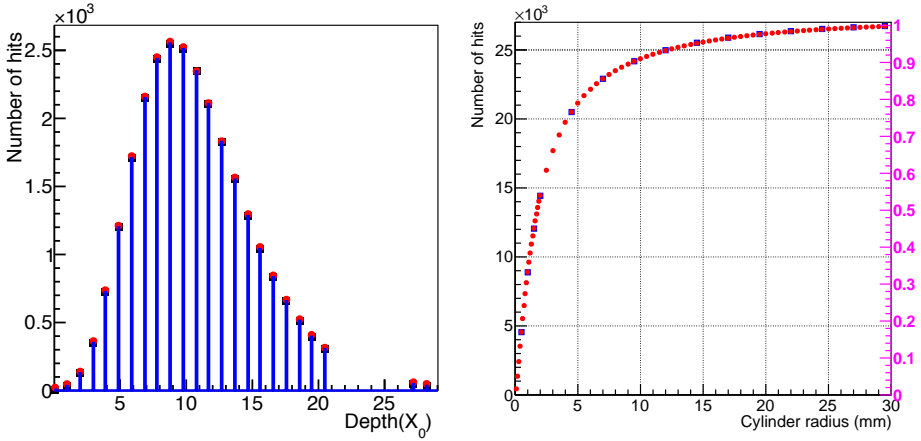


**Figure 5.11:** Left: the three longitudinal profiles for 100 GeV using the standard method for the ideal detector (black), and the mean density method for the ideal (red) and real detector (blue). Right: the total average number of hits for the ideal detector as a function of distance from the shower axis, which is obtained using the standard method and the mean density method. The right axis shows the fraction of the number of hits which is normalized by the number of hits for a cylinder radius of  $R = 30$  mm.

the mean density method for the ideal detector and real detector, and the standard method for the ideal detector. The similarity of the longitudinal profiles indicates that the mean density method provides an accurate correction for the dead areas.

Similarly, using Eq. 4.17, the total number of hits in a cylinder with radius  $R$  can be obtained. This number can also be obtained from the number of hits shower by shower. Fig. 5.11 right shows the number of hits as a function of cylinder radius using the two methods. The high consistency allows using the mean density method to determine some of the detector observables as e.g. longitudinal profile and Molière radius.

### 5.5.5 Fitting the longitudinal profiles

Fig. 5.12 shows longitudinal profiles for 100 GeV and 5.4 GeV when charge diffusion is and is not implemented with the Gamma function (Eq. 1.10) fits. The ratio of the values of the fit curve and the measured number of hits are shown in the lower panels. It can be seen in the ratio figures that the Gamma function does not fit well for about the first 2-3 radiation lengths and the last two radiation lengths. The behaviour is independent on whether charge diffusion is used or not. Thus the shower maximum positions found from the Gamma fits

could be affected by the fitting range. PDG explains: “The gamma function distribution is very flat near the origin, while the EGS4 cascade (or a real cascade) increases more rapidly. As a result Eq. 1.10 fails badly for about the first two radiation lengths” [32], which is same as our observation. In the prototype, the disagreement for the last two layers, may be related to the small number of shower particles and the large relative importance of shower-to-shower fluctuations.

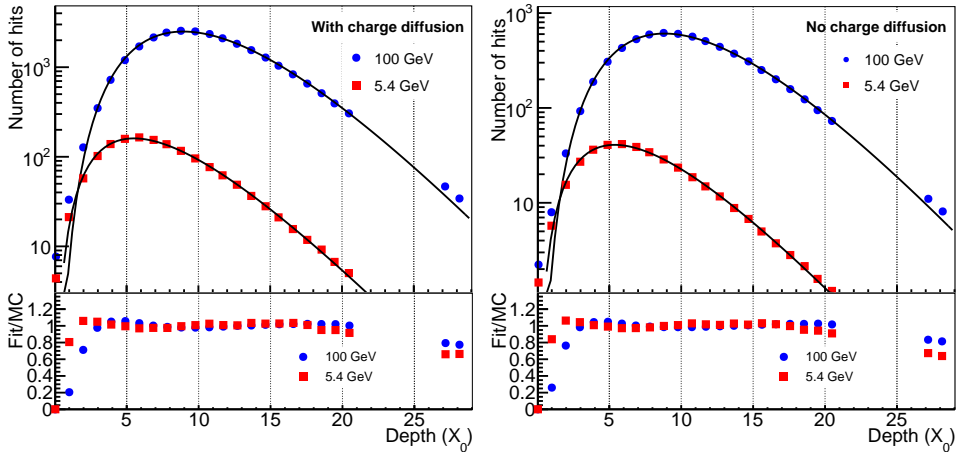


**Figure 5.12:** Gamma function fits to longitudinal profiles with (left panel) and without charge diffusion (right panel) for 100 GeV positron showers (blue dots) and for 5.4 GeV positron showers (red squares) where fitting range covers all depth in black curves. The lower panels show the ratio of values of the fit curves to the number of hits in the simulation.

### 5.5.6 Effects of calibration

In data analysis, the inter-layer calibration may change the longitudinal shower shape because this calibration is based on the fit of Gamma distribution. The previous section discusses that Gamma distribution is suited for the prototype. This section here discusses the effects of the calibration on the longitudinal profiles via applying the calibration in simulation data. This is done using the following steps:

- apply the calibration factor to the sensors. This step is to manually make the sensor sensitivity non-uniform. The modified number of hits in each sensor is changed by a factor of  $\frac{1}{c_i}$ ,  $c_i$  is calibration factor of sensor  $i$ .

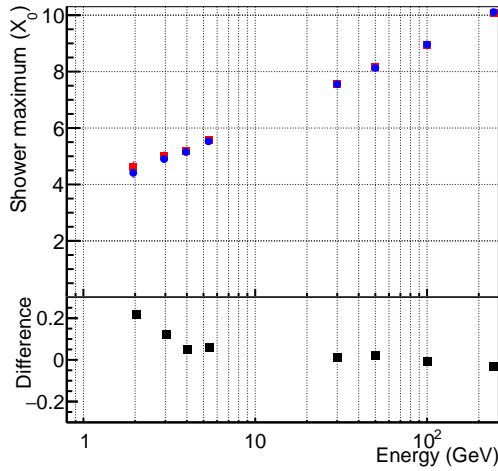


**Figure 5.13:** The position of the shower maximum as a function of energy for before (blue dots) and after (red dots) applying calibration to simulated data in the upper panel and their difference in the bottom panel.

- perform the same calibration procedures as for experimental data to the modified number of hits, and obtain the new calibration factors. Here we select 100 GeV to obtain the corresponding calibration factors.
- calculate the shower maximum from the fit of the Gamma distribution.

Fig. 5.13 shows the shower maximum position as a function of beam energy. A good agreement between before and after applying the calibration to simulated data is observed for high energies. A discrepancy appears for low energy – this may be due to the fact that the shower maximum is in the early layers for low energy and may thus be more strongly affected by a bad description of the shape by the Gamma distribution. The largest discrepancy is 0.22  $X_0$  for the lowest energy – 2 GeV.



# Chapter 6

## Results

The analysis of the experimental data is performed and then compared with simulation.

### 6.1 Introduction

The performance in beam tests presented below is always affected by the measurement conditions which include purity, position distribution, and energy spread of the beam. Furthermore, there are general properties relevant for any calorimeter, which influence the measurements, like

- detector size and corresponding sensitivity to leakage,
- the internal detector design, and
- the sensitivity and stability of active elements.

In the special case of our digital calorimeter prototype, one has to also consider

- the digitisation of energy deposition to pixel hits
- the particular properties of the CMOS sensors, and
- saturation and effects from charge sharing.

As many of these properties of a detector as possible have been implemented in GEANT simulations, so that one can reproduce the measurements and understand the limiting factors. While an ideal sampling calorimeter would consist of only fully sensitive sampling layers and homogeneous absorbers, our prototype contains, besides the absorber, also filler plates, empty space (air), glue and PCBs, all of which influence the measurements. These have all been implemented in a GEANT simulation. The properties of sensors include pixel size,

charge diffusion, pixel sensitivity and threshold, which all influence the process of digitisation. Saturation and charge sharing influence the number of pixel hits induced by individual particles. When clusters from individual shower particles overlap and therefore some pixels receive charge from different particles, two effects can occur

- **Saturation:** At higher particle density, a situation may occur where overlaps between different clusters become large and the number of observed pixels is smaller than expected.
- **Cluster tail overlap:** At lower density, the amount of charge for the individual shower particles is not sufficient to fire a pixel, but the combined charge can be above the threshold. As a consequence, the number of observed pixel hits is larger than expected.

The limited size of the prototype leads to significant shower leakage, in particular for high energy. Due to shower leakage and also dead areas, part of the shower is missing from the measurement, and this missing energy induces sizeable fluctuations in the number of hits.

The calibration homogenizes the sensor sensitivities. The hit density analysis corrects the number of hits for overlaps and dead areas to some extent, and can also correct partially for lateral leakage, but can not correct for fluctuations of hits in the dead areas.

### 6.1.1 Systematic uncertainties

Here we discuss the stability of detector response and the systematic uncertainties.

The stability of detector response to the beam is studied using 100 GeV data set (4000 events) which are divided into 8 parts. This stability refers to beam stability and response stability. 8 average numbers of the total hits and 8 shower max positions are extracted from the 8 sub-data sets (see Fig. 6.1). The response stability is indicated by the numerical width of 0.6% and  $0.03 X_0$ .

In Sec. 5.5.5, the Gamma distribution is proved to be suited to fit the longitudinal profile for range of 3-21  $X_0$ . The layer response depends on the calibration, saturation and so on. In Sec. 5.5.6, it is shown that the layer-by-layer calibration can induce a small bias in the longitudinal profile measurement at low energy, while the bias is negligible for high energy. Assuming that the Gamma distribution provides a good description of most of the layers we calculate the systematic

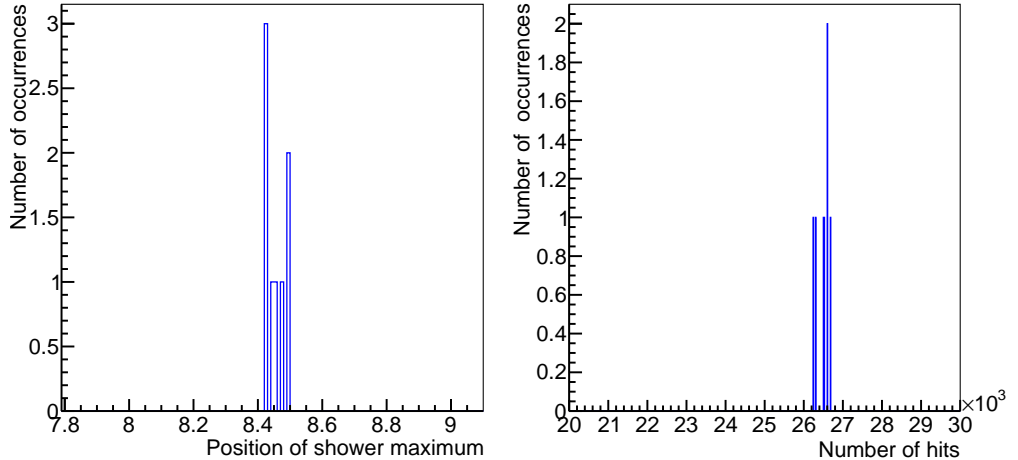


**Figure 6.1:** The distribution of mean of the number of hits (left) and the distribution of mean shower maximum position (right) for 100 GeV electromagnetic showers.

uncertainty of the number of hits using a formula similar to a study in [40]:

$$\delta E = \frac{\sqrt{\sum_{l=2}^{21} (M_l^{fit} - N_l(E))^2}}{\sum_{l=2}^{21} N_l(E)} \quad (6.1)$$

where the first and last two layers are not included.  $M_l^{fit}$  is the number of hits from Gamma fit to the longitudinal profile,  $N_l$  is the number of hits. The uncertainties for data and simulations are listed below.

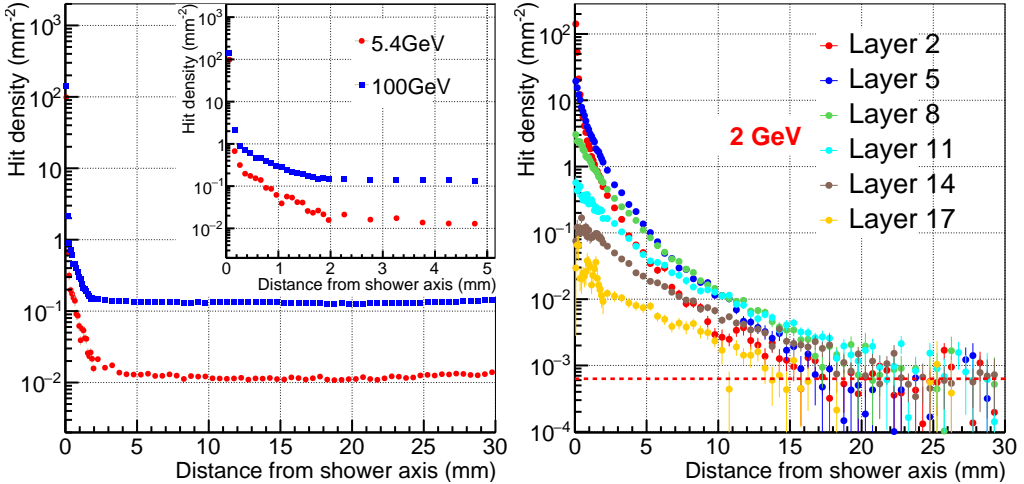
For simulation, the uncertainty is caused by the fit quality and detector properties which include digitalization, saturation and so on. Overall, the small uncertainty indicates that Gamma distribution can fit the longitudinal profiles well, and the detector response deviation is small. The uncertainty for 2 GeV is 4.0% – larger than others due to the fact that the shower maximum is close to the excluded layers 0 and 1. For data, the uncertainty also involves calibration. Here, the largest uncertainty appears for the energy far from the energy where the calibration factors were obtained – 5.4 GeV for DESY and 50 GeV for SPS. For most cases, this systematic uncertainty estimate is smaller than 2 % (see Table 6.1).

### 6.1.2 Lateral hit density profile

The FoCal prototype with its high granularity sensors allows to observe the shower development in detail, especially in a small shower core region where it

**Table 6.1:** Systematic uncertainty on average response (%).

Energy (GeV)	2	3	4	5.4	30	50	100	244
Data	4.7	3.6	1.0	1.9	3.1	1.8	0.7	1.2
Simulation	4.0	2.1	2.0	1.8	1.5	1.4	1.4	1.5

**Figure 6.2:** Lateral hit density profiles in layer 0 for 5.4 GeV and 100 GeV positrons (left), in given layers for 2 GeV (right). The red dash line indicates the noise fluctuations.

is important for two-shower separation at small distance. The lateral shower shape is studied by presenting the distribution of hit densities ( $\rho_l(r) = \frac{dN}{dS}$ ) as a function of the distance from the shower axis. Note that here we use the hit density per unit area  $S$  in two-dimensions ( $x$  and  $y$ ). In the literature, sometimes the one-dimensional density  $\frac{dN}{dr}$  is also used to characterise the lateral shower shape.

The average noise has been subtracted in Eq. 4.16 for all the layers except the first layer. The lateral profiles in the first layer (layer 0) for 5.4 and 100 GeV beam energy are displayed in Fig. 6.2 left. The data at the two different energies were taken with different threshold settings of the sensors in layer 0 to explore the effect of the threshold on the sensitivity. The clear difference in noise level between the two energies is a result of the threshold change.

The thresholds were tuned to obtain noise hit densities of 0.01/mm<sup>2</sup> and 0.1/mm<sup>2</sup> respectively. A sharp peak of  $\sim 100$  hits/mm<sup>2</sup>, corresponding to an average of  $\sim 3$  hits per event, appears for  $r < 0.1$  mm, which is similar to the response for MIPs (see Fig. 3.5). The standard deviation of this sharp peak is  $\sim 0.04$  mm indicating a very accurate shower center position determination.



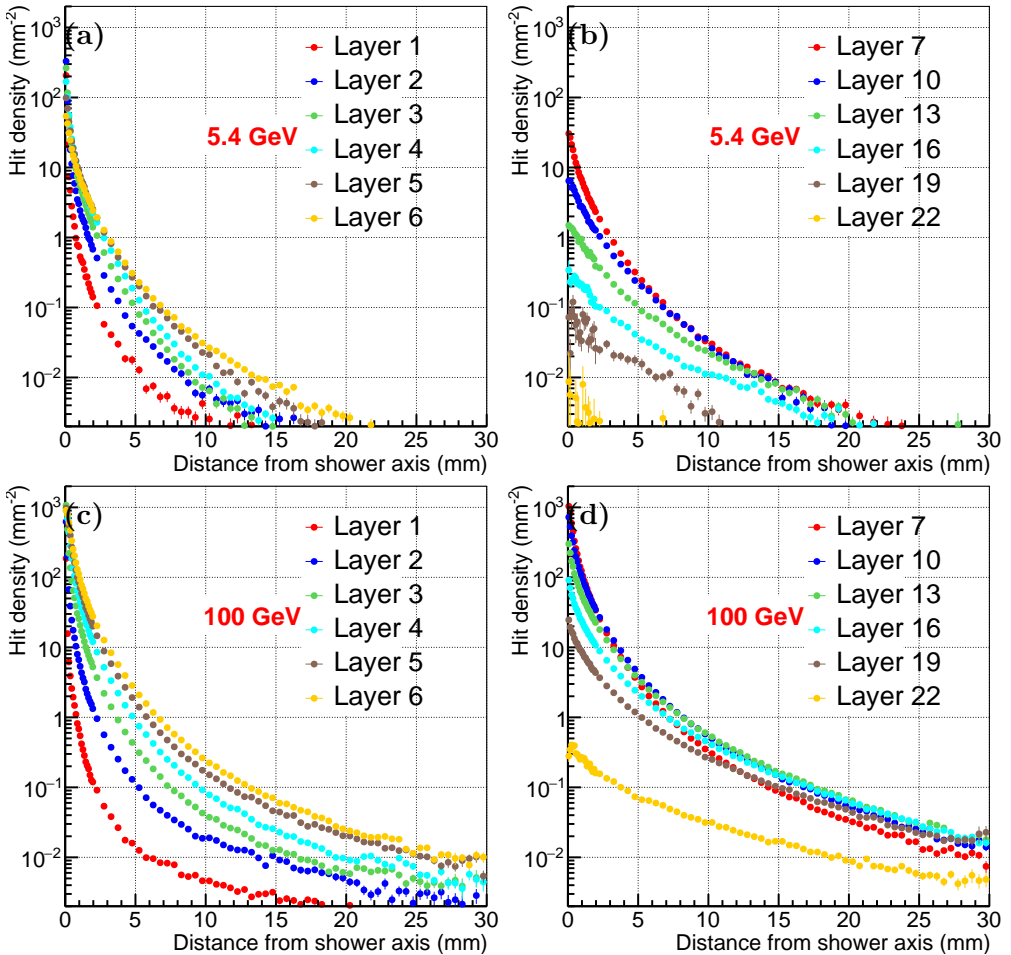


**Figure 6.3:** Lateral hit density profiles at different layers and energies - (a, b): at the given layers for 5.4 GeV positrons at DESY, (c, d): at the same given layers for 100 GeV positrons at SPS.

Beyond the sharp peak, the density does not drop abruptly, but there is a tail, which decreases gradually to the constant noise level. The two main contributions to this tail are early conversions and back scattering. A similar behaviour is found in the simulation of the detector response.

Due to the subtraction of the noise in Fig. 6.2 right, one expects the curves to level off to zero with fluctuations corresponding to the width of the noise distribution (Fig. 5.4). The noise fluctuation of  $10^{-2} \times 6.3\%$  is indicated with the red dashed line.

Typical calibrated lateral profiles are displayed in Fig. 6.3. With these, one can study the evolution of electromagnetic showers layer by layer. The steepness

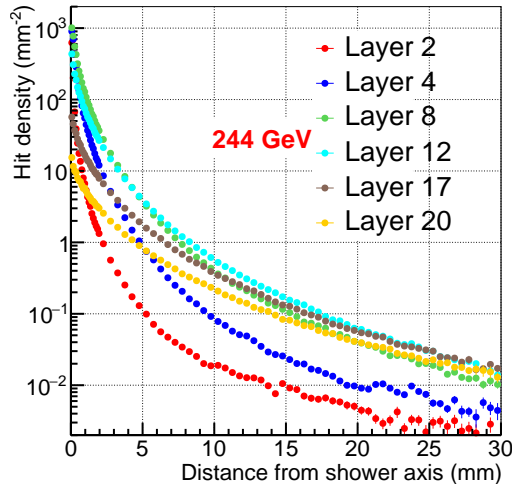


**Figure 6.4:** Lateral hit density profiles at selected layers for 244 GeV electrons at SPS.

of the hit density profiles decreases with increasing shower depth. For 5.4 GeV beam energy, the largest local hit density is reached in the region of  $r < 0.1$  mm in layer 2, while the largest total number of hits, which is often referred to as the ‘shower maximum’, is in layer 5. The total number of hits per layer increases up to layer 5 and decreases afterwards. The hit densities in the region of  $r < 0.1$  mm monotonically decrease, starting from layer 2 as also shown in Fig. 6.5.

The shower becomes broader as the shower develops and the lateral profile becomes relatively flat. Before the shower maximum is reached in layer 5, the hit densities increase with increasing depth in the most part of  $r > 0.2$  mm. After the shower maximum, the corresponding hit densities decrease with depth.

As an example of a higher beam energy, the lateral hit density profiles from 100 GeV positrons are also shown in Fig. 6.3 (c and d). The largest hit density still appears in the region of  $r < 0.1$  mm, but in layer 3, considerably earlier than the shower maximum in layer 9. The maximum density in layer 3 is  $\frac{1}{S_{pixel}} = 1111/\text{mm}^2$ , and the later layers have a similar density. The constant density is due to saturation: the signal in all pixels is above the threshold in this area. Before the shower maximum, the hit densities in the outer part of the shower also increase with increasing depth. After the shower maximum, the hit densities in shower core decrease with increasing shower depth, while at a larger distance from the shower axis, the hit densities do not show a strong dependence on shower depth and only start to decrease strongly in the last layers (layer 22 and 23).

We can also compare this to the distribution of hit densities for even higher energy, 244 GeV see Fig. 6.4. At this energy, the overall pattern is similar to that for 100 GeV beam energy, except that saturation near the shower center is only reached for layer 3 and then persists up to the shower maximum in layer 10.

Figure 6.5 shows the hit density as a function of shower depth at several selected distances  $r$  from the shower center. First, we can see that the maximum hit density moves deeper with increasing ring  $r$ . For higher energy, panel (b), the same qualitative behaviour is found. But the change of the density as a function of shower depth is slower than for lower energy.

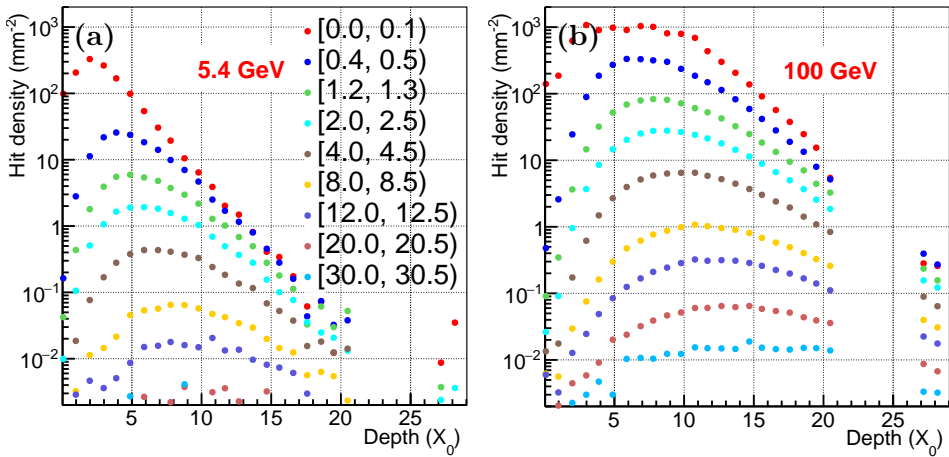


**Figure 6.5:** Longitudinal hit density profiles for different rings in mm from the shower axis for 5.4 GeV (a) and 100 GeV (b).

### 6.1.3 Fitting the lateral hit density profiles

To characterise the shower development in more detail, it is useful to find an analytic description of the shape. The lateral profiles as shown in Fig. 6.3 are strongly curved in the logarithmic representation - it is obvious that they cannot in general be described by a single exponential function only. As introduced in Sec. 1.4, the lateral development of electromagnetic showers has contributions from core and halo respectively. Earlier, a sum of two exponentials has been suggested to fit the lateral profiles [9],

$$f_1(r) = A_1 [p \cdot \exp(-r/\lambda_1) + (1 - p) \cdot \exp(-r/\lambda_2)] \quad (6.2)$$

but also that function does not provide a good fit. In this study, we have explored other functions.

The second function is the sum of an exponential and an exponential of the square root of the distance  $r$  to the shower axis, which was first suggested in [36]:

$$f_2(r) = A_1 \left[ p \cdot \exp(-\sqrt{r/\lambda_1}) + (1-p) \cdot \exp(-r/\lambda_2) \right] \quad (6.3)$$

The third function was proposed by Grindhammer [37]:

$$f_3(r) = A_1 \left[ p \cdot \frac{2R_1^2}{(r^2 + R_1^2)^2} + (1-p) \cdot \frac{2R_2^2}{(r^2 + R_2^2)^2} \right] \quad (6.4)$$

The last function is a modified power law, which was originally introduced in [38] to describe transverse momentum spectra in particle physics:

$$g(r) = p_0 \left( 1 + \frac{r}{p_1 \cdot p_2} \right)^{-p_1} \quad (6.5)$$

Fig. 6.6 (a and d) shows the lateral profile in layer 8 together with all the fit functions. The lower panel shows the relative deviation of the fit for each point i.e.  $d_l^i(r) = \frac{\rho_{fit}(r) - \langle \rho_l(r) \rangle}{\langle \rho_l(r) \rangle}$ , where  $\rho_{fit}(r)$  and  $\langle \rho_l(r) \rangle$  are the fitted and the measured hit density. The ratio is not drawn when the hit density reaches the noise level i.e.  $\langle \rho_l(r) \rangle < 0.01$ . For this layer, the best fit comes from the modified power law  $g(r)$ . In the main region ( $< R_M$ ), all the functions provide a good fit, but only  $g(r)$  keeps a good fit in the range of  $r > 15$  mm. Fig. 6.6 (c and f) compares the total number of hits per layer as obtained from a numerical integration of the profiles to the integrals of the fit functions. A good agreement is found, indicating that the deviations at large  $r$  do not affect the integral.

We use the RMS of the relative deviation

$$\sigma_l = \sqrt{\frac{\sum_{i=1}^N d_l^i(r)^2}{N}} \quad (6.6)$$

to characterise the quality of the fits in each layer  $l$ . Fig. 6.6 (b and e) shows the fitting quality of all the functions we tried. The best fit function is  $g(r)$ , then  $f_2(r)$ . There is a trend that the fit quality becomes better with increasing depth. The profiles in the first and the last two layers are hard to fit. The fits of  $f_3(r)$  for layers 11 and 20 do not look reasonable. Overall, the fits of  $g(r)$ ,  $f_2(r)$  and  $f_3(3)$  for 100 GeV are better than for 50 GeV.

For the two most successful fit functions we look in some more detail at the

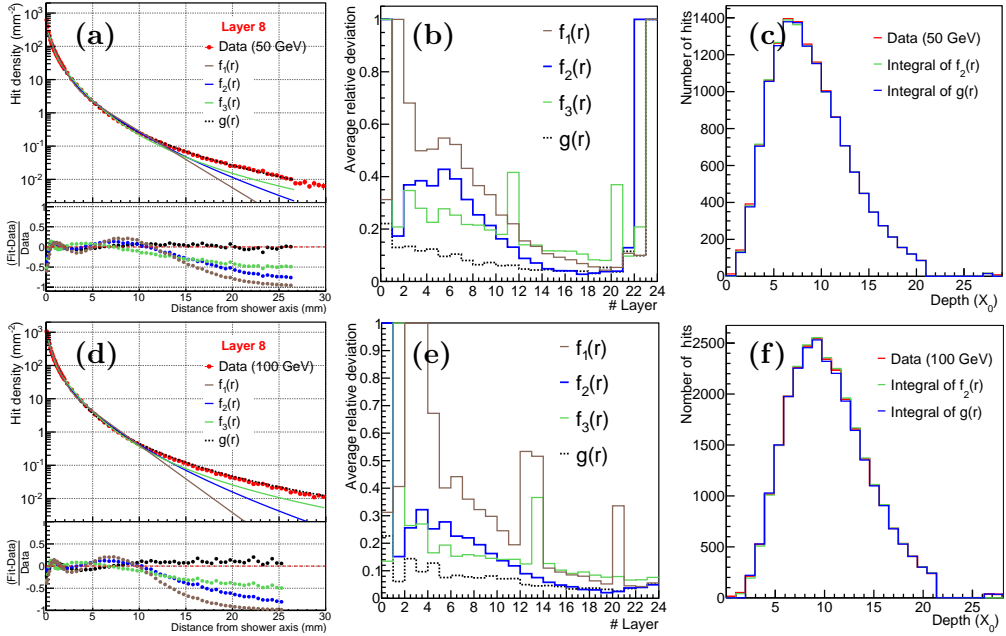


**Figure 6.6:** The quality of fitting lateral profile with functions. (a): Comparison between the lateral hit density profiles and 4 fits in layer 8 for 50 GeV positrons. The lower panel shows the relative deviation of the fits, corresponding curve in same color dots. (b): The RMS of relative deviation for all the layers,  $d_i^j(r) = 1$  represents a failed fit. (c): The number of hits obtained by integrating the hit densities for each layer (red line) and integrating the  $f_2(r)$  fit value in green,  $g(r)$  fit value in blue. (d,e,f): Similar distributions for 100 GeV positrons.

fit parameters. The parameter values of  $f_2(r)$  are displayed in Fig. 6.7, and the ones for  $g(r)$  in Fig. 6.8. The parameter values for both fits are also given in Table 8.2.

The first parameter of the function  $f_2(r)$ ,  $A_1$ , is the main amplitude parameter of each layer and is crucial for the description of the longitudinal profile. The width parameters  $\lambda_1$  and  $\lambda_2$  gradually increase with depth, indicating a broadening of the shower with increasing depth. Here  $\lambda_2$  represents the narrower part of the shower, the core.  $C_{12}$  is the relative weight of the second term. The evolution of this parameter indicates that the hit densities for early layers can be described mainly by the second component of Eq. 6.4, the core part of the distribution, while from layer 7 on, the first component becomes more important.

The function  $g(r)$  describes the distributions well with just 3 parameters.

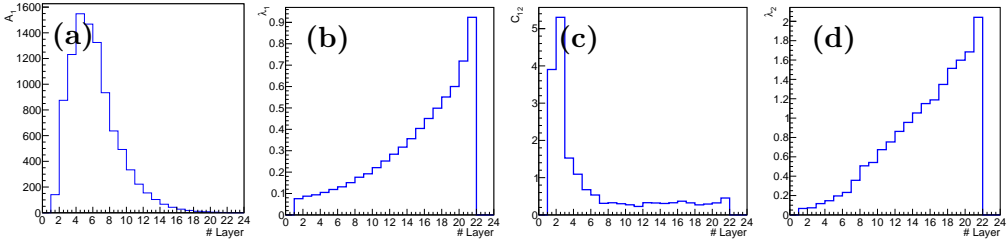


**Figure 6.7:** Parameters of fitting function  $f_2(r)$  for 50 GeV positrons,  $A_1$  (a),  $\lambda_1$  (b),  $C_{12}$  (c),  $\lambda_2$  (d).

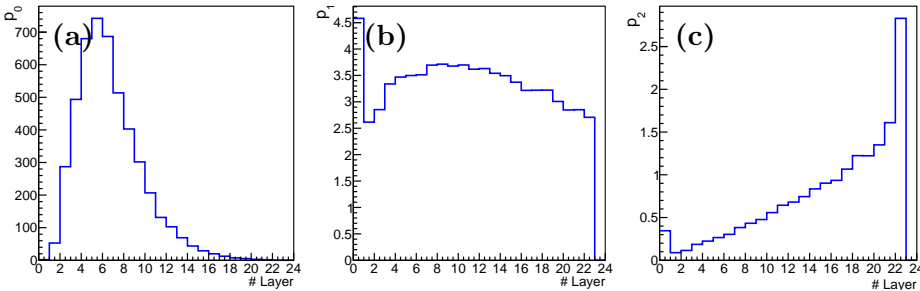


**Figure 6.8:** Parameters of fitting function  $g(r)$  for 50 GeV positrons,  $p_0$  (a),  $p_1$  (b) and  $p_2$  (c).

As can be seen in Fig. 6.8 on the left,  $p_0$  again has the role of an amplitude, its behaviour is qualitatively similar to  $A_1$  from function  $f_2(r)$ . The other two parameters have a slightly different interpretation.  $p_2$  determines the negative inverse logarithmic slope at  $r = 0$ , so it determines how narrow the inner core of the distribution is. This part of the distribution gets less steep with depth, indicated by an increasing slope  $p_2$ .  $p_1$  determines the curvature, or change in slope, of the function in a log plot. In the limit  $p_1 \rightarrow \infty$  the function evolves into a pure exponential. The value of this parameter shows no strong variations as a function of depth, except for layer 0, which anyhow has a special role in our prototype.

As a next step one might attempt to obtain a fully three-dimensional analytical description of the average shower shape. One possibility might be to use the good parameterisation for the lateral shape established here, and parameterise the behaviour of the fit parameters as a function of depth. The continuous behaviour of the fit parameters gives reasonable confidence that this should be possible, in particular for the early layers 1-18. The final layers, where shower fluctuations are strongest, may require some more attention. The studies

performed here thus provide a good starting point to develop a full analytical description of the showers.

### 6.1.4 Longitudinal profile

Two ways of obtaining a mean longitudinal profile have been explained in Sec. 5.5.4. The method of integration of the mean lateral hit densities is better than the standard method. Fig. 6.9 (a) shows the longitudinal profiles at 30 GeV obtained in the two ways. Longitudinal profiles obtained with the standard method show shower-by-shower fluctuations of the total number of hits for all layers. To illustrate the fluctuation of the layer response, the error bar represents the standard deviation of the number of hits distribution of each layer. The normalized longitudinal profiles, i.e. the fraction of the number of hits per layer to the total number of hits as a function of depth in units of radiation length, are shown in Fig. 6.9 (b, c) for the DESY and SPS measurements. All these profiles are obtained using the integration of mean lateral hit densities. For all longitudinal profiles, the shower maximum position moves deeper with beam energy and the longitudinal shower shape becomes wider, which is the qualitatively expected behaviour.

The mean longitudinal profiles of the energy deposition in an electromagnetic cascade are usually reasonably well described by a Gamma distribution (see Eq. 1.10). For our digital calorimeter, simulation studies in Sec. 5.5.5 shows that the Gamma function still works well in a limited range (2-21  $X_0$  for low energy DESY data and 3-21 for high energy data). The position of the shower maximum in radiation length can be calculated from the parameters of the Gamma fit as  $\frac{\alpha-1}{\beta}$ . Its energy dependence is often parameterised as:

$$t_{\max} \approx \ln \frac{E_0}{E_c} + t_0 \quad (6.7)$$

where  $t_0 = -0.5$  and the critical energy of tungsten  $E_c = 8.11$  MeV is calculated using Eq.1.9.

Fig. 6.9 (d) shows the positions of the shower maximum as a function of beam energy compared to Eq. 6.7 shown as the blue dashed curve. Compared to the parameterization,  $t_{\max}$  from our data is shifted by  $\sim 0.8 \pm 0.1 X_0$ . For our prototype, the shower maximum positions could be affected by the following terms:

- Eq. 6.7 is for a homogeneous calorimeter. A sampling calorimeter always has a shifted  $t_{\max}$ .

- Additional material, e.g. the air, scintillators, window of beam pipe and so on.
- A possibly different radiation thickness per layer, which was calculated to be  $0.974 X_0$ . The equivalent radiation thickness of all sensors is listed in Table 8.1.

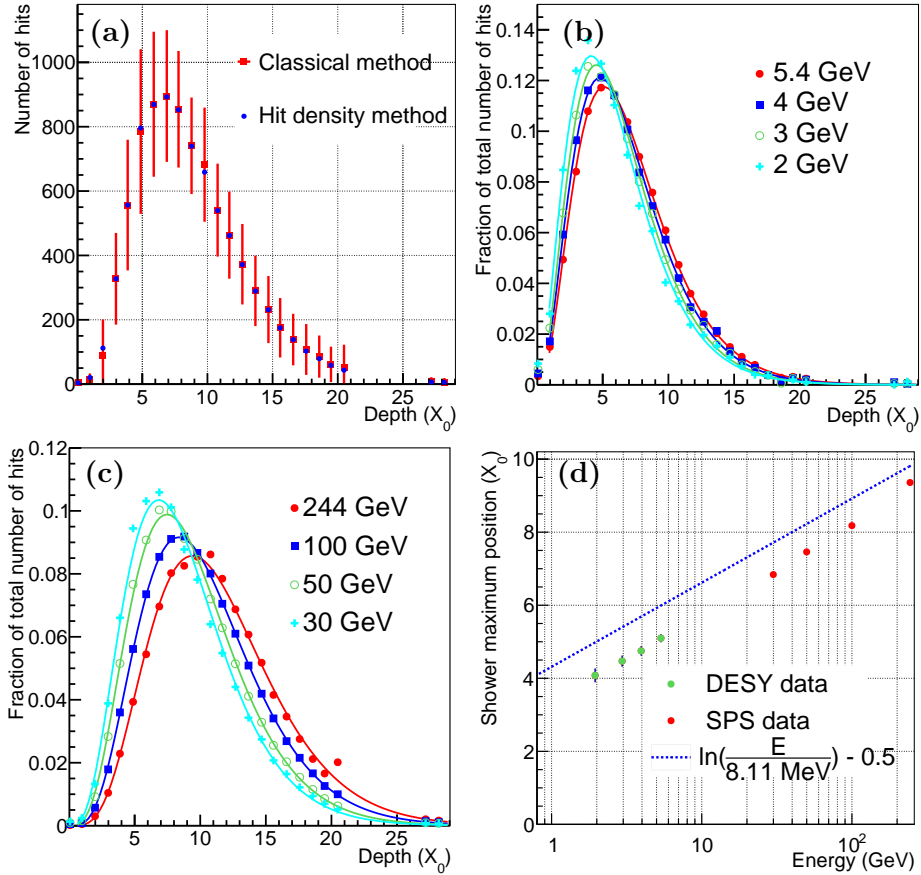


**Figure 6.9:** (a): Longitudinal profiles at 30 GeV, the red squares with red error bar (RMS) represent the profile obtained with the standard method, the blue dots represent the profile obtained by integration of hit densities. Longitudinal profiles obtained by integrating lateral hit densities for various DESY energies (b) and SPS energies (c). The same color lines indicate fits of the Gamma function. (d): Positions of electromagnetic shower maxima as a function of beam energy, the blue dashed line is the parameterization according to Eq. 6.7, red and green markers are for SPS and DESY respectively.



- The fit quality of the Gamma function, which depends on the data and fitting range.

Before reaching the first sensitive layer, beam particles go through a beam exit window, scintillators and air. The equivalent depth of these elements is  $0.12 X_0$  for SPS data, and  $0.15 X_0$  for DESY data according to the specifications. Because of scattering, especially for the low energy DESY beam, the particles go into the detector with an angle, which decreases the average shower maximum depth.

Saturation and charge sharing which mainly occur in the shower core region at early layers for high energy would make the shower maximum position deeper.

Low energy shower particles can be scattered by the spacers which mainly occurs in deep layers, the number hits will increase and shower maximum occurs at a deeper position.

All these can have an effect on the shower maximum position, but none of them is large enough to explain the difference between the measured value and the calculation.

### 6.1.5 Molière radius

The Molière radius is measured by calculating the fraction of hits within a certain distance from the shower axis. The Molière radius is the radius containing 90% of the shower energy

$$\frac{\sum_{l=0}^{23} \int_0^{R_M} 2\pi r \rho_l(r) dr}{\sum_{l=0}^{23} \int_0^{R_{\text{tot}}} 2\pi r \rho_l(r) dr} = 90\% \quad (6.8)$$

where  $\rho_l(r)$  (Eq. 4.16) is the hit density with the noise subtracted. Ideally, this should be normalised to the total amplitude in an infinitely large calorimeter. In our case we use the total number of hits in a cylinder with radius  $R_{\text{tot}}$ , and we choose  $R_{\text{tot}} = 30$  mm. This is significantly larger than twice the theoretical Molière radius. The Molière radius is expected to be energy independent to good approximation according to Eq. 1.13. The estimated Molière radius of the FoCal prototype will be more accurate at low energy than at high energy because less longitudinal leakage and smaller effects from saturation are expected. The left panel in Fig. 6.10 shows the containment for individual layers for 2 GeV positrons. For this energy, a radius of  $R_{\text{tot}} = 25$  mm should be sufficient for full containment. The necessary radius is expected to increase with depth and also with increasing energy. The right panel in Fig. 6.10 shows the measured

cumulative distributions, from which the Molière radius is determined, for 2 GeV and 100 GeV beam energy. For 2 GeV we find  $R_M = 10.5 \pm 0.5$  mm. For the higher energy, the cumulative distribution increases more slowly, indicating that the Molière radius is slightly larger for this case. This apparent energy dependence of the Molière radius may partially be due to saturation of the hit densities, which reduces the hit density at small radii.

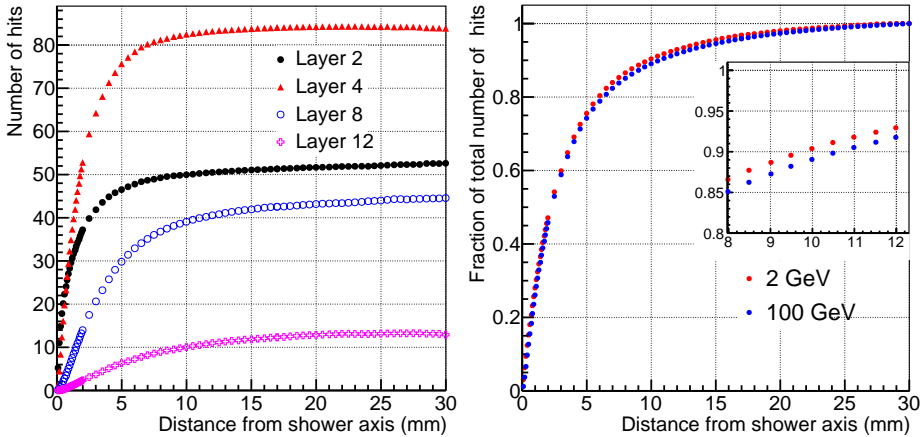


**Figure 6.10:** Cumulative lateral shower profiles for individual layers at 2 GeV (left) and total cumulative shower profiles for 2 GeV and 100 GeV electromagnetic showers (right).

### 6.1.6 Detector response and linearity

In our digital calorimeter, the detector response is given by the total number of hits. Fig. 6.11 shows the distributions of the calibrated total number of hits for electromagnetic showers. Note that the hits in layer 0 have been excluded because of the different settings and absence of absorber in front of it. The distributions are fit with a Gaussian (black curve) to determine the mean and standard deviation. In the upper panel of Fig. 6.12, the average response is plotted as a function of the beam energy. A fit with a linear function is included. Also shown in the figure is the average number of hits determined by integrating lateral hit densities as described in Sec. 5.5.4. All data points are well described by the linear fit. In more detail, this can be seen in the lower panel, which displays the relative deviation of the measured response from the fit. The deviation of the average response is smaller than 4% in a wide range of energies from 2 GeV to 244 GeV, and the average of the deviations is 1.6%, which present a reasonably good linearity.

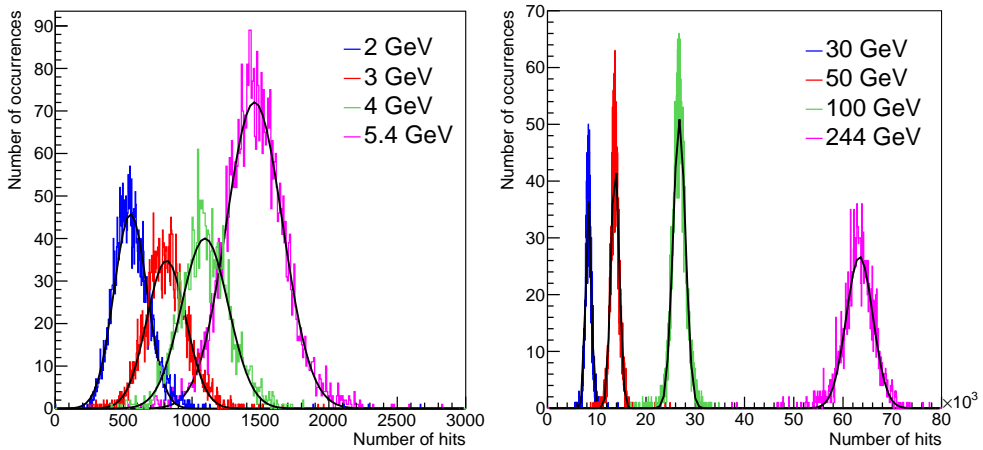


**Figure 6.11:** Distribution of the total number of hits for electromagnetic showers with Gaussian fits in black, for DESY data (left) and SPS data (right).

Some effects specific for our digital calorimeter have been mentioned above. Saturation would lead to a decrease of the number of hits, while cluster tail overlap would lead to an increase. Both effects are expected to be more important at higher energy.

While the effect of lateral leakage on the response is limited by the extrapolation of the hit densities, some residual leakage is still present. We do observe an energy dependence of the Molière radius, but this effect is small. As a consequence, we expect only a very mild effect of non-linearity from lateral leakage. In principle, also the differences in detector settings and measurement conditions between DESY and SPS could introduce a non-linearity appearing in a combined fit.

Apparently, none of the effects discussed above introduces a strong non-linearity in the energy range studied here.

### 6.1.7 Energy resolution

A fundamental goal of FoCal is the energy measurement by counting pixel hits. The energy resolution is calculated using the parameters of the Gaussian fits to the distribution of the total number of hits, as shown in Fig. 6.11.

Figure 6.13 shows the relative energy resolution as a function of beam energy as determined from the Gaussian fits. As discussed in Sec. 1.5, the energy resolution of electromagnetic calorimeters can be decomposed into three terms: ‘stochastic term’, ‘noise term’ and ‘constant term’. The noise term has been obtained from the pedestal measurement which has a very small fluctuation -

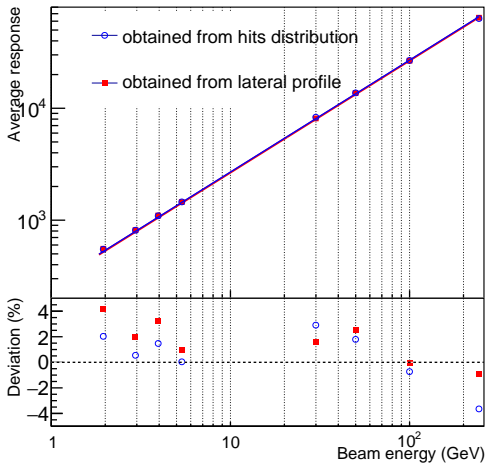


**Figure 6.12:** Average number of corrected hits as a function of beam energy with linear fits (upper panel) and the corresponding deviation (lower panel).

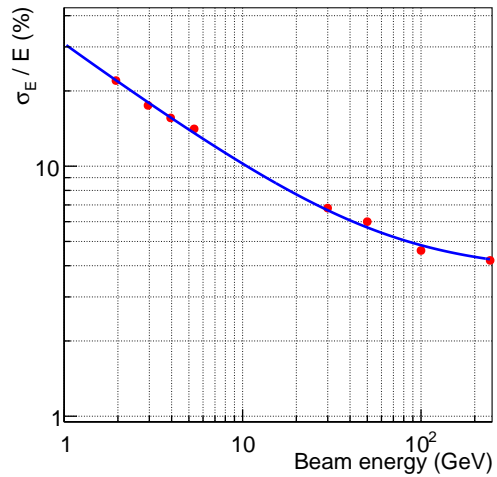


**Figure 6.13:** Energy resolution for electromagnetic showers with fit of Eq. 1.14.

$\sigma_{noise} = 17.1$ , corresponding to a contribution of 6.3% for an energy of 1.06 GeV (see Sec. 5.2). To estimate the contributions from the stochastic term and the constant term, the measured energy dependence of the energy resolution has been fitted with a parametrisation Eq. 1.14. The corresponding parameters are  $a = 30\%$ ,  $b = 6.3\%$  and  $c = 3.7\%$  for the prototype.

### 6.1.8 Two-shower separation

The minimum distance for two-shower separation is determined by the shower width and the granularity of the detector. In our prototype, the small Molière radius reduces the overlap. Overlapping showers can be identified in a shower shape analysis, but the reconstruction of two showers can also be directly achieved by measurements of the shower core only. This is illustrated in Fig. 6.14 which shows an event display of an event that contains two showers. The two showers in this event can be easily separated since most of the hits are located in a small range around the shower cores. For overlapping showers, it may be useful to use the number of hits in a cylinder with a radius  $R$  smaller than the Molière radius to measure the shower energy. To explore the performance of such a method, Fig. 6.15 shows the energy response for a few different cylinder radii. Taking 100 GeV as an example, a series of distributions of the number of hits are plotted

for different cylinder radii in Fig. 6.15 (a). The response as a function of cylinder radius is shown in Fig. 6.15 (c) for three different energies. The response rises strongly for small values of the radius, but levels off quickly beyond the small Molière radius. For  $R = 5$  mm ( $0.5 R_M$ ) already  $\sim 75\%$  of the hits are contained in the cylinder. At the same time, the energy resolution at all three energies is hardly affected for  $R > 3$  mm. The deviations are smaller than 2%. As the fraction of the noise in the total number of hits increases with cylinder radius, which is relevant especially for low energy, 5.4 GeV for example, the energy resolution becomes worse in this case at large  $R$ . In addition, longitudinal profiles using the hits confined in the cylinder are displayed in Fig. 6.15 (b) for 100 GeV positrons using different radii. The shower maximum position moves deeper into the detector with increasing cylinder size.

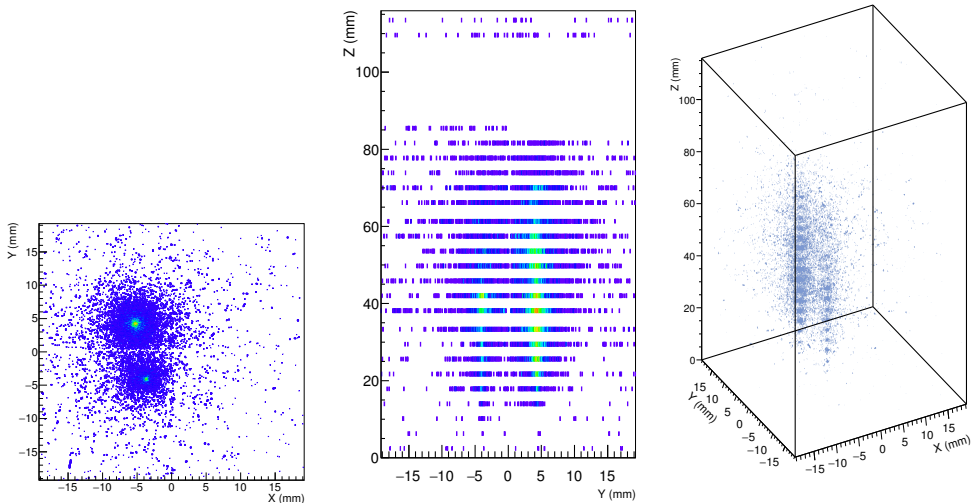


**Figure 6.14:** Event display of a single event containing two electromagnetic showers, projection in  $xy$  (left), projection in  $yz$  (middle), and 3D (right).

## 6.2 Comparison with Simulation

As a next step, we will compare the measurements to GEANT simulations. For this comparison the same analysis methods as in experimental data have been used in simulations, we e.g. use the same hit density analysis method to obtain the energy resolution, Molière radius and longitudinal profile consistently.

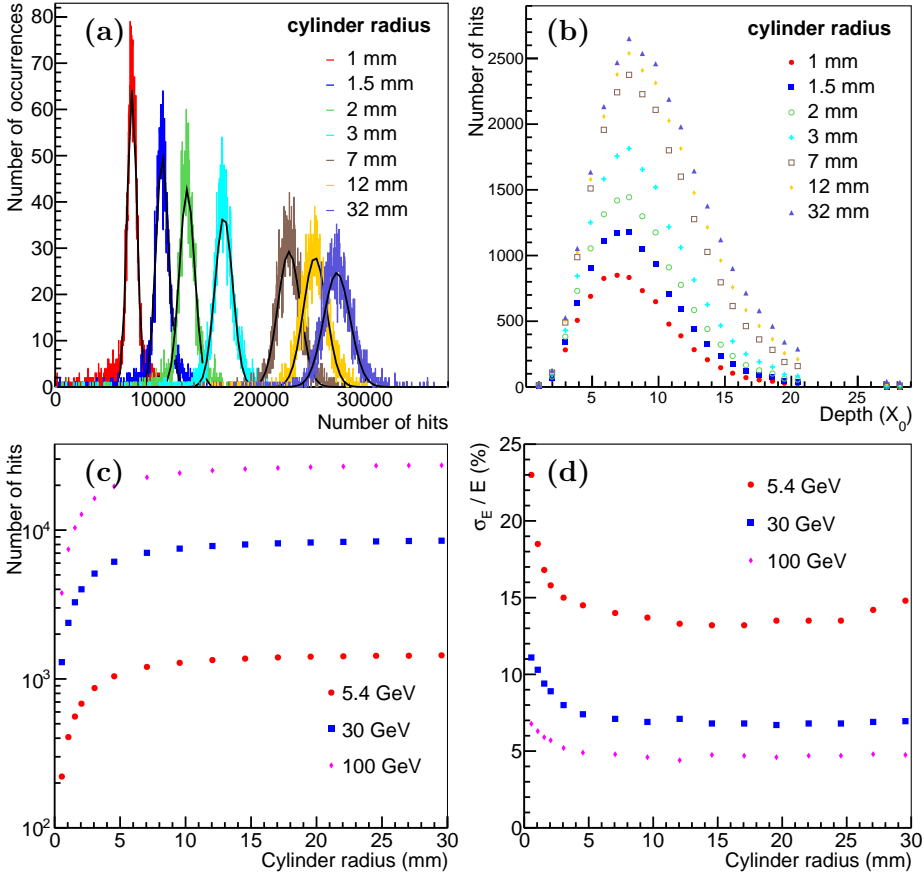
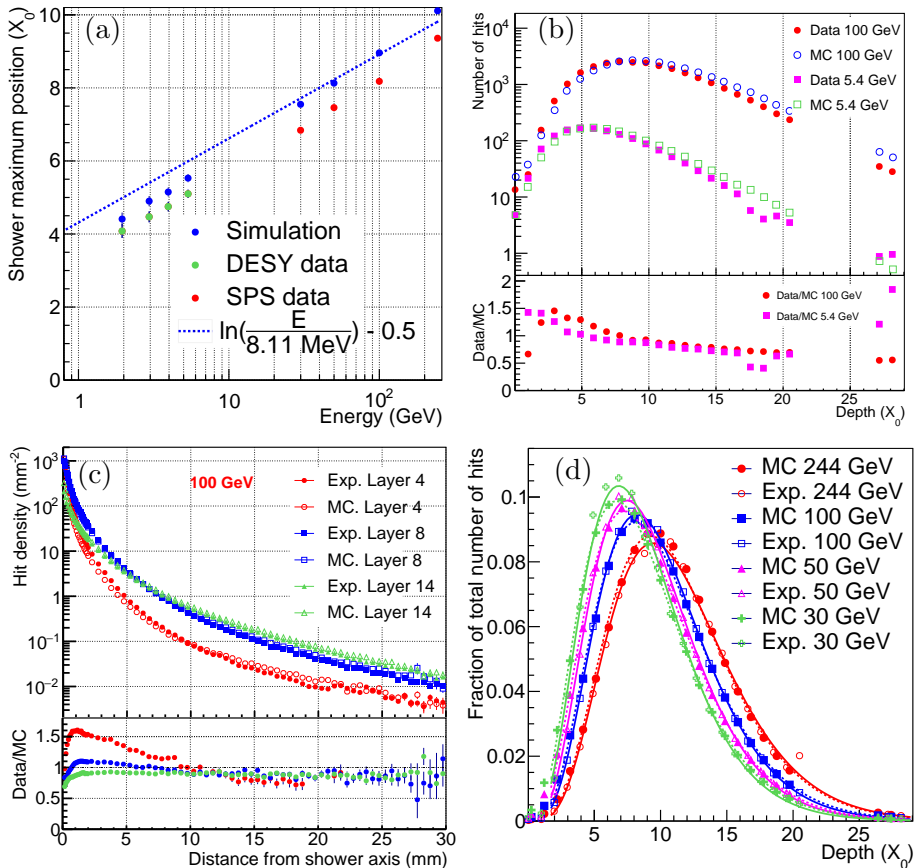


**Figure 6.15:** Detector performance for 100 GeV positrons - distribution of the number of hits with Gaussian fit (a) and longitudinal profiles (b), for a cylinder around the shower axis as a function of cylinder radius. The evolution of the number of hits (c) contained and the energy resolution (d) measured within different cylinder radii.

### 6.2.1 Longitudinal and lateral profile

Fig. 6.16 (a) we show a comparison of the extracted values of  $t_{max}$  as a function of energy for data and simulation. The simulation results are significantly different from the data. The MC is somewhat closer to the empirical function, which is also shown, but also does not fully agree. The difference between simulation and data is relatively small at low energies and increases for high energies. The slope of a linear function fitted independently would be different for simulation and data. These differences relate directly to differences in the longitudinal

profiles as shown in Fig. 6.16 (b). Hit densities in simulation are smaller than data before the shower maximum and high behind it.



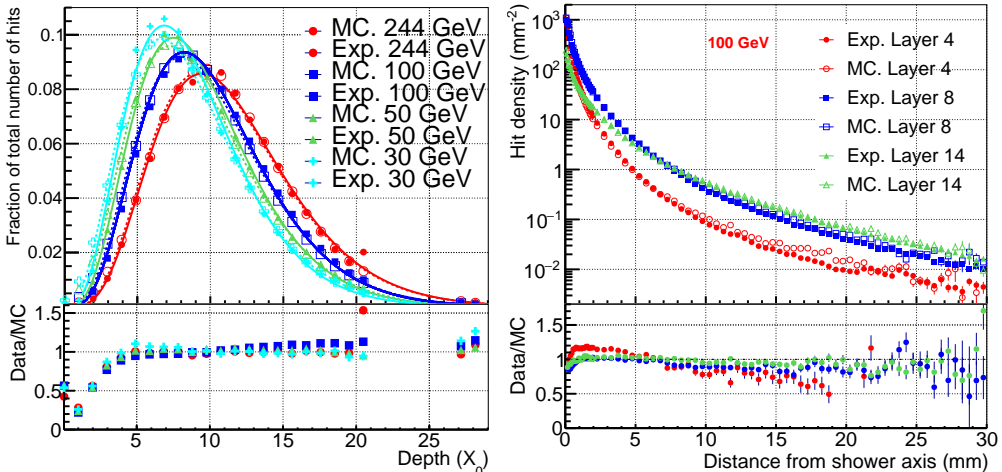
**Figure 6.16:** Comparison between data and GEANT simulation. (a): Shower maximum position as a function of energy. (b): Longitudinal profiles, the lower panel shows the ratio of the number of hits between data and simulation. (c): Lateral profiles for 100 GeV positrons. (d) Measured longitudinal profiles and simulated profiles shifted to lower values by  $0.7 X_0$ .

Fig. 6.16 (c) shows lateral profiles for 100 GeV positrons in data and simulation from three different layers. The gross features of the distributions agree nicely – a more detailed comparison can be done from the ratios of the distributions as shown in the lower panel. For all layers, the ratios ‘Data/MC’ show a small value at  $r = 0$ , which increases for larger  $r$ . While the ratio then levels off for a late layer (number 14), for the early layer (number 4) the ratio increases more strongly to a maximum value larger than 1.5 around  $r = 1$  mm, beyond which it decreases again to reach a similar asymptotic value as the other ratios.

The differences thus occur for small  $r$  values where the pixel occupancy is expected to be high and where the effect of saturation and cluster tail overlap are likely strongest. As these effects depend on details of the charge diffusion process, the discrepancies may point to a not yet fully appropriate implementation of charge diffusion in the simulation.

A shift of the longitudinal distributions from MC to smaller  $t$ -values ( $\Delta t \approx 0.7$ ) leads to a better agreement, which can be seen from Fig. 6.16 (d) where we compare the longitudinal profiles when the simulated longitudinal profile is shifted leftwards by  $0.7 X_0$  improving the agreement. So the discrepancy might be explained by possible additional material in front of the detector.

To test this hypothesis we have performed additional simulations, when a tungsten plate of 2 mm thickness is placed in front of the detector for higher energy (same as SPS). The longitudinal profiles from this simulation are compared to the data in Fig. 6.17. A similar comparison of the lateral profiles is shown in panel (b), where one can see that the agreement between data and MC is much better. The discrepancies between data and simulation are at maximum 20 % in layer 4 in which the lateral hit density profile is very sensitive to exact depth. A good agreement is obtained for a layer at intermediate depth, layer 8 and a later layer 12. The difference in all layers appears in the shower core region - the increasing trend of the ratio at small  $r$  indicates that the shower is broader in data than in simulation.



**Figure 6.17:** Comparison of longitudinal profiles (left) and lateral profiles between data and simulation when a 2.6 mm tungsten is placed in front of the detector. The lower panels show the ratio of data to simulation.



## 6.2.2 Linearity and energy resolution

The distributions of the total number of hits from MC simulation for the ideal detector and for the real detector are shown in Fig. 6.18. The similarity of the distributions for both cases supports the validity of the hit density extrapolation method. The mean and sigma of Gaussian fits to the distributions of the total number of hits in data and simulation for ideal and real detector are extracted, and the energy resolution can be calculated with these numbers. The results are listed in Table 6.3 together with those from the experimental data.

The response as a function of energy for data and MC is shown in Fig. 6.19 together with a linear fit. The lower panel again shows the relative deviation of the response from the fit. The deviation from linearity for data and simulations is smaller than 4% in a wide energy range and the results show qualitatively similar behaviour for 7 out of 8 energies (except 5.4 GeV). The total number of hits in the ideal detector is smaller by 2% compared to the real detector, which means the correction induces  $\sim 2\%$  more hits.

The results for the energy resolution are displayed in Fig. 6.20. Included are fits of Eq. 1.14. The resolution is larger in the real detector compared to the ideal one, and the results from data are still larger than these two. The values of the parameters for the fits of Eq. 1.14 are summarized in Table 6.2.

**Table 6.2:** Three parameters of Eq. 1.14 fits for experimental data and simulation.

	a	b	c
Data	30%	6.3 %	3.7%
Simulated real detector	28%	6.3 %	2.3%
Simulated ideal detector	25%	6.3 %	1.5%

At our lowest energies, the differences between the three curves are dominated by the stochastic term. The larger stochastic term for the real detector compared to the ideal one is likely caused by the smaller effective sampling fraction due to the dead areas. At high energy, the differences are dominated by the constant terms. Also here the main difference between the two simulations is the dead area, which apparently also contributes to the constant term. The most significant discrepancy in the data compared to the real-detector simulation is a larger constant term. Very likely, non-uniformities (like the known different sensitivities of the sensors), which are not implemented in simulation, are responsible for this.

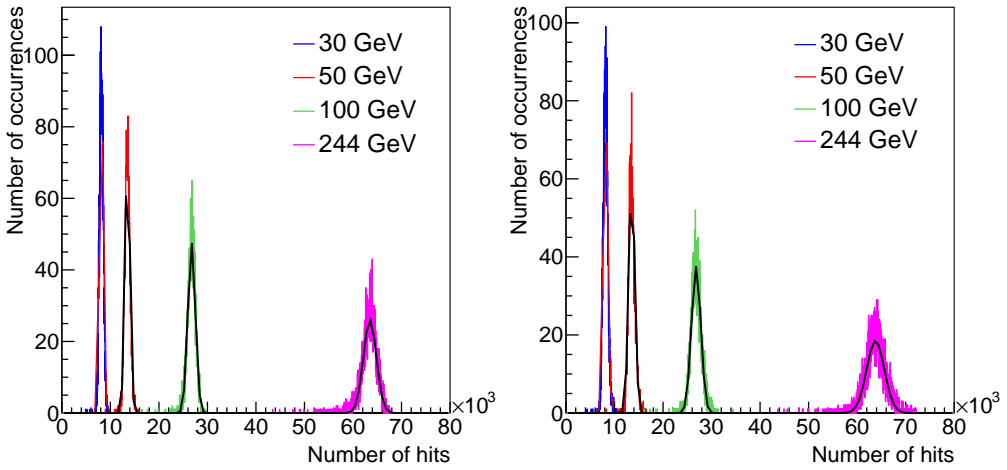


**Figure 6.18:** Distribution of the total number of hits for the ideal detector (left) and the real detector (right) with Gaussian fits in black for the full range.

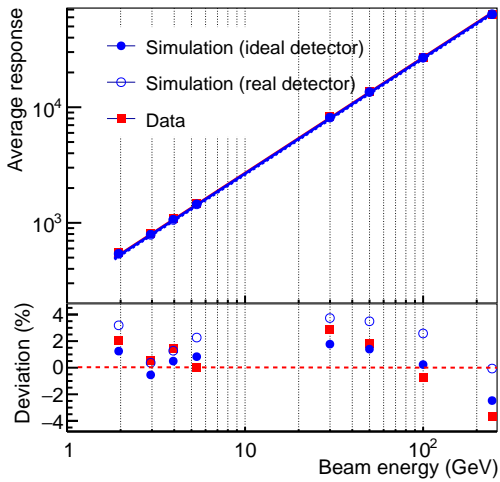


**Figure 6.19:** Comparison of energy response between data and simulation with linear fits (upper panel) and the corresponding relative deviation (lower panel).

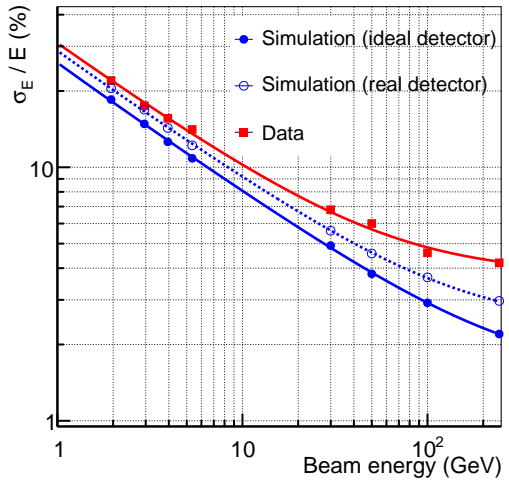


**Figure 6.20:** Comparison of energy resolution between data and simulation with fits of Eq. 1.14.

**Table 6.3:** Parameters of Gaussian fits in full range to the distributions of the total number of hits to all data and simulation.

Beam (GeV)	Data		Ideal detector		Real detector	
	Sigma/Mean	$\sigma_E/E(\%)$	Sigma/Mean	$\sigma_E/E(\%)$	Sigma/Mean	$\sigma_E/E(\%)$
2	121/550	22.0	100/540	18.5	112/542	20.7
3	143/813	17.5	118/796	14.8	133/788	16.9
4	171/1094	15.6	135/1072	12.6	152/1060	14.3
5.4	205/1456	14.1	157/1452	10.8	177/1445	12.2
30	572/8321	6.8	400/8142	4.9	458/8143	5.62
50	827/13718	6.0	513/13520	3.8	619/13540	4.57
100	1250/26756	4.6	782/26730	2.9	990/26840	3.68
244	2700/63366	4.2	1406/63459	2.2	1897/63804	2.97



# Chapter 7

## Conclusions and Outlook

### 7.1 Summary

To study the structure of protons and nuclei, we propose to construct a forward calorimeter (FoCal) to measure forward direct photons as a probe of gluon saturation. The proposed FoCal is a Si-W sampling calorimeter, consisting of high granularity layers (HGL) and low granularity layers (LGL). The HGLs provide a high spatial resolution for two-shower separation and shower shape analysis, and LGLs provide a better energy measurement. To test the feasibility of the FoCal concept, a full high granularity prototype has been built. The prototype uses MIMOSA pixel sensors with a granularity of  $30\ \mu\text{m}$ , and a total of 40 M pixels in a volume of  $4 \times 4 \times 11.6\ \text{cm}^3$ . About 85% of the total volume is W absorber, a small Molière radius of 10.5 mm is expected.

From the raw data, certain properties such as the high positional resolution due to high granularity and the small transverse size of the showers can be seen immediately. The measured patterns in the prototype for electromagnetic showers, hadronic showers and tracks are visibly different. The prototype detector has a number of non-ideal features, some of which were only found during the detector tests. In particular, there are dead areas, unstable channels, and response differences between sensors. We also find that residual pile-up is present in the analysed data, even after the suppression of these events using the triggers scintillators. Several selection procedures are applied to mask bad pixels and remove corrupted data. The presence of non-working sensors and masked channels lead to a wide distribution of the total number of hits and bad longitudinal profiles for raw data. Obviously, additional corrections are necessary to improve the detector performance.

The different hit distributions of electromagnetic showers, hadronic showers, and tracks in the detector allow a discrimination of the different types of events.

The selection criteria are listed in Table 4.1. To obtain the absolute coordinate of each pixel position exactly, all sensors are aligned using cosmic tracks. The relative inclination between detector plane and the beam is determined using pion tracks and is taken into account in the further analysis. The shower position is calculated precisely (with a resolution close to the pixel size) using the position of the shower in the first layer which acts as a tracker. A calibration based on hit density is developed to correct for the sensor sensitivity differences and the dead areas for electromagnetic showers.

In detector simulation, to make a valid comparison, misalignment, noise, and charge diffusion are considered. A realistic detector is simulated, a realistic number of noise pixels has also been added. To study the effects of dead areas, both the ‘ideal detector’ and ‘real detector’ are simulated. By simulations, the reconstruction of the cascade position, the effects of charge diffusion, the calculation of the average response based on hit density, the longitudinal profile fit quality and the effect of calibration, and the associated uncertainties are characterized.

Due to the unique high granularity and small Molière radius, we can measure the lateral profile of showers in unprecedented detail, which is the unique feature of the prototype. To parameterise the shower profiles, we fitted four different functions to the measured lateral profiles. Three of functions have been used for this purpose in the literature before. The most accurate description is provided by a modified power law as given by Eq. 6.5, followed by Eq. 6.3 and Eq. 6.4, the worst description is obtained by the double exponential function. The regular evolution of parameters of Eq. 6.5 with layer number indicates that electromagnetic shower development in the prototype could be parameterised in 3 dimensions. For shower development in the longitudinal direction, a reasonable description is provided by the Gamma function in a wide energy range. However, the shower maximum positions obtained from GEANT simulations are deeper inside the detector than the experiment. The difference could have with possible additional material in the bundle before the detector, but then the agreement in the lateral profiles is not yet perfect. In addition, it is also unclear where this extra unknown material would come from. Another possible interpretation of the results is that current GEANT simulations do not correctly describe the development of electromagnetic cascades.

The Molière radius of this prototype is determined from the lateral profiles, summed over the lateral profiles of all layers. Here 2 GeV and 100 GeV electromagnetic showers were used for a cross check and confirmation. The measured values are very close to the theoretically expected value.

Fig. 6.12 indicates that this prototype has a good linear response – the deviation of the average response is smaller than 4% in a wide range of energy.

The energy dependence of the energy resolution can be parameterised by the well-known function Eq. 1.14. The energy resolution are slightly coarser than expected from MC simulations, but the performance still stays reasonable.

The excellent two-shower separation capabilities of the detector are illustrated with an example in Sec. 6.1.8. For the core part of the shower in the range of  $R < 3$  mm, important characteristics of electromagnetic showers are hardly modified as demonstrated in Fig. 6.15. For the core, the linearity and energy resolution are still good. This is important for the reconstruction of photon pairs from neutral pion decays.

## 7.2 Discussion

There are several differences between data and simulation. Some of these differences may explain the better performance (e.g. energy resolution) in simulation compared to data:

- *Types of sensors.* There are three types of sensors employed in the prototype. However, we could not simulate the resistivity of epi-layer, meanwhile, the thickness of all sensors is set as  $20 \mu\text{m}$  which is not exactly the same as in the real detector. These differences may lead to slightly different clusters sizes in the different sensors, which are not taken into account in the simulation.
- *Beam.* The beam in simulation is uniformly distributed, the beam is pure and without energy spread. There is an energy spread of 1.3% in experiments. The spatial distribution of the beam was changing with time: the distribution was uniform during the 100 GeV beam test, and was focused during the 244 GeV beam test. The purity of selected interesting events can not reach the value of 100% as in the simulation.
- *Positions of components.* In the simulation, all components are placed according to the design, and then the modules are displaced from their nominal position based on the track alignment. Misalignment can be caused by the movement of the sensors, PCBs or modules, but we really do not know which part causes the misalignment. Besides, due to the fact that overlap is not allowed in simulation, the misalignment is generated by moving modules but not moving sensors.
- *Limits of the calibration.*

(i) The possible non-uniformity of the response within each sensor is not taken into account. Because of the uniform sensor, the simulated

sensors will present a better performance than the real sensors, especially for the energy resolution.

(ii) The correction for dead areas has a limited precision. In particular for the case where dead sensors are present in the same quadrant in subsequent layers, the interpolation procedure has been shown to introduce biases (for example Fig. 5.10), from the response as a function of position, we know that for ‘case2’ the correction is not as good as for ‘case1’.

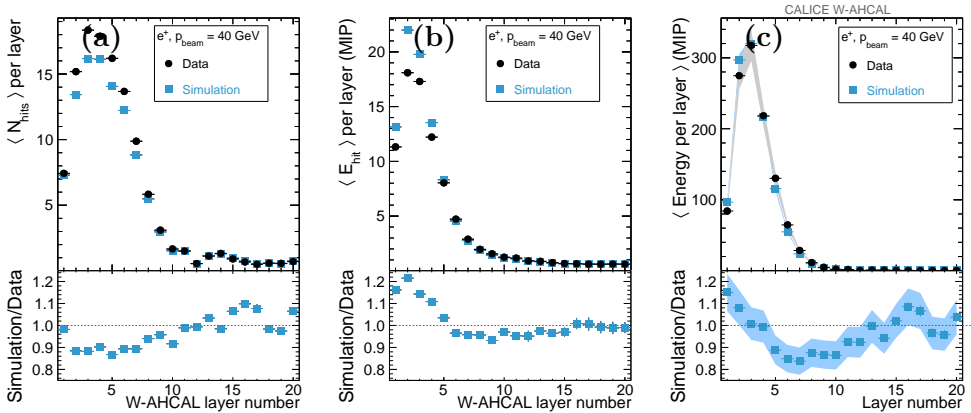


**Figure 7.1:** Longitudinal distributions in the CALICE W-AHCAL as measured with 40 GeV positrons. The black filled circles show the experimental data, the blue filled squares the results from MC simulations. Each layer in the W-AHCAL has a thickness of  $2.8 X_0$ . (a): Number of hits as a function of the layer number, (b): energy per hit as a function of layer number, (c): total energy deposition per layer as a function of layer number. These three figures have been provided by [39].

- *Digitisation.* The prototype we built is a digital calorimeter, the available literature on such calorimeters is based on the homogeneous analog calorimeters. In the case of a digital calorimeter, the number of hits is not exactly proportional to the energy deposition. This effect is included in the simulation, so differences between the measured response and the simulation would originate from an incomplete understanding of for example the charge diffusion.

Finally, the observed differences between measurements and simulation may also point to a not completely adequate description of the shower development in GEANT. Unfortunately, there exist only very few studies of the shower development with comparable detail to our measurement. But there are unpublished results from the CALICE collaboration using their W-AHCAL [40], which show



qualitatively similar effects, as can be seen from Fig. 7.1. The left panel shows the number of hits per layer as a function of layer number for 40 GeV positrons from test beam measurements (black circles) and from GEANT simulations (blue squares). Clearly, the data shows a larger number of hits compared to simulation in the first 10 layers, qualitatively very similar to our results shown e.g. in Fig. 6.16 (b). Note that the absolute normalisation in our analysis has been adjusted in the calibration procedure, such that the significant observation is the different shape of the longitudinal profile. In both measurements, the shower maximum is reached earlier in data compared to simulations. As the CALICE W-AHCAL has analog readout, one can also study the deposited energy. Fig. 7.1 (b) shows the average energy per hit in the silicon layers again as a function of depth, here a qualitatively different trend is observed – the energy per hit is rather lower in data compared to simulation for the early layers. For the total energy per layer (Fig. 7.1 (c)) the two effects seem to partially compensate, however, there is still a significant discrepancy between data and simulation for intermediate layers.

These results from CALICE emphasise the significance of the deviations of the longitudinal profile in data from GEANT calculations. It is thus likely that also other deviations, as seen in the lateral profiles point to significant shortcomings of the GEANT description. A full interpretation of these phenomena will however require further, more detailed studies.

### 7.3 Outlook

The current calibration procedure uses a single calibration factor for a single sensor. This way, it can not account for non-uniform sensitivity within the sensors. The simplest method to overcome this limitation is to use several calibration factors per sensor. One can do this by

- (i) Dividing the sensor into regions, for example  $3 \times 3$ .
- (ii) Applying the same calibration procedure which has been used for the full sensor as described in Sec. 4.6.1.

For high energy and early layers, saturation is observed as illustrated in Fig. 6.5. Thus one expects a slightly lower response for high energy, which is seen as a deviation from linearity (Fig. 6.12), but the effects of saturation are not strong in the prototype. To obtain a better performance, one could attempt to correct for the saturation using the knowledge of the shower distribution.

In addition, a number of further studies can be performed with the prototype, but are beyond the scope of this thesis. A few examples are:

- We have found parameterizations for individual lateral profiles. It would be very useful to combine the knowledge of the shapes in a full three-dimensional parameterised shower model.
- One can further study the event-by-event fluctuations of the shower distributions.
- Data on hadron beams, including hadronic showers, have been collected, so also detailed analyses of hadronic showers in the prototype can be performed in the future.

# Chapter 8

## Appendix

*Table 8.1: Sensors in the prototype*

Layer	Quadrant	Sensor	PCB	Z (mm)	Depth ( $X_0$ )
0	0	0	R81	2.05	0.03
	1	1	L16	2.05	
	2	2	L6	1.90	
	3	3	R14	1.90	
1	0	44	R33	5.98	1.00
	1	45	L50	5.98	
	2	46	R67	5.86	
	3	47	R32	5.86	
2	0	48	R8	9.96	1.98
	1	49	L27	9.96	
	2	50	L41	9.79	
	3	51	R35	9.79	
3	0	92	R53	13.90	2.95
	1	93	L49	13.90	
	2	94	L38	13.77	
	3	95	R58	13.77	
4	0	4	R45	17.94	3.92
	1	5	L25	17.94	
	2	6	L44	17.70	
	3	7	R57	17.70	
5	0	40	R20	21.93	4.90
	1	41	L14	21.93	
	2	42	L71	21.75	

	3	43	R60	21.75	
6	0	52	R50	25.92	5.87
	1	53	L3	25.92	
	2	54	L68	25.74	
	3	55	R75	25.74	
7	0	88	R17	29.92	6.85
	1	89	L9	29.92	
	2	90	L47	29.73	
	3	91	R40	29.73	
8	0	8	R54	33.87	7.82
	1	9	L66	33.87	
	2	10	L31	33.73	
	3	11	R49	33.73	
9	0	36	R13	37.85	8.80
	1	37	L1	37.85	
	2	38	L7	37.68	
	3	39	R3	37.68	
10	0	56	R48	41.86	9.77
	1	57	L34	41.86	
	2	58	L11	41.72	
	3	59	R15	41.66	
11	0	84	R65	45.82	10.74
	1	85	L57	45.82	
	2	86	L63	45.73	
	3	87	R61	45.73	
12	0	12	R59	49.85	11.72
	1	13	L37	49.85	
	2	14	L48	49.69	
	3	15	R56	49.69	
13	0	32	R18	53.88	12.69
	1	33	L13	53.88	
	2	34	L26	53.65	
	3	35	R38	53.65	
14	0	60	R55	57.83	13.67
	1	61	L43	57.83	
15	2	62	L35	57.69	14.64
	3	63	R34	57.69	
14	0	80	R21	61.81	13.67
	1	81	L18	61.81	
	2	82	L42	61.64	

	3	83	R52	61.64	
16	0	16	R36	65.81	15.62
	1	17	L45	65.81	
	2	18	L30	65.62	
	3	19	R51	65.62	
17	0	28	R12	69.78	16.59
	1	29	L2	69.78	
	2	30	L23	69.61	
	3	31	R44	69.61	
18	0	64	R72	73.73	17.56
	1	65	L58	73.73	
	2	66	L40	73.65	
	3	67	R62	73.65	
19	0	76	R1	77.79	18.54
	1	77	L5	77.79	
	2	78	L32	77.60	
	3	79	R47	77.60	
20	0	20	R63	81.79	19.51
	1	21	L60	81.79	
	2	22	L64	81.66	
	3	23	R79	81.66	
21	0	24	R69	85.86	20.49
	1	25	L53	85.86	
	2	26	L54	85.71	
	3	27	R70	85.71	
22	0	68	R66	109.98	27.17
	1	69	L59	109.98	
	2	70	L62	109.86	
	3	71	R78	109.86	
23	0	72	R39	113.94	28.14
	1	73	L46	113.94	
	2	74	L12	113.91	
	3	75	R19	113.91	

Orange : 14  $\mu\text{m}$  10  $\Omega \cdot \text{cm}$  (type I)

Green : 15  $\mu\text{m}$  400  $\Omega \cdot \text{cm}$  (type II)

Red : 20  $\mu\text{m}$  400  $\Omega \cdot \text{cm}$  (type III)

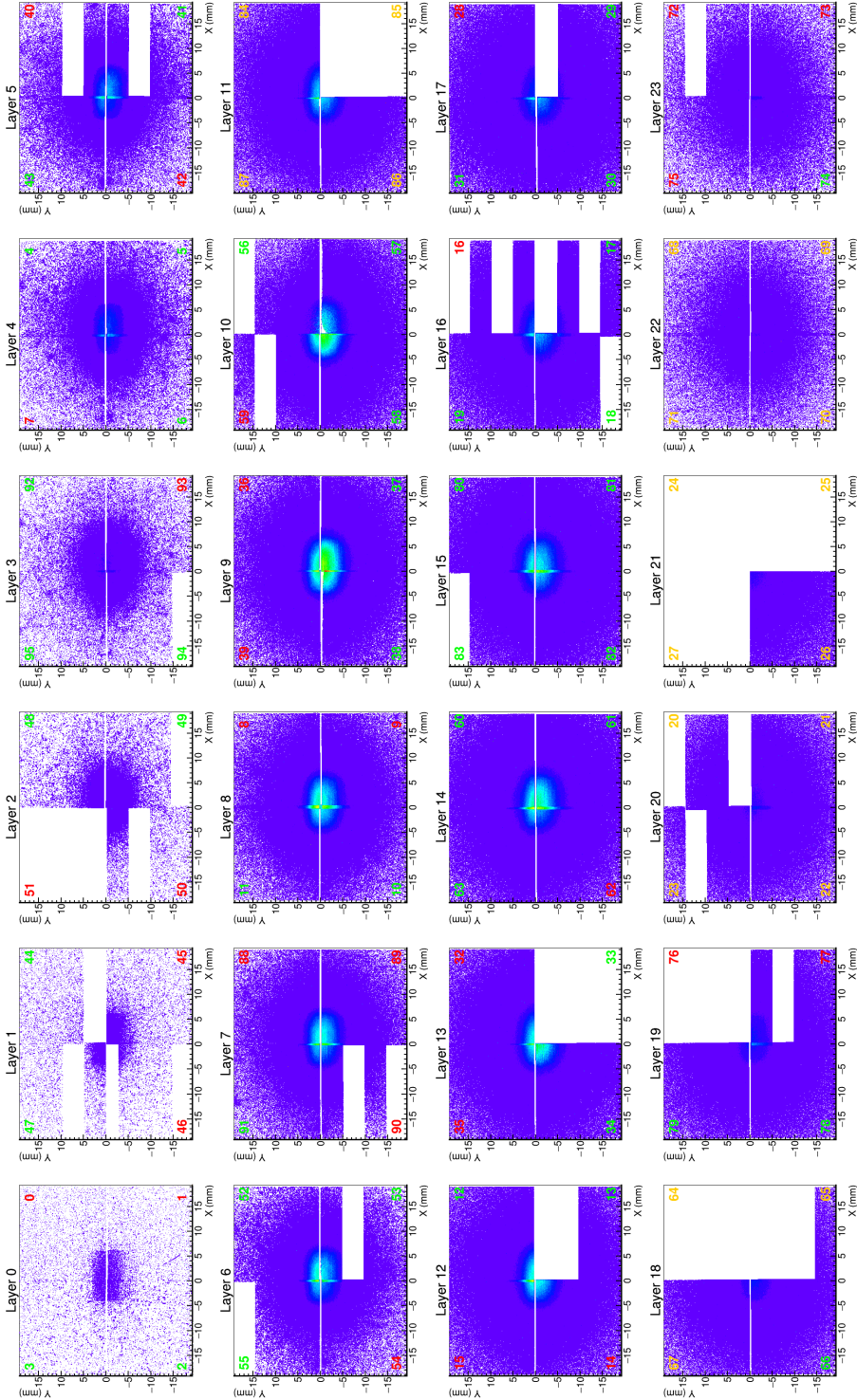


**Figure 8.1:** Uncalibrated distribution of hits in 2D at all 24 layers for cleaned-up data of 244 GeV when the central (H&V) trigger is selected with same z-scale, bin size = 30  $\mu\text{m}$ , sensor number is marked at corner, sensor type in color, orange = 14  $\mu\text{m}$  10  $\Omega/\text{cm}$ , green = 15  $\mu\text{m}$  400  $\Omega/\text{cm}$ , red = 20  $\mu\text{m}$  400  $\Omega/\text{cm}$ .

**Table 8.2:** Parameters of fitting function  $g(r)$ ,  $f_2(r)$  and  $f_3(r)$  for 50 GeV positrons.

Layer	$g(r)$			$f_2(r)$				$f_3(r)$						
	$p_0$	$p_1$	$p_2$	$A_1$	$p$	$\lambda_1$	$\lambda_2$	$A_1$	$p$	$\lambda_1$	$\lambda_2$			
0	1.70	4.58	3.45	68.4	0.03	0.74	0.003	6.99	0.88	-0.01	1.11			
1	48.8	2.71	0.095	195	0.07	0.82	0.06	4.59	0.33	-0.18	1.18			
2	269	2.92	0.121	1.21	0.08	0.85	0.07	37.0	0.36	0.20	1.42			
3	517	3.26	0.179	112	0.10	0.60	0.13	121	0.37	0.33	1.72			
4	675	3.48	0.226	156	0.10	0.52	0.15	228	0.35	0.38	1.87			
5	744	3.49	0.265	146	0.12	0.40	0.20	342	0.34	0.46	2.12			
6	685	3.52	0.304	133	0.13	0.35	0.23	407	0.33	-0.52	2.32			
7	515	3.70	0.431	629	0.18	0.25	0.51	443	0.32	-0.73	2.85			
9	300	3.70	0.480	629	0.18	0.25	0.51	405	0.31	0.80	3.12			
10	205	3.72	0.562	341	0.22	0.20	0.67	375	0.31	0.95	3.58			
11	133	3.56	0.634	213	0.26	0.21	0.76	325	0.66	4.43	1.18			
12	102	3.65	0.683	156	0.28	0.24	0.86	281	0.37	1.32	4.83			
13	68.1	3.61	0.758	109	0.30	0.21	0.95	231	0.36	1.44	5.24			
14	43.1	3.58	0.852	70.4	0.34	0.19	1.05	187	0.36	1.63	6.00			
15	28.4	3.49	0.928	46.2	0.38	0.19	1.15	150	0.35	1.78	6.61			
16	19.6	3.28	0.949	29.3	0.43	0.23	1.18	117	0.35	1.90	7.32			
17	12.1	3.37	1.10	19.8	0.46	0.18	1.36	93.9	0.34	2.13	7.96			
18	7.43	3.18	1.21	11.1	0.56	0.22	1.51	75.4	0.67	9.37	2.39			
19	5.04	3.17	1.27	8.32	0.55	0.16	1.49	55.5	0.69	9.36	2.40			
20	3.10	2.70	1.30	3.93	0.80	0.31	1.67	46.3	0.68	12.5	2.99			
21	1.65	2.84	1.61	2.14	0.93	0.31	2.04	33.0	0.28	3.04	12.3			
22	1.03	2.09	2.66		Failed					Failed				
23		Failed				Failed					Failed			





# Bibliography

- [1] V. N. Gribov and L.N. Lipatov, *Sov. J. Nucl. Phys.* **15** (1972) 438.
- [2] The parton model, P. Hansson, KTH, November 18, 2004.
- [3] L. McLerran and R. Venugopalan, *Phys. Rev. D* **49** (1994) 2233–2241.
- [4] L. McLerran and R. Venugopalan, *Phys. Rev. D* **49** (1994) 3352–3355.
- [5] L. McLerran and R. Venugopalan, *Phys. Rev. D* **50** (1994) 2225–2233.
- [6] T. Peitzmann, Proceedings of CHEF 2013 - Calorimetry for the High Energy Frontier, arXiv:1308.2585v1
- [7] <http://aliceinfo.cern.ch/Public/en/Chapter2/Page3-subdetectors-en.html>
- [8] <http://aliceinfo.cern.ch/secure/Documents/TDR/index.html>
- [9] R. Wigmans, *Calorimetry - Energy Measurement in Particle Physics*, Oxford Science Publications, (2000).
- [10] Y.S. Tsai, *Rev. Mod. Phys.* **46**, 815 (1974).
- [11] B. Rossi, *High Energy Particles*, Prentice-Hall, Inc., Englewood Cliffs, NJ, 1952.
- [12] E. Longo and I. Sestili, *Nucl. Inst. Meth.* **128** (1975) 283.
- [13] W.R. Nelson et al., *Phys. Rev.* **149**, 201 (1966)
- [14] G. Bathow et al., *Nucl. Phys.* **B20**, 592 (1970).
- [15] CERN-LHCC-99-4 ; ALICE-TDR-2.
- [16] CERN-LHCC-2008-014 ALICE-TDR-014
- [17] CERN-LHCC-96-041 ATLAS-TDR-2.

- [18] CERN-LHCC-97-033; CMS-TDR-4.
- [19] CERN-LHCC-2000-036 LHCb-TDR-2.
- [20] B. Bilki et al., Nucl. Inst. Meth **A794**, (2015) 240–254.
- [21] D. Fehlker, *et al.*, *Electronics for a highly segmented electromagnetic calorimeter prototype*, 2013 JINST 8 P03015.
- [22] M.Reicher, *Digital calorimetry using pixel sensors*, PhD thesis Utrecht University (2016).  
[https://www.nikhef.nl/pub/services/biblio/theses\\_pdf/thesis\\_M\\_Reicher.pdf](https://www.nikhef.nl/pub/services/biblio/theses_pdf/thesis_M_Reicher.pdf)
- [23] A. Himmi, A. Brogna, *et al.*, *PHASE-1 User Manual*, Institut de Recherches Subatomiques IN2P3-CNRS / ULP Strasbourg, France.
- [24] P.F. Dauncey, *Performance of CMOS sensors for a digital electromagnetic calorimeter*, PoS (ICHEP 2010) 502.
- [25] R.Nusselder, *Focal chip calibration with cosmic*, Bachelor thesis Utrecht University (2014).
- [26] P.J. Blenkers, *The development of a GEANT based Monte Carlo simulation framework for the R&D process of the FoCal calorimete*, Master thesis Utrecht University (2012).
- [27] G. Nooren, *Extremely fine grained electro-magnetic calorimeter*, PoS (RD11) 026.
- [28] E. Rocco, *Highly granular digital electromagnetic Calorimeter with MAPS*, in Proceedings of the 37 International Conference on High Energy Physics (ICHEP 2014).
- [29] G. Nooren and E. Rocco, *A particle counting EM calorimeter using MAPS*, J.Phys: Conference Series **587** 012061.
- [30] H. Wang, *private communication*. Utrecht university
- [31] A. Brogna *et al.*, *Manual PHASE1*, IPHC Strasbourg.
- [32] K.A.Olive *et al.*, *Particle Physics booklet*, 2014.  
<http://pdg.lbl.gov/>.
- [33] Application Software Group, *Geant Detector Description and Simulation Tool*, CERN, Geneva (1993).

- 
- [34] Geant4 Collaboration, *Geant4 User's Guide for Application Developers* Published 14 December, 2007.
- [35] L. Maczewski *et al.*, Nucl. Inst. Meth. **A610** (2009) 640.
- [36] G. Ferri *et al.*, Nucl. Inst. Meth. **A273** (1988) 123.
- [37] G. Grindhammer *et al.*, in *Proceedings of the Workshop on Calorimetry for the Supercollider*, Tuscaloosa, AL, March 13-17, 1989, p. 151.  
<https://arxiv.org/abs/hep-ex/0001020>.
- [38] R. Hagedorn, Riv. Nuovo Cim. 6 (1983) 1.
- [39] E. Sicking, *CALICE*, *private communication*, 2017.
- [40] M. Chefdeville, JINST 10 (2015) P12006.



# Nederlandse Samenvatting

Om de structuur van protonen en kernen te bestuderen, stellen wij voor om een voorwaartse calorimeter te construeren, ten einde voorwaartse directe fotonen te meten als sonde van gluonverzadiging. De voorgestelde FoCal is een Si-W sampling calorimeter, die bestaat uit lagen wolfram die dienen voor foton-conversie, met detectielagen met hoge granulariteit (HGL) en lage granulariteit (LGL). De HGLs zorgen voor een hoge positieresolutie ten behoeve van de analyse van de vorm van cascades en de scheiding van naburige cascades en de LGLs zorgen voor een betere energiemeting. Om de haalbaarheid van het FoCal-concept te testen, is een prototype gebouwd dat volledig is uitgerust met detectielagen met een hoge granulariteit. Dit prototype gebruikt sensoren van het MIMOSA type, met pixels met een granulariteit van  $30\ \mu\text{m}$ , en in totaal 40 miljoen pixels. Ongeveer 85% van het totale volume bestaat uit absorptielagen van wolfram (W), en de verwachte Molièrestraal is 10.5 mm.

Uit de ruwe gegevens zijn bepaalde eigenschappen, zoals de hoge positieresolutie door hoge granulariteit en de kleine transversale grootte van de cascades, direct te zien. De met het prototype gemeten patronen zijn zichtbaar verschillend voor elektromagnetische cascades, hadronische cascades en sporen. De prototypedetector heeft ook een aantal niet-ideale eigenschappen, waarvan sommigen slechts tijdens de detectortests werden gevonden. In het bijzonder zijn er dode gebieden, onstabiele kanalen, en responsverschillen tussen sensoren. Wij vinden ook dat er pile-up aanwezig is in de geanalyseerde gebeurtenissen, ook na de onderdrukking van deze gebeurtenissen met behulp van de trigger-scintillatoren. Verscheidene selectieprocedures worden toegepast om slechte pixels te maskeren en corrupte gegevens te verwijderen. De aanwezigheid van niet-werkende sensoren en gemaskeerde kanalen leidt tot een brede verdeling van het totale aantal hits en slechte longitudinale profielen in de ruwe gegevens. Extra correcties zijn noodzakelijk om de detectorprestaties te verbeteren.

Om de precieze absolute coördinaten van elke pixelpositie te verkrijgen, worden alle sensoren uitgelijnd met hulp van sporen van kosmische muonen. De relatieve hoek tussen detectorplaten en de bundel wordt bepaald door middel van pionsporen en wordt in acht genomen in de verdere analyse. De cascadepositie wordt berekend in de eerste laag, die hiermee als tracker dienst doet,

---

waarbij gebruik wordt gemaakt van andere lagen om de invloed van ruis te onderdrukken. De resolutie van deze positiebepaling is vergelijkbaar met de pixelpositie. Een calibratie gebaseerd op hitdichtheid is ontwikkeld om de verschillen in de sensorgevoeligheid en de dode gebieden voor elektromagnetische cascades te corrigeren.

In de detectorsimulaties zijn de misuitlijning, de ruis en de ladingsdiffusie geïmplementeerd. Om een realistische detector te simuleren, is ook een realistisch aantal ruispixels toegevoegd. Om de gevolgen van dode gebieden te bestuderen, worden zowel de ‘ideale detector’ als de ‘echte detector’ gesimuleerd. Door middel van simulaties zijn de reconstructie van de cascadepositie, de effecten van ladingsdiffusie, de berekening van de gemiddelde respons gebaseerd op hitdichtheid, de fitkwaliteit van de longitudinale profielen en het effect van calibratie bestudeerd en de bijbehorende onzekerheden gekarakteriseerd.

Door de unieke hoge granulariteit en de kleine Molièrestraal van het prototype, kunnen wij het transversale profiel van cascades in ongekend detail meten. Om de parameters van de cascade te bepalen zijn vier verschillende functies aan de gemeten transversale profielen gefit. Drie van deze functies zijn eerder hiervoor gebruikt. Het regelmatige verloop met laagnummer van parameters van de beste functie wijst erop dat wij de elektromagnetische cascadeontwikkeling in het prototype ook door een parameterisering in drie dimensies kunnen beschrijven. Voor de cascadeontwikkeling in de longitudinale richting geeft de Gamma-verdeling in een breed energiegebied een redelijke beschrijving. Nochtans liggen de posities van het maximum van de cascade, berekend uit GEANT-simulaties, dieper in de detector dan de posities uit de experimentele gegevens. Het verschil zou met mogelijk extra materiaal in de bundel vóór de detector te maken kunnen hebben, maar dan is de overeenkomst in de laterale profielen nog niet perfect. Daarnaast is het ook onduidelijk waar dit extra onbekende materiaal vandaan zou komen. Een andere mogelijke interpretatie van de resultaten is dat de huidige GEANT-simulaties de ontwikkeling van elektromagnetische cascades niet correct beschrijven.

De Molièrestraal van ons prototype is bepaald uit de transversale profielen, gesommeerd over alle lagen, voor cascades van 2 GeV en 100 GeV. De gemeten waarden liggen zeer dicht bij de theoretisch verwachte waarde.

Dit prototype heeft een goede lineaire respons – de afwijking van de gemiddelde respons is kleiner dan 4% in een breed energie-interval. De energieafhankelijkheid van de energieresolutie kan door de gebruikelijke functie worden beschreven waarvan de parameters zijn bepaald. De waarden van energieresolutie zijn iets groter dan verwacht op basis van de MC simulaties, maar laten nog redelijke prestatie zien.

---

Het uitstekende vermogen van detector om naburige cascades te scheiden wordt geïllustreerd met een voorbeeld. Voor het kerndeel van de shower in een cilinder van  $R < 3$  mm zijn belangrijke kenmerken van elektromagnetische cascades nauwelijks anders dan voor de volledige cascade. Ook voor de kern zijn de lineariteit en de energieresolutie nog goed. Dit is belangrijk voor de reconstructie van fotonparen van het verval van neutrale pionen.

---



# Acknowledgments

My deepest gratitude goes first and foremost to my supervisor, Prof. Thomas Peitzmann, for your constant encouragement and guidance. It is you that I had the opportunities of joining the FoCal group, attending meetings and so on. You have walked me through all the stages of this thesis. Without your consistent and illuminating instruction, this thesis would not have reached its present form.

I would like to express my sincere gratitude to my copromotor Dr. Ger-Jan Nooren, you always answer my questions with patient and points out the possible solutions.

Dr. Marco van Leeuwen, my another copromotor, so smart and diligent that I admire you so much. You can help me solve issues from programming, analysis to performing beam test quickly.

My thesis was modified after receiving the comments and suggestions from my promoter, copromotoren and the reading committee. I can hardly express my appreciation to you with words.

The prototype had been built when I came to the FoCal group, I have to thank these people – Ton, Marcel, Arie, keen and the people from Bergen University, who design and assemble the prototype. Our mechanic engineer Ton, you not only built the prototype but also have been assisting in performing all the beam tests.

At the beginning of entering the FoCal group, Martijn and Elena helped me familiar with the FoCal project and prototype. Although you left the FoCal group, but you still gave help when we need you. Martijn, the developer of the software of the prototype, who developed and modified 5 times to reach the final version. I learned so much from your beautiful and logical code.

Hongkai, your coming makes the project goes forward fast and continue. Discussing with you help me shorten crooked road on research. Some of your results I take them directly, like the alignment.

The FoCal team also includes the Japanese group, Indian group and Norway group. We are responsible for different parts of the FoCal detector and perform the beam tests together happily.

In the past 4 years, I received lots of help for my work and life from the people in subatomic physics group. I would like also to thank you: Allesandro, Alberto, Andre, Andrea, Astrid, Davide, Haque, Hongyan, Jaccopo, Naghmeh,

---

Kees, Martijn, Merijn, Mike, Misha, Paul, Redmer, Raimond, Sandro, You.  
Special thanks to our football team for the happiness we share. At the end,  
most importantly, thanks to my family for their everlasting support.

# Curriculum

I was born in June 12th, 1984 Shaanxi, China. From 2004, I studied applied physics in the Zhengzhou University, and received my bachelor degree in 2008. After that I started Master-Doctor combined program, and enrolled as PhD in 2010 at the Lanzhou University, and focused on study of Micromegas detector for fast neutron imaging.

During November 2012 to December 2016, I worked in the FoCal group as a PhD in the Utrecht University and Nikhef in the Netherlands. This thesis presents the results of my research work.